

May 2023

On Outflows Due to Radiation

Randall Cody Dannen

Follow this and additional works at: <https://digitalscholarship.unlv.edu/thesesdissertations>



Part of the [Astrophysics and Astronomy Commons](#)

Repository Citation

Dannen, Randall Cody, "On Outflows Due to Radiation" (2023). *UNLV Theses, Dissertations, Professional Papers, and Capstones*. 4668.

<http://dx.doi.org/10.34917/36114693>

This Dissertation is protected by copyright and/or related rights. It has been brought to you by Digital Scholarship@UNLV with permission from the rights-holder(s). You are free to use this Dissertation in any way that is permitted by the copyright and related rights legislation that applies to your use. For other uses you need to obtain permission from the rights-holder(s) directly, unless additional rights are indicated by a Creative Commons license in the record and/or on the work itself.

This Dissertation has been accepted for inclusion in UNLV Theses, Dissertations, Professional Papers, and Capstones by an authorized administrator of Digital Scholarship@UNLV. For more information, please contact digitalscholarship@unlv.edu.

ON OUTFLOWS DUE TO RADIATION

By

Randall Cody Dannen

Bachelor of Science - Physics
Bachelor of Science - Mathematics
University of Nevada, Las Vegas
2016

Master of Science - Astronomy
University of Nevada, Las Vegas
2018

A dissertation submitted in partial fulfillment
of the requirements for the

Doctor of Philosophy – Astronomy

Department of Physics & Astronomy
College of Sciences
The Graduate College

University of Nevada, Las Vegas
May 2023

Copyright By Randall Cody Damm 2023
All Rights Reserved



Dissertation Approval

The Graduate College
The University of Nevada, Las Vegas

April 6, 2023

This dissertation prepared by

Randall Cody Dannen

entitled

On Outflows Due to Radiation

is approved in partial fulfillment of the requirements for the degree of

Doctor of Philosophy – Astronomy
Department of Physics & Astronomy

Daniel Proga, Ph.D.
Examination Committee Chair

Zhaohuan Zhu, Ph.D.
Examination Committee Member

Stephen Lepp, Ph.D.
Examination Committee Member

Monika Neda, Ph.D.
Graduate College Faculty Representative

Alyssa Crittenden, Ph.D.
*Vice Provost for Graduate Education &
Dean of the Graduate College*

ABSTRACT
ON OUTFLOWS DUE TO RADIATION

By

Randall Cody Dannen

Dr. Daniel Proga, Examination Committee Chair
Professor of Physics & Astronomy
University of Nevada, Las Vegas

Observations of ionized AGN outflows have provided compelling evidence that the radiation field transfers both momentum and energy to the plasma. At parsec scale distances in AGN, energy transfer can dominate, in which case the only force needed to launch an outflow is due to gas pressure. Much closer to the black hole, gravity dominates thermal energy due to insufficient heating by the radiation and the gas is in the so-called 'cold wind solution' regime. Only magnetic or radiation forces can lead to outflow, but it is unclear how these forces depend on the spectral energy distribution (SED) and the ionization parameter. To accurately compute the radiation force, it is still necessary to know the gas temperature, both of which require detailed accounting of the microphysics. By surveying the parameter space of radiation forces resulting from various temperature blackbody, AGN, and X-ray binary SEDs while simultaneously computing the heating and cooling balance to determine the temperature, I will characterize and quantify how the resulting wind properties depend on the assumed SED and ratio of gravitational binding energy and gas thermal energy.

TABLE OF CONTENTS

ABSTRACT	iii
LIST OF TABLES	vi
LIST OF FIGURES	x
CHAPTER 1: Active Galactic Nuclei	1
1.1 AGN Power Generation: Supermassive Black Holes	3
1.2 Motivation for Clouds	5
1.2.1 Warm Absorbers	5
1.2.2 Broad and Narrow Absorption Lines	7
1.2.3 Ultra Fast Outflows	8
1.2.4 Broad Line Region	8
1.2.5 Narrow Line Region	8
1.3 Changing Look AGN: NGC 5548	9
CHAPTER 2: Photoionization and Radiative Force Multiplier	11
2.1 Photoionization	11
2.2 Radiative Line Driving	11
2.3 Methodology	13
2.4 Atomic Line Lists	15
2.5 Force Multiplier Calculations	17
2.6 Results Using AGN SED	22
2.7 Discussion of Force Multiplier Calculations	25
CHAPTER 3: Heating and Cooling Photoionized Gas and TI	27
3.1 Basic Equations of Hydrodynamics	27
3.1.1 Thermal Instability (TI)	29
3.2 Numerical Considerations and Simulation Setup	30
3.3 Results	33
3.3.1 Unsteady, Clumpy Wind Solutions	34
3.3.2 Smooth Wind Solutions Passing Through a TI Zone	37
3.3.3 Clumpy Winds in 2-D	38
3.4 Discussion of Thermally Driven Winds and Their Clumpiness	40
CHAPTER 4: Thermally and Line Driven Winds	42
4.1 Scaling Relations	46
4.2 Simulation Setup	49
4.3 Results	52
CHAPTER 5: Discussion of Results & Future Work	59

APPENDIX A: LTE VS. non-LTE Calculations	63
APPENDIX B: The Equilibrium Temperature and Force Multiplier	66
BIBLIOGRAPHY	73
CURRICULUM VITAE	82

LIST OF TABLES

<p>Table 2.1: Table showing the top five contributing lines to the force multiplier for AGN1 (left column) and AGN2 (right column) for fixed $t = 10^{-6}$ and selected values of ξ. Note that the value of ξ in the bottom section of the table differs in the each column; it is intended to correspond to the bump in the M_{max} distribution at large ξ (see the black lines in fig. 2.5).</p>	23
<p>Table 3.1: Summary of key parameters and results. HEP is the hydrodynamic escape parameter. The inner radius is derived from the choice of HEP as $r_0 = (1 - \Gamma) GM_{\text{BH}} \text{HEP}^{-1} c_{s,0}^{-2}$ (see Eq. 3.5), while the density at the base follows from the definition of ξ as $\rho_0 = \mu m_p L_X \xi_0^{-1} r_0^{-2}$. The sound crossing time is defined as $t_{\text{sc},0} = (r_{\text{out}} - r_0)/c_{s,0}$. The ratio $t_{\text{cool}}/t_{\text{sc}}$ is given at the location where $\Xi = \Xi_{\text{c,max}}$. The average mass flux and velocity through r_{out} are shown as $\langle \dot{M} \rangle$ and $\langle v \rangle$. Comment columns denote the state of the flow at late times. Values/comments in parenthesis denote results for the 8x-resolution runs.</p>	32
<p>Table 4.1: Example of input parameters for three SED cases with $\text{HEP}_0 = 5$: 4×10^5, 8×10^5, and 10^6 BB SED, second, third, fourth column, respectively. For all models, we assumed $M = 10 M_\odot$, $\Gamma = 0.2$, and $\xi_0 = 80$. In addition, we set T_0 to T_{eq} corresponding to ξ_0 for a given SED. Therefore, the inner radius and the density at the base depend only on HEP_0 and we compute them using the following expressions $r_0 = (1 - \Gamma) GM \text{HEP}_0^{-1} c_{s,0}^{-2}$ (see Eq. 3.5) and $\rho_0 = \mu m_p L_{\text{Edd}} \Gamma \xi_0^{-1} r_0^{-2}$ facilitating the definition of ξ. For a reference, we also list Ξ_0 (see Eq. 4.5). We explored models with HEP_0 ranging from 5 to 500 (see Table 4.2).</p>	50
<p>Table 4.2: List of the simulations considered in this work and summary of some gross properties of the wind solutions. The first column list the model case, from the top to the bottom: self-consistent model with radiative heating and cooling and line driving based on the results from photoionization calculations for 4×10^5, 8×10^5, and 10^6 BB SEDs, isothermal model using the CAK, and two modified CAK expression for line driving with $\delta = 0.1$ and 0.3. The second column list HEP_0 value. The third and fourth column lists the wind mass loss rate and momentum efficiency, \dot{M}_w and $\eta_{\text{wind}} \equiv \dot{M}_w v_{\text{out}} c / (L_{\text{Edd}} \Gamma)$, respectively. We plot these two and other wind properties as functions of HEP_0 in Fig. 4.3. Finally, the last column provides the information whether the wind solution reached a steady state or remained variable.</p>	51

LIST OF FIGURES

Figure 1.1:	Artistic impression of a AGN courtesy of Nima Abkenar.	1
Figure 1.2:	Schematic representation of the spectral energy distribution (SED) of an unobscured AGN (black curve), separated into the main physical components (colored curves) and compared to the SED of a star-forming galaxy (gray curve). Figure and caption from Hickox and Alexander (2018)	2
Figure 1.3:	Schematic representation of how line of sight and spectral features effect AGN classification. Image credit: J. E. Thorne	4
Figure 1.4:	Summary of different ionized outflows detected in AGN and their average physical parameters. Note that there is considerable diversity in the properties of each type of outflows depending on the nature of the central AGN, and there is substantial overlap in parameter space of the different outflows. Figure from Laha et al. (2020).	6
Figure 1.5:	Image of NGC 5548 taken by the Hubble Space Telescope.	9
Figure 2.1:	<i>Top panel:</i> Two representative AGN SEDs used in our calculations: AGN1 represents the unobscured SED (solid line) while AGN2 represents the obscured SED (dashed line) of the AGN in NGC 5548. We use different color shading to show the UV and X-ray energy bands. The two vertical green lines mark the energy interval used to calculate ξ (13.6 eV – 13.6 keV). <i>Bottom panel:</i> Fraction of the total energy of the SEDs in each energy component band for AGN1 (solid lines) and AGN2 (dashed lines). We also show the fraction of the total energy used in computing ξ (i.e., the fraction of the total energy between the vertical green lines in the top panel).	14
Figure 2.2:	Histograms illustrating properties of the lines used in our calculations. <i>Left panel:</i> Solid lines indicate the number of lines as function of energy in units of eV for the atomic database used in this work (black line) and used in SK90 (green line). For emphasis, we shade in blue the energy range for UV photons and in red for the X-rays. <i>Middle panel:</i> Number of lines as a function of oscillator strength gf for the entire line list (black line), including only the UV lines (blue line), and only X-ray lines (red line). <i>Right panel:</i> Number of lines as a function of ionization degree for the atomic database used in this work (black line), UV lines only (blue line), X-ray lines only (red line), and the atomic database used in SK90 (green line).	16
Figure 2.3:	Summary of results from our photoionization and line force calculations. <i>Top panels:</i> The force multiplier $M(\xi, t)$ as a function of ξ for an optically thin gas with small optical depth parameter, $t = 10^{-6}$, for AGN1 (left) and AGN2 (right). This small value of t yields a proxy for M_{\max} . Plotted against the left vertical axes are values of M_{\max} due to all lines (solid blue curve), UV lines only (dashed red curve) and X-ray lines only (dash-dotted green curve). Plotted against the right vertical axes is the photoionization equilibrium temperature determined by XSTAR corresponding to $\mathcal{L} = 0$ (solid black line). The shaded regions indicate the parameter space where the gas is thermally unstable by the isobaric criterion (i.e., $[\partial \log T / \partial \log \xi]_{\mathcal{L}} \geq 1$; (e.g., Barai et al., 2012)). <i>Bottom panels:</i> The opacity of the single strongest UV and X-ray line as a function of ξ (dashed red and dash dotted green curves, respectively). The line opacity is in units of electron scattering opacity (see Eq. 2.14).	18

Figure 2.4: The main results from our photoionization and line force calculations. *Top panels:* These correspond to AGN1. The left panel shows our results as a function of t for a fixed ξ . The solid lines show results for a fixed ξ [from top to bottom, ξ increases from 10^{-2} (violet region) to 10^5 (red region)], and the ξ levels are separated by $\Delta \log(\xi) = 1$. The right panel shows results of our force multiplier calculations as function of ξ for a fixed t . The solid lines show results for a fixed t [from top to bottom, t increases from 10^{-8} (violet region) to 10 (red region)], and the t levels are separated by $\Delta \log(t) = 1$. *Bottom panels:* Same as the top panels for AGN2. 19

Figure 2.5: Main contributors to the total force multipliers. The left panels correspond to AGN1 and the right panels correspond to AGN2. The solid black line in each panel represents the total force multiplier for $t \simeq 10^{-6}$ (our proxy for M_{\max}). The top panels shows the contribution to M_{\max} for various elements of interest (see the legend in the bottom left corner of the top left panel). Similarly, the bottom panels show the contribution of various ions (see the legend in the bottom right corner of the bottom left panel). 22

Figure 3.1: *Top panel:* SED intrinsic to NGC 5548, as determined by Mehdipour et al. (2015). The energy range used to define ξ is marked by the two vertical lines. This SED is relatively flat and has $L_X/L \approx 0.36$ and mean photon energy $\langle h\nu \rangle = k_B T_X = 34.8$ keV (corresponding to Compton temperature $T_C = T_X/4 = 1.01 \times 10^8$ K). *Bottom panel:* Associated S-curve and Balbus contour (the solid and dashed lines, respectively). Red dots mark the points $\Xi_{c,\max}$, Ξ_1 , Ξ_2 , and $\Xi_{h,\min}$. Note that $\Xi_{c,\max}$ ($\Xi_{h,\min}$) denotes the last (first) stable point on the “cold phase branch” (“Compton branch”) of the S-curve. The SED-dependent conversion to the other common ionization parameter $U = (\Phi_H/c)/n$ (with Φ_H the number density of H ionizing photons) is $U \approx \xi/42$, so $[\log(\Xi_{c,\max}), \log(\xi_{c,\max}), \log(U_{c,\max})] = [1.10, 2.15, 0.53]$ 30

Figure 3.2: Phase diagram comparison of our four 1-D models showing T as function of Ξ in relation to the thermal equilibrium curve (black solid line) and the Balbus contour (black dashed line). The colored solid lines display time-averaged solutions and the less opaque lines a single snapshot at the end of the simulation (at $t > 3 t_{\text{sc},0}$). The top row presents our standard resolution (‘-1x’) runs and the bottom row our high (‘-8x’) resolution runs. See §2.6 and §3.4 for details about the dynamics of each model. 33

Figure 3.3: Spatial low profiles of our four 1-D models run at both medium (‘-1x’ runs, the first and third columns of panels) and high (‘-8x’ runs, the second and fourth column of panels) resolution. As in Fig. 2, fully opaque curves show time-averaged profiles, while less opaque ones are snapshots from the end of the simulation. The X’s mark sonic points of the time-averaged solutions. In the temperature panels, the dotted black line shows where $T = T(\Xi_{c,\max})$. Animations of these runs are downloadable at <https://doi.org/10.5281/zenodo.3739603> or watchable at <http://www.physics.unlv.edu/astro/clumpywindsims.html>. 36

Figure 3.4: 2-D version of model B. *Bottom Panels:* Log-scale maps of T (left) and ρ (right) in cgs units. *Top Panels:* The relative difference of T (left) and ρ (right) computed using time averaged values. Bright green contours display sonic surfaces. 39

Figure 4.1: Example of results from our photoionization calculations for four SEDs: from left to right, blackbody SEDs with temperatures 4×10^5 K, 8×10^5 K, 10^6 K, and an unobscured AGN SED (AGN1; Mehdipour et al., 2015). *Top panels:* colormap of the force multiplier for t going from $\log t = 1$ (red) to $\log t = -8$ (blue). Black dotted lines mark $M(t, \xi)$, while gray lines indicate $M(t, \xi)$ at $\log t = -1, -2, \dots, -8$. The horizontal dashed line marks the value $M(t, \xi) = 10$, to indicate the level above which line driving can be the dominant outflow driving mechanism. The solid black line is the equilibrium temperature (or S-curve), T_{eq} , in units of 10^4 K. *Bottom panels:* profiles of $\alpha(\xi)$, $k(\xi)$, $|\delta(\xi)|$, and $M_{\text{max}}(\xi)/k(\xi)$ (blue, black dashed, green, and red curves, respectively), the four parameters characterizing the behavior of the force multiplier. To mark negative values of δ we added green squares to the green line in the right panel. The first three parameters are computed along the $t = 1$ curves above to relate our numerical results of the force multiplier to the modified CAK formula. The fourth parameter, $M_{\text{max}}(\xi)/k(\xi)$, is estimated, using $M(t = 10^{-8}, \xi)$ (the upper envelope of the curves above) as a proxy of the maximum force multiplier, $M_{\text{max}}(\xi)$. See Appendix A for more details. 44

Figure 4.2: The force multiplier as a function of ξ for a subset of our wind solutions. Each panel shows results for $\text{HEP}_0=5, 50, \text{ and } 500$ (red, green, blue curves) our six cases presented in this work: 1) CAK (i.e., $\delta = 0$ top left panel); 2) mCAK with $\delta = 0.1$ (top middle panel); 3) mCAK with $\delta = 0.3$ (top right panel); and 4-6) $4, 8, 10 \times 10^5$ BB SED cases (the bottom panels, from left to right). For a reference, in each panel we also plot the force multiplier as a function of ξ for fixed values of optical depth parameter, t : $\log t = -8, -7, \dots, 0, 1$. In the top panels, the solid lines are by design straight lines, equally spaced and with the slope equal to $-\delta$ (see the appendix including Eq. B.2). In the bottom panels, the force multiplier is computed based on the photoionization calculations and its t and ξ is more complex, for example the solid lines converge for small t which reflects the saturation of $M(t, \xi)$ as t approaches zero. This saturation is most apparent for the 8×10^5 BB SED case and has a significant effect on the wind solution especially for high HEP_0 simulations where the solution is highly time dependent. 53

Figure 4.3: Comparison of the gross properties of our wind solutions as a function of HEP_0 . From top to bottom, those quantities shown are the mass flux, wind momentum efficiency $\eta_{\text{wind}} = v\dot{M} (c / (\Gamma L_{\text{Edd}}))$, velocity as the gas exits the outer grid cell in units of escape velocity defined at the inner radius ($v_{\text{esc}} = \sqrt{2GM/r_0}$), v_{out} velocity at the inner radius, v_0 , and optical depth parameter at the inner radius, t_0 . The horizontal black dashed line in the top panel represents $\dot{M}_{w, \text{CAK}}$ (see Eq. 4.2). 55

Figure 4.4: Properties of winds for the 4×10^5 BB SED case. We show three solutions that correspond to $\text{HEP}_0 = 5, 50, 500$ (red, green, and blue lines respectively). Proceeding left to right, the first panel shows the density in units of the density at r_0 , ρ/ρ_0 . The second panels shows the radial velocity. The third panel shows both force multiplier, $M(t, \xi)$ (solid), and the line optical depth parameter, t (dashed), as functions of radius. Fourth panel displays the radiation force, F^{rad} , and gas pressure, F^{th} , normalized to the force of gravity, F^{grav} , as a function of radius. The final right most panel shows the phase diagram (i.e., $\log T$ vs. $\log \xi$) for all three wind solutions. The solid black curve corresponds to the thermal equilibrium ("S-curve", i.e. where $T = T_{\text{eq}}(\xi)$). The x's and squares in matching color on each curve mark the sonic and critical radii, respectively). 57

Figure A.1: Comparison of LTE and non-LTE force multiplier calculations for AGN1 (left) and AGN2 (right), assuming $t = 10^{-6}$. *Top Panels:* The solid black line is $M(\xi, t)$ from Fig. 2.3 that assumes a Boltzmann distribution for the level populations. The blue dash-dotted line is $M(\xi, t)$ found without making the Boltzmann distribution assumption but with the level populations determined by XSTAR and including only lines contained in XSTAR. *Bottom Panels:* The black dash-dotted line is the ratio of the blue dash-dotted and black solid lines, illustrating how the combination of a smaller line list and a non-LTE treatment of the level populations reduces $M(\xi, t)$ 65

Figure B.2: Parameter survey of photoionization results for the two AGNs and two XRBs SEDs (top row of pair of panels), and ten blackbody SEDs of different temperatures. From left to right, from second top row of panels to bottom, the SEDs correspond to BBs with $T = 2 \times 10^4$ K, 4×10^4 K, 6×10^4 K, 8×10^4 K, 10^5 K, 2×10^5 K, 4×10^5 K, 6×10^5 K, 8×10^5 K, 10^6 K. The first four SEDs correspond to an unobscured and obscured AGN (AGN1 and AGN2; Mehdipour et al., 2015) and hard and soft state XRBs (XRB1 and XRB2; Trigo et al., 2013). *Top panels:* colormap of the force multiplier for t going from $\log t = 1$ (red) to $\log t = -8$ (blue). Black dotted lines mark $M(t, \xi)$, while gray lines indicate $M(t, \xi)$ at $\log t = -1, -2, \dots, -8$. The horizontal dashed line marks the value $M(t, \xi) = 10$, to indicate the level above which line driving can be the dominant outflow driving mechanism. The solid black line is the equilibrium temperature (or S-curve), T_{eq} , in units of 10^4 K. *Bottom panels:* profiles of $\alpha(\xi)$, $k(\xi)$, $|\delta(\xi)|$, and $M_{\text{max}}(\xi)/k(\xi)$ (blue, black dashed, green, and red curves, respectively), the four parameters characterizing the behavior of the force multiplier. To mark negative values of δ we added grey squares atop the green line. 71

Figure B.3: Parameter survey of our line force result for the ten BB SEDs of different temperatures, XRB, and AGN SEDs with increasing mean photon energy from left to right. The parameters of interest from top to bottom are M_{max} , k , the ratio of M_{max} and k , maximum line opacity η_{max} , α , and δ . The color of the of each point corresponds to $\log \xi$ shown in the color bar along the top (red corresponding to low ionization and blue with high ionization). The circled points correspond to where $\log \xi = -2, -1, 0, 1, 2, 3, 4, 5$, and the vertical lines are for reference but also indicate where $\xi \approx 30$ for each SED. . . 72

CHAPTER 1: ACTIVE GALACTIC NUCLEI



Figure 1.1. Artistic impression of a AGN courtesy of Nima Abkenar.

Active Galactic Nuclei (AGN) are the brightest objects in the universe located at the center of active galaxies and represent the growth phase of supermassive black holes (SMBH). Astronomers have been working to understand what AGN look like and the physics underlying them for over 100 years (Fath, 1909), and owing to their complex nature, AGN have had many names. Commonly nearby AGN were often referred to as Seyfert Galaxies, and further galaxies referred to as quasars,

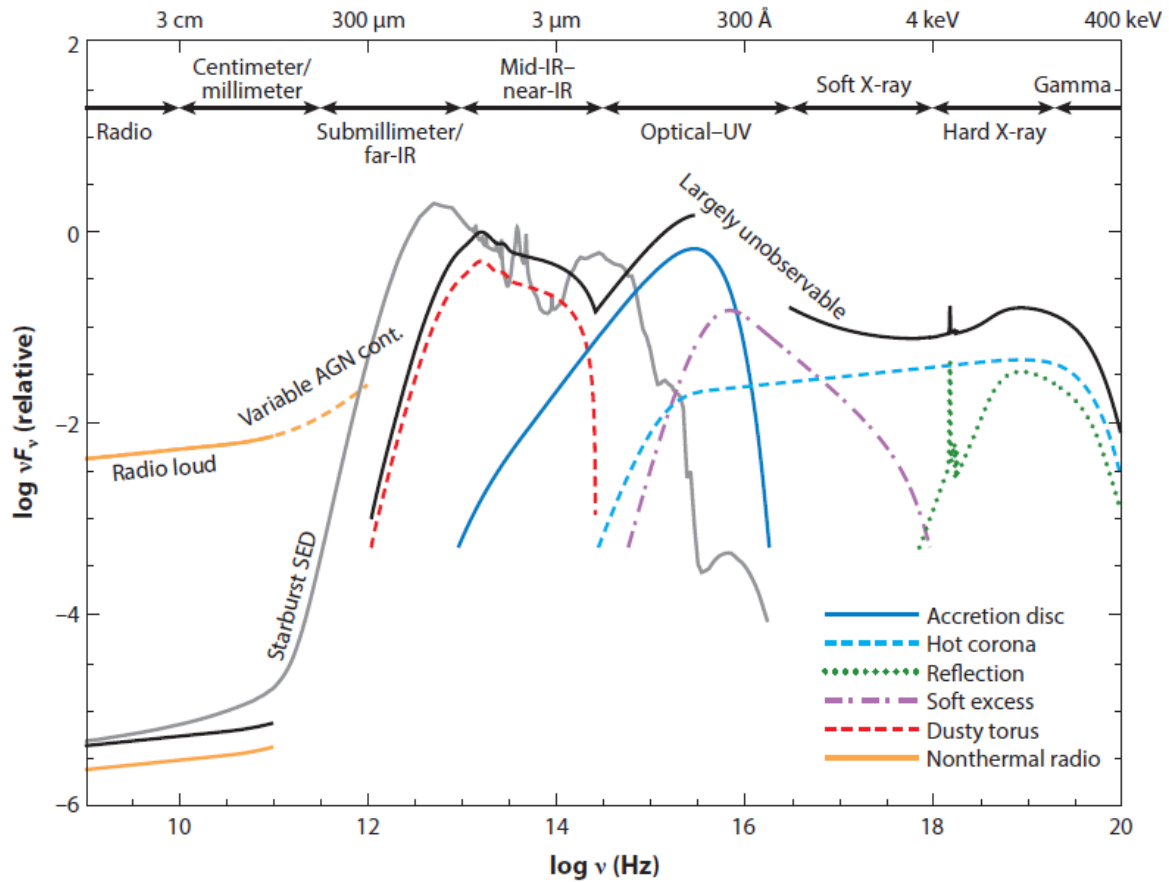
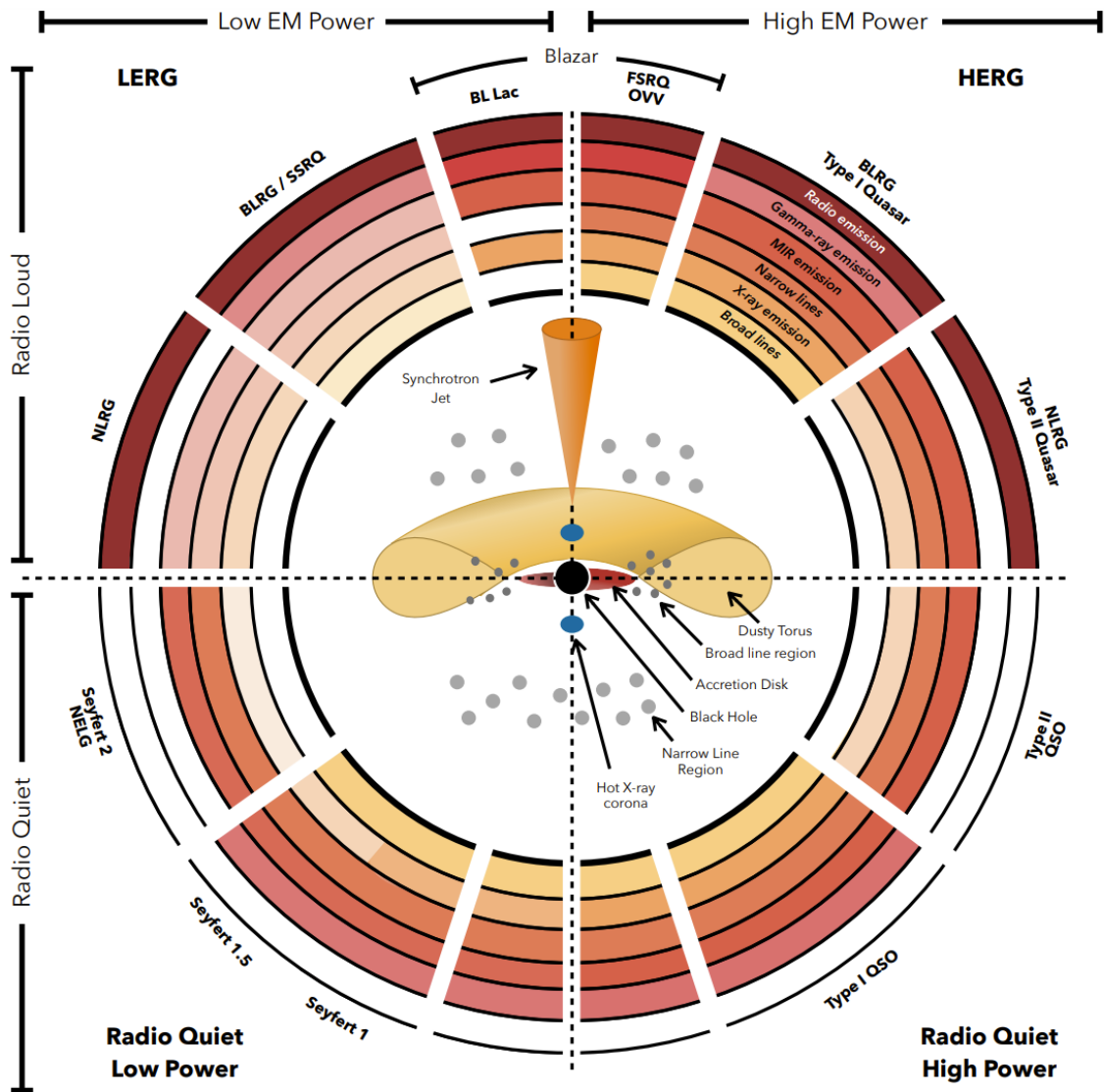


Figure 1.2. Schematic representation of the spectral energy distribution (SED) of an unobscured AGN (black curve), separated into the main physical components (colored curves) and compared to the SED of a star-forming galaxy (gray curve). Figure and caption from Hickox and Alexander (2018)

quasi stellar objects, and QSOs not understanding that they were all AGN (Seyfert, 1943; Salpeter, 1964; Lynden-Bell, 1969). After the introductory chapter describing the basic properties of AGN and evidence for clouds, Chapter 2 will discuss how we compute the force due to spectral lines, the force multiplier, $M(t, \xi)$. Chapter 3 will discuss winds due to thermal driving and results from simulations. Chapter 4 discusses line driven winds with and without heating due to the same radiation force and important factors that impact the efficiency of line driving. Generally gas is assumed to be in local thermal equilibrium (LTE), however non-LTE calculations for $M(t, \xi)$ will be presented in Appendix A and in B we will discuss the important role of temperature when computing $M(t, \xi)$.

1.1 AGN Power Generation: Supermassive Black Holes

Although AGN are typically identified and classified based on observational features, there is no precise physical definition. According to Netzer (2013), any galaxy that hosts an actively accreting SMBH is considered an AGN. The prevailing notion is that all large galaxies have central SMBHs as well as many small galaxies, notably those with bulges. It is the broadly accepted view that there exists an accretion disk around the SMBH of viscous, optically thick gas that emits thermally with temperatures ranging $T \approx 10^{4-5}$ K (referred to as the standard accretion disk or α -disk model, Shakura and Sunyaev, 1973; Rees, 1984), emitting strongly in the optical and UV spectral bands. Although that is far from the only component of the AGN SED (see Fig. 1.2 for a schematic presentation of the different components of the SED). Another possible component of AGN emission which this work will not touch on are jets, with two broad classifications: Blazars, emitting broadly but powerful emitters of γ -rays and radio galaxies, characterized by extended radio lobes emitting far from the galactic center due to jets powered by the SMBH. As mentioned in the previous it is thought that the different classifications of AGN are due to line of sight effects



J. E. Thorne

Figure 1.3. Schematic representation of how line of sight and spectral features effect AGN classification. Image credit: J. E. Thorne

and whether or not there’s material between the viewer and the central SMBH (Urry, 2004), see Fig. 1.3 for a schematic of how the presence of spectral features and line of sight determine AGN classification.

Evidence suggests that these galaxies and their black holes have co-evolved, as the masses of SMBHs and the properties of their host galaxies are closely linked (Magorrian et al., 1998; Ferrarese and Merritt, 2000; Gebhardt et al., 2000). This implies that a significant proportion of galaxies, around 99%, do not accrete enough gas to be classified as ”active” galaxies. However, they do accrete gas in a subdued manner, as demonstrated by the exceptionally faint appearance of the low-luminosity AGN (LLAGN) such as our own galactic center. These LLAGN likely constitute a substantial fraction of the galaxy population and thus broaden the range of luminosity’s in all AGN, where LLAGN have luminosity in the range $L \sim 10^{40-42}$ erg, Seyfert galaxies and low-luminosity QSOs span the next three orders of magnitude, $L \sim 10^{43-46}$, and high-luminosity QSOs can have $L \sim 10^{44-48}$ (Giustini and Proga, 2019).

1.2 Motivation for Clouds

In the spectra of AGN, we often observe spectra signatures from different sources of absorption and emission. Fig. 1.4 shows a summary of the different ionized outflows we’ll discuss in this section: Warm absorbers (WAs), broad absorption lines (BALs), narrow absorption lines (NALs), ultra fast outflows (UFOs), broad line region (BLR), narrow line region (NLR). This section will conclude with a brief over view of the “changing look AGN”, NGC 5548, whose intrinsic SED is used in many of our studies and an AGN that show the potential for clump formation.

1.2.1 Warm Absorbers

From early observation of AGN, there has been evidence of absorption from ionized gas, so-called warm absorbers, in the soft X-ray spectra (Halpern, 1984; Reynolds and Fabian, 1995a).

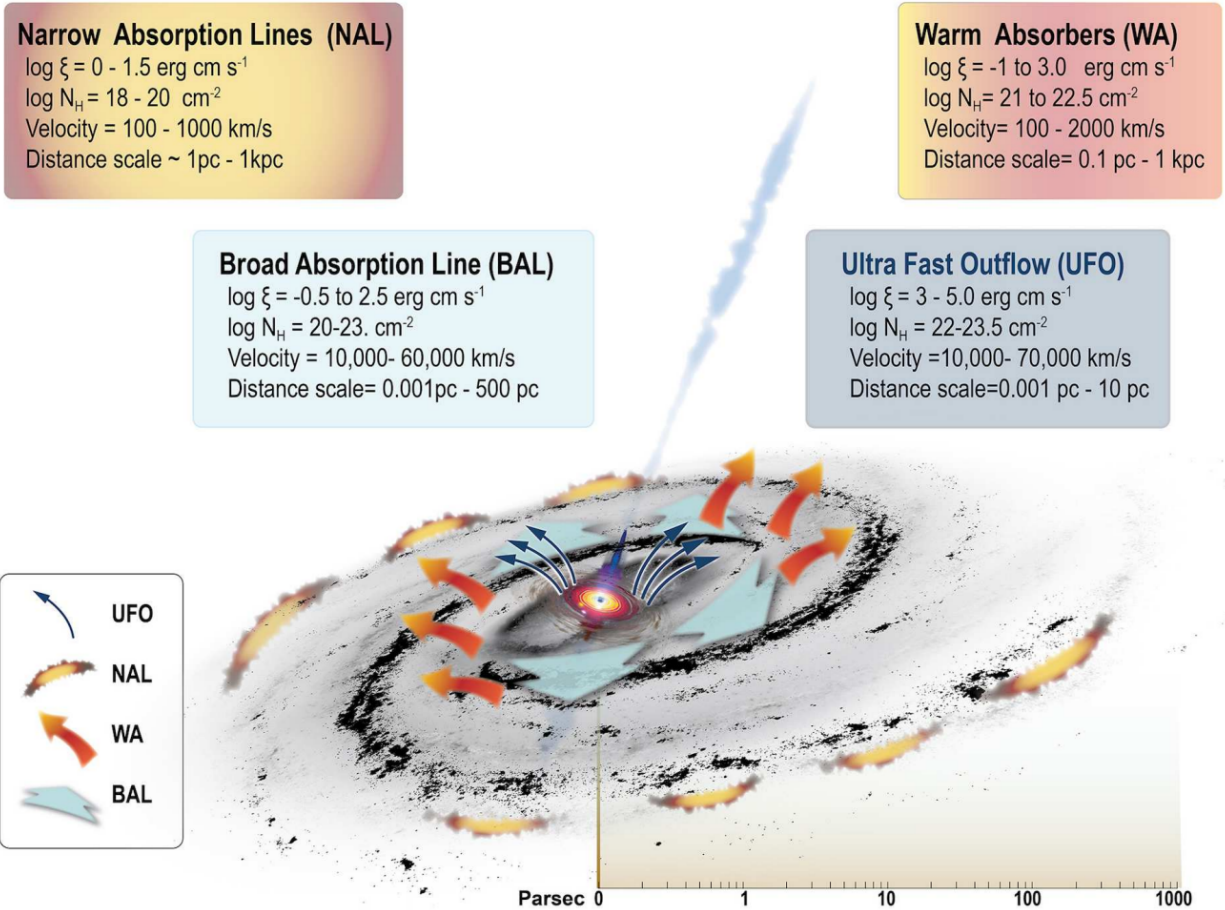


Figure 1.4. Summary of different ionized outflows detected in AGN and their average physical parameters. Note that there is considerable diversity in the properties of each type of outflows depending on the nature of the central AGN, and there is substantial overlap in parameter space of the different outflows. Figure from Laha et al. (2020).

WAs are clouds of partially ionized gas commonly found in the vicinity of AGN and are thought to be principally responsible for the hard-UV and X-ray opacity along our line of sight. While the physical properties of warm absorbers are still not fully understood, they are thought to be composed of gas that is at a temperature of a few thousand degrees Kelvin with moderate to full ionization and outflowing from within 10^2 pc of central SMBH. Absorption features from H- and He-like C, O, N, Ne, Mg, Al, and S ions show that typical outflow velocities range from 100–2000 km s^{-1} (Kaspi et al., 2002). Typical densities range from $n_e = 10^{4-11} \text{ cm}^{-3}$ and occupy between 0.1pc–1 kpc away from the SMBH. This outflowing material plays an important role in galactic feedback by regulating the growth of the SMBH and transporting material and momentum to interstellar medium (ISM).

1.2.2 Broad and Narrow Absorption Lines

BALs and NALs are spectral features indicating the presence of high velocity AGN outflows, both of which can be found with velocities up to 10,000 km s^{-1} . As their names imply, BALs tend to be much broader absorption features with FWHM $> 3000 \text{ km s}^{-1}$ with minimum outflow velocities $> 5000 \text{ km s}^{-1}$. NALs on the other hand, have typical velocities of about 1000 km s^{-1} and narrow FWHM (Weymann et al., 1981; Hamann et al., 2011; Chen and Pan, 2017). The likely difference in the velocities is due to their launching locations. BALs and NALs also tend to be seen in different parts of the spectrum; BALs are typically seen in the UV where NALs tend to be seen in the optical and near infrared, and BALs are typically correlated with AGN luminosity, indicating that the SMBH is actively accreting. This in turn will heat up the surrounding gas, resulting in an outflow. NALs tend to be associated with radio emission where BALs are not (Knigge et al., 2008; Hamann et al., 2018).

1.2.3 Ultra Fast Outflows

Ultra fast outflows (UFOs) are relatively new addition to the study of AGN outflows with velocities that are a considerable fraction of the speed of light, ranging up to $\sim 0.3c$. These UFOs show a high degree of ionization due to their inclusion of absorption in the X-ray belonging to 25 XXV and 25 XXVI K-shell lines. Once thought to be rare, an archival search of the data from *XMM-Newton* and *Suzuki* revealed that UFOs maybe more common than previously that, appearing in about 35% of the galaxies surveyed (Tombesi et al., 2010a; Gofford et al., 2013; Tombesi et al., 2013).

1.2.4 Broad Line Region

The BLR is a region of gas that surrounds the supermassive black hole at the center of an AGN and thought to be responsible for the broad emission lines that are seen in the spectra of AGN with $\text{FWHM} > 25,000 \text{ km s}^{-1}$ (Strateva et al., 2003). Thought to be a very complex region since it's structure is still not well understood. However, it is thought to be comprised of a large number of relatively small highly ionized clouds of gas orbiting the central SMBH with velocities in the few thousand km s^{-1} range and with $T \approx 10^4 - 10^5 \text{ K}$. These observed broad emission lines have been vital to our understanding of AGN, since they allow us to estimate the velocities of these clouds and line intensity can be used to gives estimates of the temperature.

1.2.5 Narrow Line Region

The NLR is the gas thought responsible for the narrow emissions lines, $\text{FWHM} < 25,000 \text{ km s}^{-1}$, that are seen in the spectra of AGN and located on scales of 100–1000 pc from the central engine of the AGN. The NLR is thought to be comprised of ionized clouds of gas ionized by the central source moving away from the SMBH with velocities estimated in the few hundred km s^{-1} range and with $T \approx 10^4 \text{ K}$ from observed emission lines. These observed narrow emission lines are correlated with radio emission from AGN, and thought to be produced by the recombination of electrons with

ionized atoms and this allow to make velocity and temperature estimates of these outflowing clouds (Bennert et al., 2002).

UFOs, NLR, BLR, and WAs are all thought to be important components of the galactic feedback process, regulating the growth of the central SMBH and by transporting energy and material to the ISM and suppressing star formation.

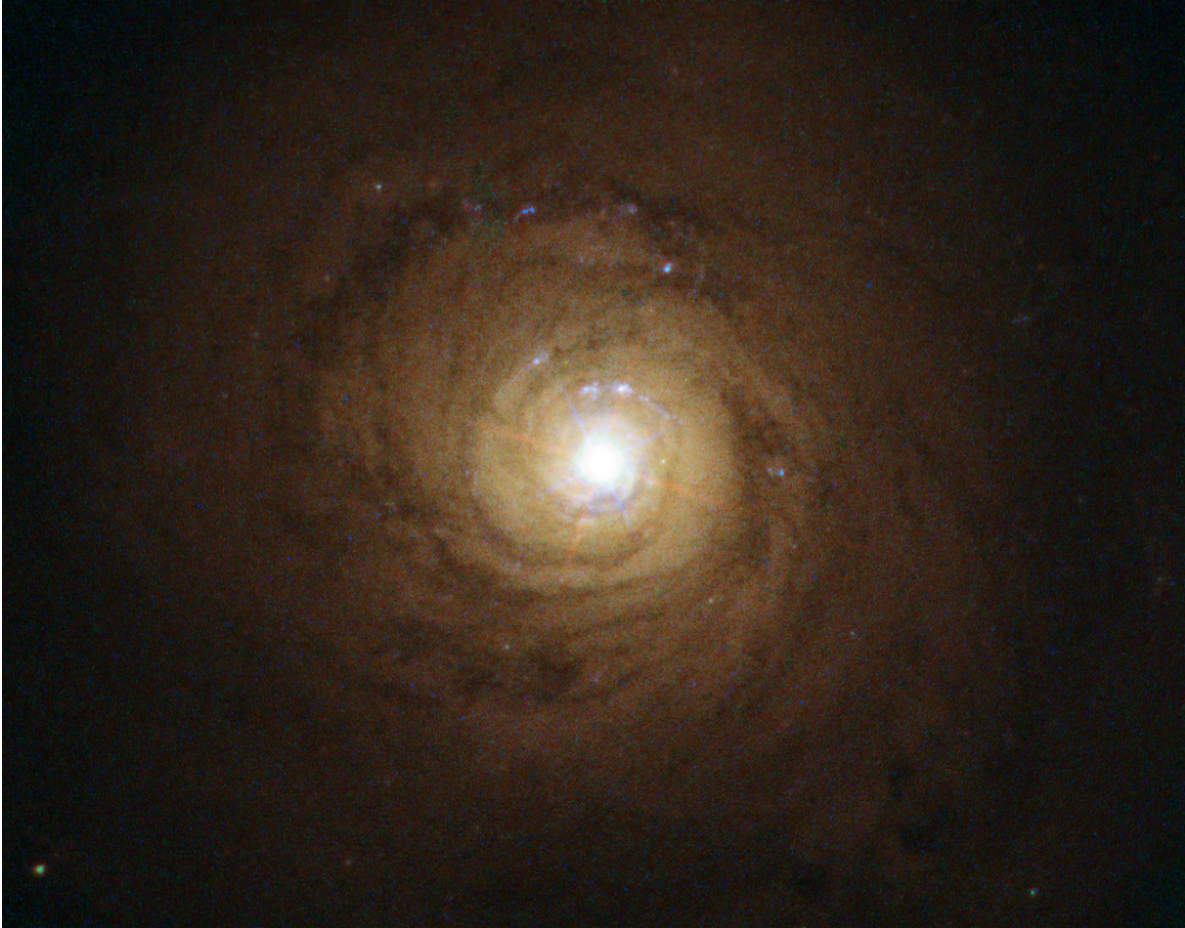


Figure 1.5. Image of NGC 5548 taken by the Hubble Space Telescope.

1.3 Changing Look AGN: NGC 5548

NGC 5548, a Seyfert galaxy, was first discovered in 1787 by William Herschel; one of twelve nebulae listed by American astronomer Carl Keenan Seyfert in 1943 that showed broad emission lines in their nuclei, excess in the radio emission, X-rays confined to near the center of the galaxy,

and ionized outflows in excess of 450 km s^{-1} (Kaastra et al., 2014). First noted in 2013 and continuing even to now, this AGN has been closely studied due to its extreme variability in X-ray emission, earning moniker “changing look AGN” (see Fig. 2.1 for examples of NGC 5548’s SED in the obscured and unobscured states). Due to the extreme size of AGN, their variability tends to not be on time scales too long for astronomers to observe them happening in real time, but this fortunate observations is allowing us to get a deeper understanding of how AGN operate. This change in brightness is thought to be caused by some obscurer, possibly WAs, moving into our line of sight between the central source and not an underlying change in the intrinsic SED, and this gas may provide the shielding thought to be required for line driven winds to form (Mehdipour et al., 2015, 2016).

CHAPTER 2: PHOTOIONIZATION AND RADIATIVE FORCE MULTIPLIER

2.1 Photoionization

Simply put, photoionization is one of the processes by which an atom (or molecule) is ionized by absorbing a photon with enough energy to have an electron removed. Plasma codes such as XSTAR (Kallman and Bautista, 2001) and CLOUDY (Ferland et al., 2017) can be used to model these features, as they perform detailed photoionization, radiative transfer, and energy balance calculations. Several groups have begun incorporating these calculations into hydrodynamical codes, and this is currently the most accurate approach for comparing theory with observations (e.g., Salz et al., 2015; Ramírez-Velasquez et al., 2016; Kinch et al., 2016; Dyda et al., 2017; Higginbottom et al., 2017).

It is useful to define the photoionization parameter

$$\xi = \frac{L_X}{nr^2} \quad (2.1)$$

where L_X is the luminosity integrated from 1–1000 Ry, n is the number density of hydrogen nucleons, and r is the distance from the source. Another useful form when dealing with isobaric gas,

$$\Xi = \frac{\xi}{ck_B T} \quad (2.2)$$

2.2 Radiative Line Driving

AGN are examples of astrophysical objects that are extremely luminous radiation sources over a broad range of energies. A consequence of such efficient conversion of gravitational binding energy is the production of outflows in the form of relativistic jets and winds of ionized gas with velocities approaching a few percent the speed of light (e.g., Kaspi et al., 2002; Chartas et al., 2002; Tombesi et al., 2010b; Reeves et al., 2018). Radiative and mechanical AGN feedback may play an important role in the evolution of the host galaxy (Silk and Rees, 1998; Furlanetto and Loeb, 2003; Haiman

and Bryan, 2006; Hopkins et al., 2006; Ciotti et al., 2010; McCarthy et al., 2010; Ostriker et al., 2010; Fabian, 2012; Faucher-Giguère et al., 2012; Choi et al., 2014), and the winds in particular are responsible for imprinting a host of spectral features in the optical, UV, and X-ray bands. These features take the form of broad absorption lines, warm absorbers and ultra-fast outflows (Weymann et al., 1991; Reynolds and Fabian, 1995b; Crenshaw et al., 2003; Giustini et al., 2011; Hamann et al., 2013; Kaastra et al., 2014; Nardini et al., 2015; McGraw et al., 2017; Arav et al., 2018), and much work is still required to determine the mechanism by which these outflows form.

Still, even within this modeling framework, a full treatment of the effects of radiation on gas dynamics requires many time consuming calculations, so various further approximations are made. For instance, most theoretical studies of gas flows that include thermal driving neglect or simplify the treatment of the radiation force, f_{rad} , whereas studies of radiation pressure driven flows typically neglect or simplify the radiative heating and cooling rates. In some applications, one could justify ignoring the radiation force by referring to the rule of thumb that “radiation can heat (cool), but frequently finds it difficult to push” (Shu, 1992). However, under some circumstances, radiation can effectively push gas, such as when the total opacity of the gas, κ_{tot} , is dominated by the contribution from photon scattering (thereby providing no energy transfer) rather than from photon absorption (which mainly provides heating). OB stars and cataclysmic variables are examples of objects where the total opacity in their upper atmospheres and winds is dominated by contributions from spectral line transitions, which mostly scatter photons, hence their winds are driven by the so-called line force, $f_{\text{rad,l}}$ (see Castor et al., 1975, CAK hereafter). Early theoretical work suggested that the radiation force can also be the main mechanism driving supersonic gas flows in AGNs (Mushotzky et al., 1972; Arav and Li, 1994; Murray et al., 1995; Proga et al., 2000; Proga, 2007), and numerous observations appear to confirm these expectations (Foltz et al., 1987; Srianand et al., 2002; Ganguly et al., 2003; Gupta et al., 2003; North et al., 2006; Bowler et al., 2014; Lu and Lin, 2018; Mas-Ribas

and Mauland, 2019).

$$f_L = \left(\frac{\Delta\nu F_\nu}{c} \right) \left(\frac{\kappa_L}{\tau_L} \right) (1 - e^{-\tau_L}). \quad (2.3)$$

Where $\Delta\nu$ is the characteristic Doppler width of the transition ($\Delta\nu = \nu v_{th}/c$), F_ν is the specific flux of our radiation field, κ_L is the line opacity, and τ_L is the line optical depth. (Stevens & Kallman 1990). The line opacity per unit mass is given by

$$\kappa_L = \frac{\pi e^2}{m_e c} g f \frac{N_L/g_L - N_U/g_U}{\rho \Delta\nu}. \quad (2.4)$$

Where N_L and N_U are the populations of the upper and lower states, g_L and g_U are their respective statistical weights, and gf is the line oscillator strength. We can express the optical depth of a given line

$$\tau_L = \int_r^\infty \phi \rho \kappa_L dr = \frac{\rho v_{th} \kappa_L}{dv/dr}. \quad (2.5)$$

Building on these definitions, we need define two more parameters

$$t = \frac{\sigma_e v_{th} \rho}{dv/dr}, \quad (2.6)$$

the local optical depth parameter, and

$$\eta = \frac{\kappa_L}{\sigma_e}, \quad (2.7)$$

the line opacity relative to electron-scattering coefficient σ_e . We see that $\tau_L = \eta t$ as well.

2.3 Methodology

In the bottom panel of Fig. 2.1, we mark the fraction of the total energy contained in various portions of the electromagnetic spectrum. We note that the comparison of ratios between the hard and soft UV and X-ray fractional energy is likely an important factor. That is, the quantity of the radiation is clearly important, but the shape of the radiation field is also important. For example,

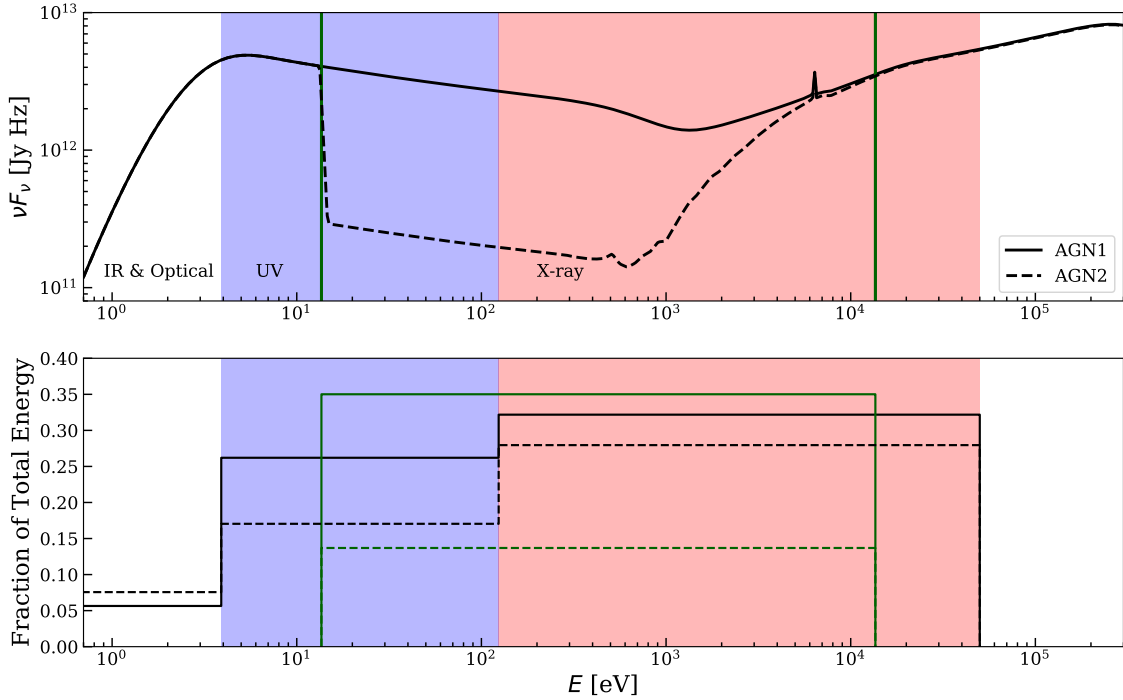


Figure 2.1. *Top panel:* Two representative AGN SEDs used in our calculations: AGN1 represents the unobscured SED (solid line) while AGN2 represents the obscured SED (dashed line) of the AGN in NGC 5548. We use different color shading to show the UV and X-ray energy bands. The two vertical green lines mark the energy interval used to calculate ξ (13.6 eV – 13.6 keV). *Bottom panel:* Fraction of the total energy of the SEDs in each energy component band for AGN1 (solid lines) and AGN2 (dashed lines). We also show the fraction of the total energy used in computing ξ (i.e., the fraction of the total energy between the vertical green lines in the top panel).

modeling of AGN observations requires spectra that are of a certain hardness (e.g., Mehdipour et al., 2015, and references therein). However, only a fraction of the physically relevant SED energy range can be observed. The behavior in the unobservable EUV region, for instance, must be assumed. Additionally, the SED also affects the gas thermal stability (e.g., Kallman and McCray, 1982; Krolik, 1999; Mehdipour et al., 2015; Dyda et al., 2017). In particular, AGN1 and AGN2 both have regions of isobaric thermal instability; we return to this point in §2.5. The deficit of soft photons in AGN2 also allows for isochoric instability, which leads to the formation of non-isobaric clouds (Waters and Proga, 2019). In this context, the AGN is being obscured or not obscured from point of view of the gas and not necessarily the observer.

We present these two SEDs since there is evidence that the evolution of the SED and therefore the gas dynamics may be due to material moving between the AGN and our line of sight (LOS; e.g., Capellupo et al., 2011, 2012). AGN1, the unobscured SED, is the intrinsic SED of the AGN and AGN2, the obscured SED, represents the AGN SED through a column density of material $N_H = 1.45 \times 10^{20} \text{ cm}^2$ (Mehdipour et al., 2015). This allows us to consider situations where the SED incident on the gas experiences the attenuated SED.

2.4 Atomic Line Lists

SK90 considered an X-ray binary system where blackbody radiation from a star drives a stellar wind which was irradiated by X-rays emitted by a companion. Unlike SK90, we assume the radiation field for both the ionizing flux and line driving is the same, as this is more appropriate for modeling gas dynamics in AGNs. Other authors have also explored the line force due to AGNs (e.g. Arav and Li, 1994; Chelouche and Netzer, 2003; Everett, 2005; Chartas et al., 2009; Saez and Chartas, 2011) but they used a different photoionization code (e.g. CLOUDY) and different atomic data sets and line lists.

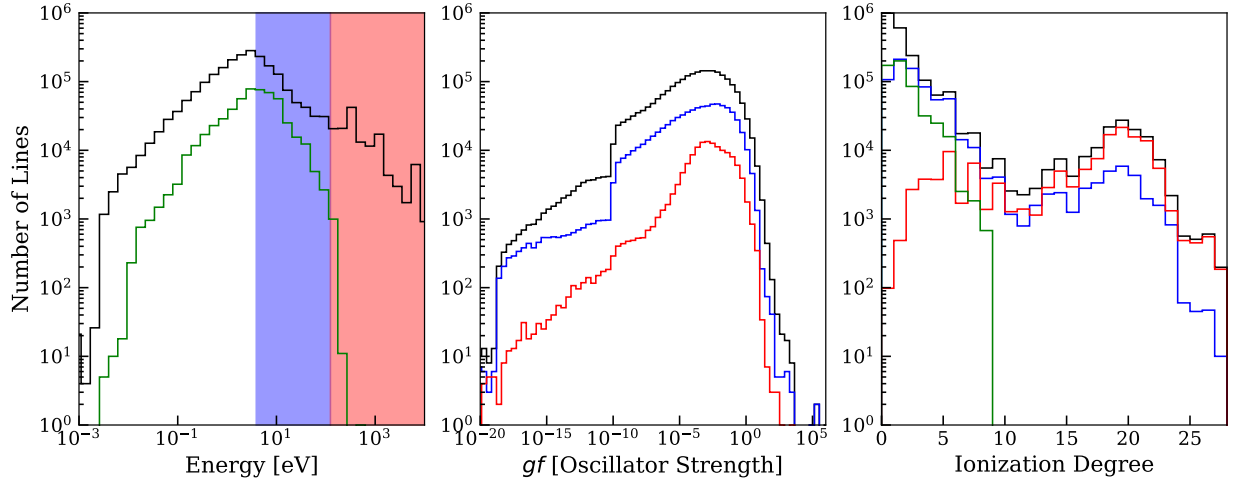


Figure 2.2. Histograms illustrating properties of the lines used in our calculations. *Left panel:* Solid lines indicate the number of lines as function of energy in units of eV for the atomic database used in this work (black line) and used in SK90 (green line). For emphasis, we shaded in blue the energy range for UV photons and in red for the X-rays. *Middle panel:* Number of lines as a function of oscillator strength gf for the entire line list (black line), including only the UV lines (blue line), and only X-ray lines (red line). *Right panel:* Number of lines as a function of ionization degree for the atomic database used in this work (black line), UV lines only (blue line), X-ray lines only (red line), and the atomic database used in SK90 (green line).

The line list that we use is a combination of the `XSTAR` atomic data set and the atomic data curated by Robert L. Kurucz. We take special care when merging these atomic data sets to not double count any lines. If a line was found in both data sets, we prioritize the `XSTAR` atomic data for X-ray lines and high energy UV lines and Kurucz’s data set otherwise. Information about the distribution of lines as a function of energy, oscillator strength, and ionization degree is shown in Fig. 2.2. This figure also includes information about the atomic data set used by SK90. Our current atomic data set contains over two million lines, covering a wider range of energies and ionization degrees and allowing for a more complete calculation of the force multiplier compared to previous studies, especially due to X-rays lines and lines from highly ionized plasma.

2.5 Force Multiplier Calculations

We adopt the same elemental abundances as Mehdipour et al. (2016) in both models. The ionization balance is determined by the external radiation field rather than by the LTE assumption (i.e. Saha ionization balance), using the photoionization code `XSTAR` to determine the ion abundances as a function of ξ . The gas temperature is also function of ξ , which entails an implicit assumption that the gas is optically thin. To guarantee this while also ensuring that collisional de-excitation processes are negligible compared to radiative processes in determining the ionization balance, we set the hydrogen nucleon number density in `XSTAR` to $n_H = 10^4 \text{ cm}^{-3}$. This value is in accordance with density estimates for AGN outflows (Arav et al., 2018). The column density was set to $N = 10^{17} \text{ cm}^{-2}$, the luminosity to $10^{46} \text{ ergs s}^{-1}$, and the ionization parameter at the inner radius to $\log(\xi) = 5$, placing the most ionized gas $\approx 1 \text{ pc}$ away from the source and least ionized gas $\approx 3000 \text{ pc}$ from the source. This results in the range ξ spanning $\log(\xi)$ from -2 to 5, where `XSTAR` defines ≈ 160 spatial zones with step sizes $\Delta \log(\xi) \approx 0.4$. In the two top panels of Fig. 2.3, we show the photoionization equilibrium temperature (i.e., the temperature for which the total amount of energy absorbed from the incident radiation field should balance the total emitted energy in lines and continua) as a function of ξ (black solid lines) and we shaded regions where the condition for isobaric thermal instability is satisfied (Field, 1965).

The force per unit mass due to an individual line can be computed as

$$f_L = \frac{F_\nu \Delta\nu_D}{c} \frac{\kappa_L}{\tau_L} (1 - e^{-\tau_L}), \quad (2.8)$$

where κ_L is the line's opacity, τ_L the line's optical depth, $\Delta\nu_D = \nu_0 v_{\text{th}}/c$ is the line's thermal Doppler width, with v_{th} being defined as the thermal speed of the ion that a given atomic line belongs to, and F_ν is the specific flux (Castor, 1974). The optical depth for specific line in a static

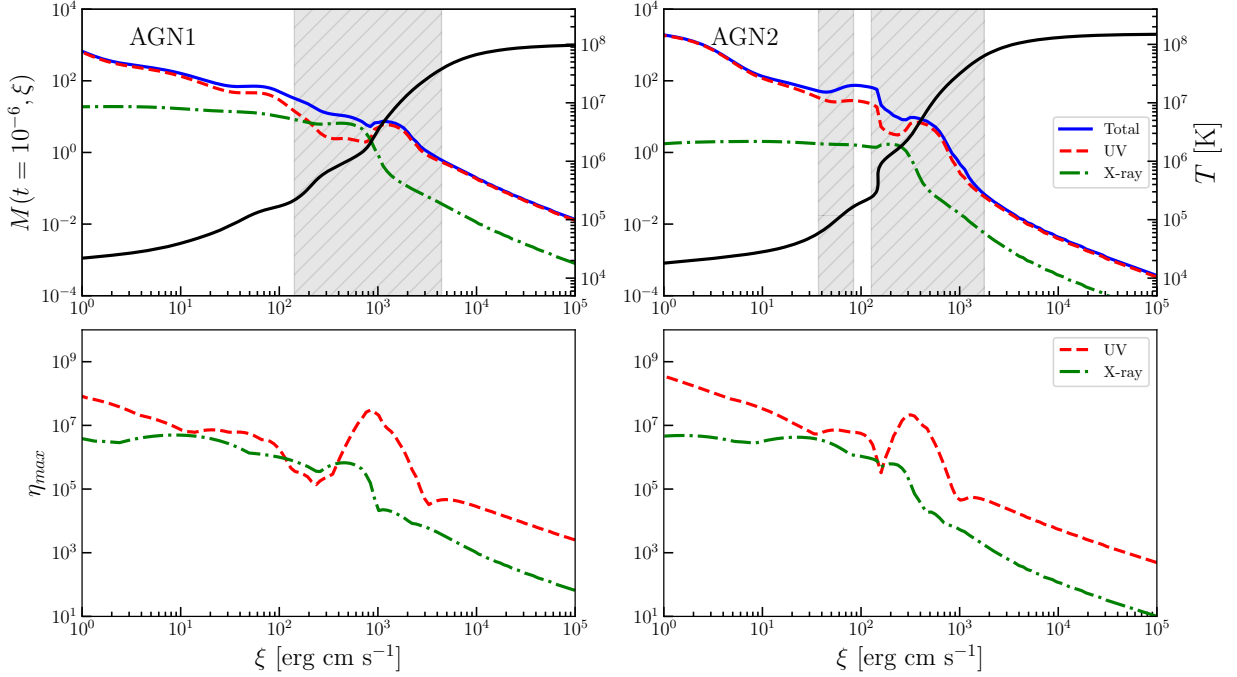


Figure 2.3. Summary of results from our photoionization and line force calculations. *Top panels:* The force multiplier $M(\xi, t)$ as a function of ξ for an optically thin gas with small optical depth parameter, $t = 10^{-6}$, for AGN1 (left) and AGN2 (right). This small value of t yields a proxy for M_{\max} . Plotted against the left vertical axes are values of M_{\max} due to all lines (solid blue curve), UV lines only (dashed red curve) and X-ray lines only (dash-dotted green curve). Plotted against the right vertical axes is the photoionization equilibrium temperature determined by XSTAR corresponding to $\mathcal{L} = 0$ (solid black line). The shaded regions indicate the parameter space where the gas is thermally unstable by the isobaric criterion (i.e., $[\partial \log T / \partial \log \xi]_{\mathcal{L}} \geq 1$; (e.g., Barai et al., 2012)). *Bottom panels:* The opacity of the single strongest UV and X-ray line as a function of ξ (dashed red and dash dotted green curves, respectively). The line opacity is in units of electron scattering opacity (see Eq. 2.14).

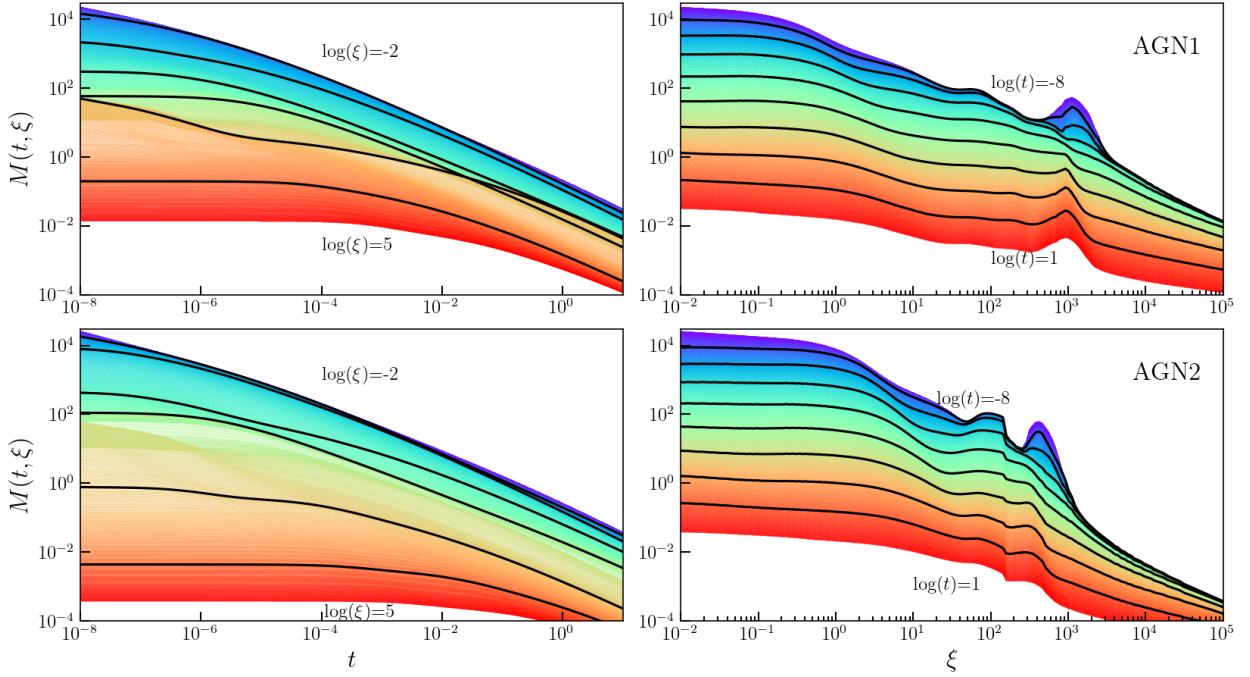


Figure 2.4. The main results from our photoionization and line force calculations. *Top panels:* These correspond to AGN1. The left panel shows our results as a function of t for a fixed ξ . The solid lines show results for a fixed ξ [from top to bottom, ξ increases from 10^{-2} (violet region) to 10^5 (red region)], and the ξ levels are separated by $\Delta \log(\xi) = 1$. The right panel shows results of our force multiplier calculations as function of ξ for a fixed t . The solid lines show results for a fixed t [from top to bottom, t increases from 10^{-8} (violet region) to 10 (red region)], and the t levels are separated by $\Delta \log(t) = 1$. *Bottom panels:* Same as the top panels for AGN2.

atmosphere is

$$\tau_L = \int_r^{\infty} \rho \kappa_L dr, \quad (2.9)$$

while in an expanding atmosphere it is

$$\tau_L = \rho \kappa_L l_{\text{Sob}}. \quad (2.10)$$

Here, $l_{\text{Sob}} \equiv v_{\text{th}}/|dv/dl|$ is the so-called Sobolev length. CAK defined a local optical depth parameter

$$t = \sigma_e \rho l_{\text{Sob}}. \quad (2.11)$$

We take v_{th} to be the proton thermal speed at 50,000 K. For a given line, we can define the opacity accounting for stimulated emission,

$$\kappa_L = \frac{\pi e^2}{m_e c} g f \frac{N_L/g_L - N_U/g_U}{\rho \Delta \nu_D}, \quad (2.12)$$

where κ_L is the opacity in units $\text{cm}^2 \text{g}^{-1}$ (where all other symbols have their conventional meaning). Following SK90, we assume a Boltzmann distribution (i.e. the Local Thermodynamic Equilibrium, LTE, assumption) when determining the level populations. For SK90's calculation, `XSTAR` version 1 did not explicitly calculate the populations of excited levels, and also such a calculation was not computationally feasible at the time. In our current work, the LTE assumption is made in order to allow the use of the Kurucz line list and to allow for direct comparison with CAK, SK90, Gayley (1995), and Puls et al. (2000). This line list is more extensive in the optical and ultraviolet than the lines currently considered by `XSTAR`. However, the Kurucz line list does not include the associated collision rates or level information which are needed in order to calculate non-LTE level populations. The LTE assumption results in a larger population of the excited levels when compared to a non-LTE calculation (see §2.7 for discussion on these points).

It is conventional to rewrite the optical depth as

$$\tau_L = \eta t, \quad (2.13)$$

where η is a rescaling of line opacity

$$\eta = \kappa_L / \sigma_e. \quad (2.14)$$

We can now write an expression for the total acceleration due to lines as

$$a_L = \frac{\sigma_e F}{c} M(t, \xi), \quad (2.15)$$

where $M(t, \xi)$ is the total force multiplier given by

$$M(t, \xi) = \sum_{\text{lines}} \frac{\Delta\nu_D F_\nu}{F} \frac{1}{t} (1 - e^{-\eta t}). \quad (2.16)$$

While t depends on the temperature through v_{th} , this temperature value is arbitrary and has no direct role in $M(\xi, t)$; our calculations of $M(\xi, t)$ just require one to be specified (i.e. the v_{th} terms cancel upon expanding the various components of Eq. 2.16; see Gayley 1995 for a detailed discussion of this point and an alternative formalism).

CAK found that $M(\xi, t)$ increases with decreasing t and it saturates as t approaches zero (i.e., gas becomes optically thin even for the most opaque lines). We will refer to the saturated value of $M(\xi, t)$ as M_{max} . CAK also showed that for OB stars, M_{max} can be as high as ~ 2000 (see also Gayley, 1995). This means that the gravity can be overcome by the radiation force even if the total luminosity, L , is much smaller than the Eddington luminosity, $L_{\text{Edd}} = 4\pi cGM/\sigma_e$. In other words, the radiation force can drive a wind when $L' M_{\text{max}} > 1$, where $L' \equiv L/L_{\text{Edd}}$ is the so-called Eddington factor.

The key result of SK90 was to show how $M(\xi, t)$ changes not only as a function of t but also as a function of ξ . In particular, they found that M_{max} increases gradually from ~ 2000 to 5000 as ξ increases from 1 to ~ 3 and then drops to ~ 0.1 at $\xi \sim 1000$. The line force becomes negligible for $\xi > 100$ because then $M_{\text{max}} \lesssim 1$.

The force multiplier depends also on other gas and radiation properties, for example gas metallicity (e.g., CAK) and column density, N_{H} (e.g., Stevens, 1991). However, here we concentrate

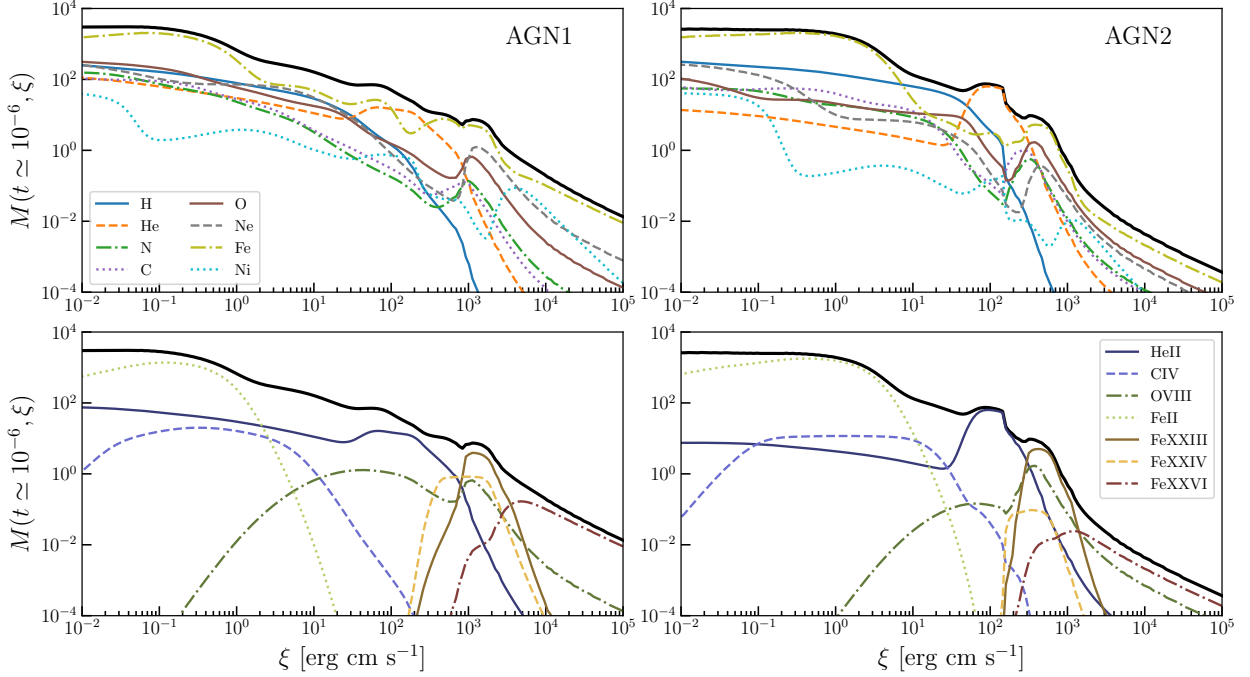


Figure 2.5. Main contributors to the total force multipliers. The left panels correspond to AGN1 and the right panels correspond to AGN2. The solid black line in each panel represents the total force multiplier for $t \simeq 10^{-6}$ (our proxy for M_{\max}). The top panels show the contribution to M_{\max} for various elements of interest (see the legend in the bottom left corner of the top left panel). Similarly, the bottom panels show the contribution of various ions (see the legend in the bottom right corner of the bottom left panel).

only on the effects due to t and ξ for a given SED and chemical abundance (the same as the ones in Mehdipour et al., 2016).

2.6 Results Using AGN SED

In Fig. 2.4, we show how the force multiplier changes as a function of ξ and t . The left hand side panels show that $M(\xi, t)$ is a mostly monotonic function of t that saturates at very small t for all ξ , while at large t , $M(\xi, t)$ is a power law of t as first found by CAK. The right hand side panels show that $M(\xi, t)$ decreases slightly with increasing ξ for small ξ and a fixed t . However, for $\xi \gtrsim 1$, $M(\xi, t)$ decreases significantly with increasing ξ (the details depend on t). The decrease is not monotonic; there is a resurgence in the line force for $\xi \approx 100 - 1000$ for both the AGN1 and

AGN1			AGN2		
$\log(\xi) \simeq 0$	$M_{total}(t, \xi) = 522$		$\log(\xi) \simeq 0$	$M_{total}(t, \xi) = 1635$	
Ion	Wavelength (Å)	$M_L(t, \xi)$	Ion	Wavelength (Å)	$M_L(t, \xi)$
H I	1216	5.051	H I	1216	5.992
H I	1026	4.768	H I	1026	5.769
C IV	1550	1.550	C IV	1550	1.840
N V	1239	1.355	C III	977	1.562
O VI	1037	1.224	N V	1239	1.520
$\log(\xi) \simeq 1$	$M_{total}(t, \xi) = 123$		$\log(\xi) \simeq 1$	$M_{total}(t, \xi) = 117$	
H I	1216	4.771	H I	1216	7.522
Ne VI	401	1.02	H I	1026	4.023
O VI	150	0.945	C IV	1548	2.227
O VII	21	0.724	N V	1239	1.907
C V	40	0.6812	O VI	1038	1.849
$\log(\xi) \simeq 2$	$M_{total}(t, \xi) = 24$		$\log(\xi) \simeq 2$	$M_{total}(t, \xi) = 9.2$	
O VIII	19	0.604	H I	6563	0.409
Si X	303	0.399	O VI	1032	0.171
Fe XI	180	0.340	Fe XI	180	0.096
Fe XII	202	0.330	Fe X	174	0.089
Fe XIV	284	0.290	Fe XII	187	0.089
$\log(\xi) \simeq 3$	$M_{total}(t, \xi) = 20$		$\log(\xi) \simeq 2.6$	$M_{total}(t, \xi) = 22$	
Fe XXIII	777	7.328	Fe XXIII	1157	6.200
Fe XXII	1157	3.546	Fe XXIII	1345	4.725
Fe XXII	1344	2.640	Fe XXIII	3739	3.909
Fe XXII	3738	2.172	Fe XXIII	9587	2.193
Fe XXII	9586	1.561	O VIII	1303	0.416

Table 2.1. Table showing the top five contributing lines to the force multiplier for AGN1 (left column) and AGN2 (right column) for fixed $t = 10^{-6}$ and selected values of ξ . Note that the value of ξ in the bottom section of the table differs in the each column; it is intended to correspond to the bump in the M_{\max} distribution at large ξ (see the black lines in fig. 2.5).

AGN2 cases. A similar “bump” feature on the plot of $M(\xi, t)$ vs. ξ was shown in SK90 (see Fig. 2 there). No such feature was shown in the work of Everett (2005), Chartas et al. (2009), and Saez and Chartas (2011); their models indicate that there should be a dramatic decrease of $M(\xi, t)$ in that region. Our calculations are nevertheless in agreement with the finding made by these recent studies showing that $M(t, \xi)$ can be larger than 1000 for low values of ξ .

The force multiplier is a sum of opacities due to various lines. To better understand its properties, in Fig. 2.5 we show the contributions to the force multiplier from various ions as a function of

ξ for $t = 10^{-6}$. We note that $M(t = 10^{-6}, \xi)$ is our proxy for M_{\max} , so this figure illustrates how M_{\max} changes with ξ . Similar to SK90, we find that Fe and He are the dominant contributors to the force multiplier. Table 2.1 lists the top five contributors to the force multiplier for four values of ξ . The top contributors for low values of ξ contribute $< 5\%$ to the total force multiplier, agreeing with previous findings (e.g. Abbott 1982, Gayley 1995, & Puls et al. 2000). Comparing to Fig. 2.5, we notice that although He contributes a substantial amount to $M(\xi, t)$ at $\xi \simeq 100$, it is absent from our table. Thus, this table illustrates an important result: the force multiplier is due to the contributions of many weak lines rather than a few very strong lines.

Returning to Fig. 2.3, we demonstrate how $M(\xi, t)$ depends on the energy of the photons. We present the UV and X-ray contributions to the force multiplier (top panels). The UV band contributes the majority of the line force with the X-ray energy band only being important for a narrow window in AGN1 (i.e., for ξ between 200 and 1000). We find a similar trend for the maximum opacity of a single line (bottom panels). We note that even though opaque IR lines are present in our line list, we omit them from these two panels, because there are comparatively few IR photons (see Fig. 2.1) compared to UV and X-ray. The line opacity is weighted by the continuum flux, hence IR lines contribute very little to the total force multiplier.

We finish this section with a couple of observations based on a comparison of the results from the force multiplier calculations and the heating and cooling calculations that we carried out using the same code and input parameters. First, the significant increases of the equilibrium temperature with ξ (see the solid black lines in the top panels of Fig. 2.3) occurs for the ionization parameter range where M_{\max} (solid blue lines) strongly decreases with increasing ξ . This is expected because spectral lines are major contributors to the gas cooling at small and intermediate ξ . Therefore, the decrease in the overall number of line transitions with increasing ξ manifests itself in a decrease in $M(\xi, t)$ as well as an increase in the gas equilibrium temperature (i.e., an increase in the slope

of the $\log T$ vs $\log \xi$ relation).

Second, the shaded regions in Fig. 2.3 mark the ξ values for which the gas is thermally unstable (where the slope of the equilibrium curves exceed one). These regions closely coincide with those corresponding to the resurgence in the line force. As we will discuss in the next section, this overlap may strongly impact the significance of line driving for high ionization parameters where $M(\xi, t)$ is nominally still larger than one.

2.7 Discussion of Force Multiplier Calculations

The basic requirement for line driving to win over gravity is $M_{\max}L' > 1$. The non-monotonic behavior of M_{\max} vs. ξ implies that line-driving can be dynamically important over a relatively wide range of ξ , wider than explored in previous line-driven wind simulations, for example, those by Proga et al. (2000), Proga and Kallman (2004), Proga (2007), Kurosawa and Proga (2008), Kurosawa and Proga (2009b), Kurosawa and Proga (2009a) and Dyda and Proga (2018). The line force might have been underestimated in those calculations. We say this with caution, since the above requirement is just a necessary and not a sufficient condition for producing an appreciable line-driven wind.

Our finding that the gas can be thermally unstable over the same range of ξ where there is a bump in the M_{\max} distribution implies that this potential increase of the line force might not be physically realized. This can be either because the flow avoids the thermally unstable region altogether (as in the 1D models of D17), or because cloud formation is triggered, thereby changing the local ionization state of the gas. In either case, only a relatively small amount of gas (e.g., as measured by the column density) may be subject to the strong force at the location of the bump. The effects of thermal instability in dynamical flows (Balbus 1986; Mościbrodzka and Proga 2013) must be further understood before a definitive conclusion can be drawn. If cloud formation

naturally occurs, the clouds will subsequently be accelerated (see Proga & Waters 2015) and the resulting multiphase flow may have right properties (e.g., velocities and ionization structure) to account for the narrow line regions in AGN.

The bump at $\xi \approx 100 - 1000$ may also have interesting implications for the dynamics of line driven winds. That is, a bump should be accompanied by different stages of acceleration, with distinct lines accompanying each stage, for Eddington fractions as low as 0.01. Note, however, that if the overall decrease in the number of lines, including coolants, leads to significant heating (i.e., runaway heating and thermal instability), the flow might be thermally driven rather than line-driven. Also not addressed are the effects of continuum opacity, which can contribute significantly to the total radiation force (e.g., Stevens, 1991; Everett, 2005; Saez and Chartas, 2011).

CHAPTER 3: HEATING AND COOLING PHOTOIONIZED GAS AND TI

Here, we present the global simulations of an outflow that is multiphase due to TI. Specifically, we show that there exists a range of the so-called hydrodynamic escape parameter (HEP), small yet relevant, for which the outflow can develop regions with significant over- and under-densities and that the over-densities can survive their acceleration over a relatively large distance. We identify the physical effects that contribute to making the HEP range small and thus explain why we and others have not yet seen a clumpy outflow in any previously published results from the simulations of thermally driven outflows, neither in 1- nor 2-D simulations (e.g., Woods et al., 1996; Proga and Kallman, 2002; Luketic et al., 2010; Higginbottom and Proga, 2015; Dyda et al., 2017; Waters and Proga, 2018).

3.1 Basic Equations of Hydrodynamics

In this section, we briefly discuss the basic equations of hydrodynamics that govern the dynamics of gas in AGN. Although it should be noted that more complicated equations, such as those of multi-group radiation magnetohydrodynamics coupled with the non-LTE statistical rate equations, are required to obtain a complete model of the AGN environment.

Gas in AGN is observed to be partially ionized, which means that it contains both free electrons and ions. Magnetic fields can arise locally via a dynamo process or travel inward from plasma originating in the interstellar medium of the galaxy. In the presence of magnetic fields, electrons cannot flow freely across magnetic field lines, meaning that the equations of magnetohydrodynamics with anisotropic conduction must be solved in order to fully capture this behavior.

AGN are definitionally ample suppliers of continuum radiation, sometimes allowing the forces due to radiation can be dominant over all others. If the gas responsible for the observed line takes the form optically thick clumps, then the dynamics of these clumps must be governed by the equations

of radiation hydrodynamics To solve this set equations would require calculating the opacity of gas which requires a detailed understanding of gas composition, ionization balance, state occupancy. These opacities are incredibly sensitive to frequency, so a multi-group approach would be required for a full accounting of how the gas and spectral energy distribution interact.

We have two ways to describe the motions of fluids: the Lagrangian and Eulerian points of view. The Lagrangian point of view description follows a particular fluid particle as it moves through space and time, often used when the motion of individual fluid particles is more important than the overall structure of the flow. The Eulerian description, on the other hand, describes the fluid motion at a fixed point in space and is often used when the motion of the fluid as a whole is important, such as in planetary atmospheres or stellar winds. While both methods are employed to solve computation fluid mechanics problems, we'll focus our understanding to the Eulerian point of view with our source terms added to account for heating and cooling and radiation force as they are present in our simulations using ATHENA++ Stone et al. (2020). Those equations are:

1. Conservation of Matter

$$\frac{\partial \rho}{\partial t} + \nabla \cdot (\rho \mathbf{v}) = 0 \quad (3.1)$$

2. Conservation of Momentum

$$\frac{\partial \rho \mathbf{v}}{\partial t} + \nabla \cdot (\rho \mathbf{v} \mathbf{v} + \mathbf{P}) = -\rho \nabla \Phi + \mathbf{F}_{\text{rad}} \quad (3.2)$$

3. Conservation of Energy

$$\frac{\partial E}{\partial t} + \nabla \cdot [(E + P) \mathbf{v}] = -\rho \mathbf{v} \cdot \nabla \Phi - \rho \mathcal{L} + \mathbf{v} \cdot \mathbf{F}_{\text{rad}} \quad (3.3)$$

Where ρ is the fluid density, \mathbf{v} is the fluid velocity, $\mathbf{P} = p \mathbf{I}$ with p the gas pressure and \mathbf{I} the unit tensor, $\Phi = -GM_{\text{BH}}/r$ is the gravitational potential due to a black hole with mass M_{BH} , $E = \rho \mathcal{E} + 1/2 \rho |\mathbf{v}|^2$ is the total energy with $\mathcal{E} = (\gamma - 1)^{-1} p / \rho$ the gas internal energy, $\mathbf{F}^{\text{rad}} = F^{\text{rad}} \hat{\mathbf{r}}$

is the radiation force, and \mathcal{L} is the net cooling rate. All of our calculations assume $\gamma = 5/3$ when heating and cooling are present, but use $\gamma = 1.00001$ when we assume an isothermal equation of state. We compute models both with and without radiative line driving and let $F_{\text{rad}} = (1 + M(t, \xi)GM_{\text{BH}}\rho\Gamma/r^2)$, where $\Gamma = L/L_{\text{Edd}}$ is the Eddington fraction and $M(t, \xi)$ is the radiative force multiplier (discussed more in § 2.5). Irradiation is thus assumed to be due to a point source, as is appropriate when considering parsec scales in relation to the X-ray coronae and the UV emitting regions of AGN disks.

3.1.1 Thermal Instability (TI)

Thermal instability (TI, Field, 1965) was long ago recognized as a viable mechanism for producing multiple phases in AGN winds (e.g. Davidson and Netzer, 1979; Krolik and Vrtilik, 1984; Shlosman et al., 1985). Such winds are observed, for example, in some Seyfert galaxies, where the UV and X-ray absorbers have similar velocities, strongly suggesting that very different ions are nearly cospatial and therefore that different temperature regions coexist (e.g., Shields and Hamann, 1997; Crenshaw et al., 2003; Gabel et al., 2003; Longinotti et al., 2013; Fu et al., 2017; Mehdipour et al., 2017, and references therein).

While TI is well understood in a local approximation (e.g., Balbus, 1995; Waters and Proga, 2019), it has proven challenging to quantitatively model clump formation in a dynamic flow. Only in recent years has it become clear how the in situ production of multiphase gas can be triggered using *global* time-dependent hydrodynamical simulations – and only in the context of accretion flows (Barai et al., 2012; Gaspari et al., 2013; Takeuchi et al., 2013; Mościbrodzka and Proga, 2013, MP13 hereafter) or stratified atmospheres (e.g., McCourt et al., 2012; Sharma et al., 2012). In an outflow regime, previous work has focused on highlighting the importance of considering the effects of clumpiness, but only on a qualitative basis (e.g., Nayakshin, 2014; Elvis, 2017).

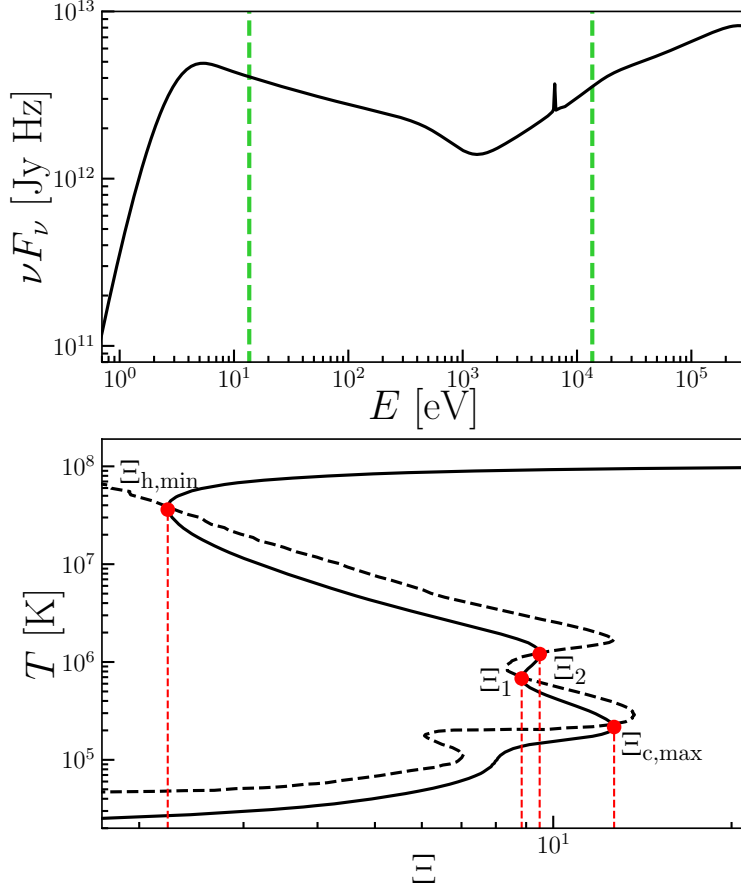


Figure 3.1. *Top panel:* SED intrinsic to NGC 5548, as determined by Mehdipour et al. (2015). The energy range used to define ξ is marked by the two vertical lines. This SED is relatively flat and has $L_X/L \approx 0.36$ and mean photon energy $\langle h\nu \rangle = k_B T_X = 34.8$ keV (corresponding to Compton temperature $T_C = T_X/4 = 1.01 \times 10^8$ K). *Bottom panel:* Associated S-curve and Balbus contour (the solid and dashed lines, respectively). Red dots mark the points $\Xi_{c,\max}$, Ξ_1 , Ξ_2 , and $\Xi_{h,\min}$. Note that $\Xi_{c,\max}$ ($\Xi_{h,\min}$) denotes the last (first) stable point on the “cold phase branch” (“Compton branch”) of the S-curve. The SED-dependent conversion to the other common ionization parameter $U = (\Phi_H/c)/n$ (with Φ_H the number density of H I ionizing photons) is $U \approx \xi/42$, so $[\log(\Xi_{c,\max}), \log(\xi_{c,\max}), \log(U_{c,\max})] = [1.10, 2.15, 0.53]$.

3.2 Numerical Considerations and Simulation Setup

As mentioned in § 3.1, we employ the magnetohydrodynamics code ATHENA++ Stone et al. (2020) to solve the equations of non-adiabatic gas dynamics.

For the unobscured AGN SED of NGC 5548 from Mehdipour et al. (2015), shown in the top panel of Fig. 3.1, D17 have tabulated the net cooling rate $\mathcal{L} = \mathcal{L}(T, \xi)$, which is function of the gas temperature, T , and the ionization parameter, ξ (Eq. 2.1). The ξ dependence on distance

plays an important role in determining the thermal stability of the flow, as discussed in detail in §3.4. Also, the ratio between the hard and soft X-ray energy bands is an important characteristic affecting properties of TI (e.g., Kallman and McCray, 1982; Krolik, 1999; Mehdipour et al., 2015; Dyda et al., 2017).

The solid line in the bottom panel of Fig. 3.1 is the S-curve corresponding to this SED, i.e. the contour where $\mathcal{L}(T, \Xi) = 0$, where $\Xi \equiv p_{\text{rad}}/p = \xi/(4\pi ck_{\text{B}}T)$ is the pressure ionization parameter, with p_{rad} the radiation pressure (equal to F_{X}/c in our models). For the adopted SED, gas is unstable by the isobaric criterion for local TI in the two zones where the slope of the S-curve is negative (these are the locations where Field’s criterion for TI, $[\partial\mathcal{L}/\partial T]_p < 0$, is satisfied). Gas is actually thermally unstable everywhere left of the dashed line (hereafter referred to as the Balbus contour), as this region of parameter space satisfies Balbus’ generalized criterion for TI, $[\partial(\mathcal{L}/T)/\partial T]_p < 0$ (Balbus, 1986). Points corresponding to the maximum value of Ξ on the cold stable branch of the S-curve (i.e, for $\log \Xi_{\text{c,max}} = 1.10$) are dynamically the most significant, as they mark the entry into a cloud formation zone and dramatic changes in the flow profiles can occur there.

We present the results of 1-D models run at both medium and high resolution, all using a uniform grid spacing $[\Delta r \approx (r_{\text{out}} - r_0)/N_r]$. The standard resolution runs (Models A-1x, B-1x, C-1x, & D-1x) have $N_r = 552$, chosen such that gradient scale heights $\lambda_q \equiv q/|dq/dr|$ (where q is any hydrodynamic variable) are adequately resolved with $\lambda_q/\Delta r \approx 3$ for $r \lesssim 1.1 r_0$ and $\lambda_q/\Delta r > 10$ at all other points in the wind except in the vicinity of the location where $\Xi = \Xi_{\text{c,max}}$, where this ratio dips to about 1. The high resolution runs (Models A-8x, B-8x, C-8x, & D-8x) have $N_r = 8 \times 552$, nearly an order of magnitude higher resolution everywhere. The other relevant length scale to resolve is that of the clumps, which have a size on the order of the local cooling length scale $\lambda_{\text{cool}} \equiv c_s t_{\text{cool}}$, where $t_{\text{cool}} = \mathcal{E}(n\mathcal{C}/m_p)^{-1}$ is the cooling time while \mathcal{C} is the cooling

Model	HEP	r_0	ρ_0	$t_{\text{sc},0}$	$t_{\text{cool}}/t_{\text{sc}}$	$\langle v \rangle$	$\langle \dot{M} \rangle$	Comment	
		[10^{18} cm]	[10^{-18} g cm $^{-3}$]	[10^{12} s]		[10^7 cm s $^{-1}$]	[10^{24} g s $^{-1}$]	1x runs	(8x runs)
A	13.3	1.01	2.68	3.4	0.47 (0.48)	6.4 (6.0)	1.2 (1.2)	steady	(steady)
B	11.9	1.13	2.15	3.9	0.54 (0.49)	3.4 (3.5)	3.2 (3.3)	unsteady	(unsteady)
C	9.1	1.48	1.26	5.0	0.41 (0.42)	2.5 (2.3)	5.9 (6.0)	unsteady	(unsteady)
D	8.1	1.67	0.98	5.7	0.41 (0.41)	2.4 (2.2)	6.6 (6.7)	quasi-steady	(unsteady)

Table 3.1. Summary of key parameters and results. HEP is the hydrodynamic escape parameter. The inner radius is derived from the choice of HEP as $r_0 = (1 - \Gamma) GM_{\text{BH}} \text{HEP}^{-1} c_{s,0}^{-2}$ (see Eq. 3.5), while the density at the base follows from the definition of ξ as $\rho_0 = \mu m_p L_X \xi_0^{-1} r_0^{-2}$. The sound crossing time is defined as $t_{\text{sc},0} = (r_{\text{out}} - r_0)/c_{s,0}$. The ratio $t_{\text{cool}}/t_{\text{sc}}$ is given at the location where $\Xi = \Xi_{c,\text{max}}$. The average mass flux and velocity through r_{out} are shown as $\langle \dot{M} \rangle$ and $\langle v \rangle$. Comment columns denote the state of the flow at late times. Values/comments in parenthesis denote results for the 8x-resolution runs.

rate in units of $\text{erg cm}^3 \text{s}^{-1}$. For $\gamma = 5/3$,

$$\lambda_{\text{cool}} \approx 3 \times 10^{16} T_5^{3/2} n_3^{-1} C_{23}^{-1} \text{ cm}, \quad (3.4)$$

where $T_5 = T/10^5 \text{ K}$, $n_3 = n/10^3 \text{ cm}^{-3}$, $C_{23} = C/10^{-23} \text{ erg cm}^3 \text{s}^{-1}$, and $T_5 = n_3 = C_{23} = 1$ are characteristic values of the clumps. With $\Delta r \approx 2 \times 10^{15} \text{ cm}$ for our ‘-1x’ runs, this length scale is adequately resolved.

We apply outflowing boundary conditions at the inner and outer radii with the density fixed at the innermost active grid point to the value of ρ_0 in Table 3.1. The initial conditions are a simple expanding atmosphere with $\rho = \rho_0 (r/r_0)^{-2}$ and a β -law velocity profile, $v = v_{\text{esc}} \sqrt{1 - r_0/r}$, where the ‘0’ subscript is used to denote values at the inner radius of the computational domain, r_0 . The pressure profile is set according to the temperature, chosen so that the gas lies along the S-curve, having a value Ξ_0 at r_0 (see §2.6).

The 2-D model uses a 256×256 grid in r and θ , with logarithmic spacing in r such that $dr_{i+1} = 1.01 dr_i$ and uniform spacing in θ from 0 to π . At the inner boundary we assumed a density profile $\rho = \rho_0 [1 + 0.001 \sin(2\theta)]$ to break spherical symmetry. We apply reflecting boundary conditions at 0 and π .

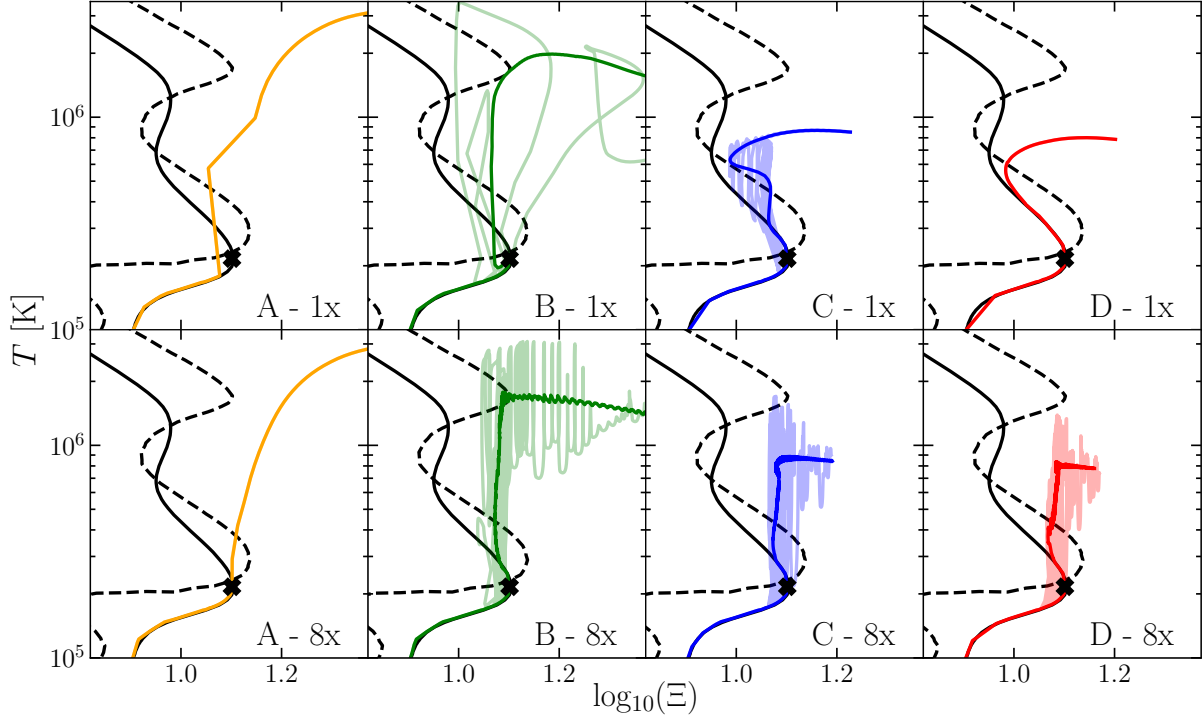


Figure 3.2. Phase diagram comparison of our four 1-D models showing T as function of Ξ in relation to the thermal equilibrium curve (black solid line) and the Balbus contour (black dashed line). The colored solid lines display time-averaged solutions and the less opaque lines a single snapshot at the end of the simulation (at $t > 3t_{\text{sc},0}$). The top row presents our standard resolution (‘-1x’) runs and the bottom row our high (‘-8x’) resolution runs. See §2.6 and §3.4 for details about the dynamics of each model.

3.3 Results

For a given M_{BH} , just three parameters govern our solutions: Γ , Ξ_0 , and the HEP, which sets the strength of thermal driving. We define HEP as the ratio of effective gravitational potential and thermal energy at r_0 ,

$$\text{HEP} = \frac{GM_{\text{BH}}(1 - \Gamma)}{r_0 c_{s,0}^2}. \quad (3.5)$$

We only present models with $\Xi_0 = 3$, $\Gamma = 0.3$, and $M_{\text{BH}} = 10^6 M_{\odot}$, as HEP is the main governing parameter. We note, however, that the choice of Ξ_0 is not unimportant, e.g., selecting one too large can cause the flow to miss relevant regions. The dependence of stable wind solutions on Γ for various SEDs was explored in 1-D by D17. In Table 3.1, we list model parameters and summarize gross outflow properties.

After examining over one hundred 1-D simulations, with the standard resolution, that span this parameter space, we arrived at four qualitatively different 1-D wind solutions that capture the general behavior seen across all runs. These four cases illustrate how the stability of the outflow depends on the HEP (and the numerical resolution). We chose the values of HEP for our models A and D such that they closely bracket the parameter space leading to transonic, clumpy winds (here represented by models B, C, and D-8x).

For each model, Fig. 3.2 shows the models tracks on the phase diagram while Fig. 3.3 shows radial profiles of ρ , v , T , and Ξ . The phase diagrams reveal that all solutions pass through the lower TI zone but only models B and C with the standard resolution actually trigger TI to become unsteady. Additionally, two general trends are evident: (i) the range of Ξ decreases with HEP and (ii) for large Ξ , the wind is not in thermal equilibrium; the wind temperature is nowhere near that of the stable Compton branch on the S-curve (the maximum temperature shown in these plots is more than an order of magnitude lower than T_C). The first trend is due to the fact that for thermal winds, the velocity is a decreasing function of HEP, and by mass conservation for radial flows, $\xi \propto v$ in a steady state (i.e. $v \propto 1/nr^2$, as is ξ). Trend (ii) is due to adiabatic cooling (see D17), but note that the highest temperatures reached in all four cases occupy thermally stable regions of the (T - Ξ)-plane (namely, regions to the right of the Balbus contour). We now examine the dynamics of these solutions in detail to understand why Models B, C, & D-x8 are clumpy, while A & D-x1 are not.

3.3.1 Unsteady, Clumpy Wind Solutions

A basic requirement for TI to operate once gas enters the TI zone is for it to stay there long enough for initially small perturbations to grow. In terms of timescales, the flow must satisfy $t_{\text{cool}} < t_{\text{sc}}$ on global scales, which it does (see Table 3.1). However, Fig. 3.2 shows that for the flow to remain in the TI-zone, it must also be the case that Ξ *not* increase downstream, the normal

tendency in disk winds, at least in the absence of magnetic field pressure (Higginbottom and Proga, 2015). This normal Ξ -scaling is especially obvious in the 1-D radial winds studied by D17 that had constant radiation flux. In such winds, $\Xi \propto 1/p$, and p tends to decrease radially outward in outflows, the necessary condition for the pressure gradient to overcome gravity. The increase in Ξ will therefore cause the gas to quickly leave the TI zone (i.e. to cross to the right of the dashed lines in Fig. 3.2 once reaching $\Xi_{c,\max}$). What we see in models B, C, and D, however, is that Ξ can decrease outwards through the TI-zone (see the bottom panels in Fig. 3.3). Viewed in terms of the phase diagrams, gas not only enters and stays in the TI zone, but even crosses through a large portion of this zone. That a necessary condition for a clumpy wind solution is for the gas pressure profile to be such that it leads to a decrease of Ξ within a TI zone is the critical insight of this work. The criterion that Ξ decrease outward is hard to satisfy (see §3.4), explaining why TI is absent in the thermally driven wind models studied in the past.

In model B, the inner gas is just slightly less gravitationally bound than in model A (HEP of 11.9 compared to 13.3), yet this is enough for the flow to be twice as fast at small radii and to follow the S-curve all the way to the TI zone. As the flow enters this zone, we see formation of an initially thin layer where the temperature increases rapidly (see the locations marked by dotted lines in Fig. 3.3). This heating is radiative and is related to the gas being thermally unstable. We note that the heating is localized, namely, the gas immediately interior and exterior of this hot layer is relatively cool and dense, as it is gas located on or just above the upper branch of the cold phase. The separation of this cooler downstream flow that has entered the TI zone from the cold phase upstream flow by the hot layer is the origin of a dense clump that, in the animations of these runs (see Fig. 3.3 for a link), appears as an ejection of a layer of cold gas.

We reiterate that this is not clump formation from a condensation as in classical TI, as the role of TI here is primarily to form a hot layer. This layer is initially cool, lying above a stable

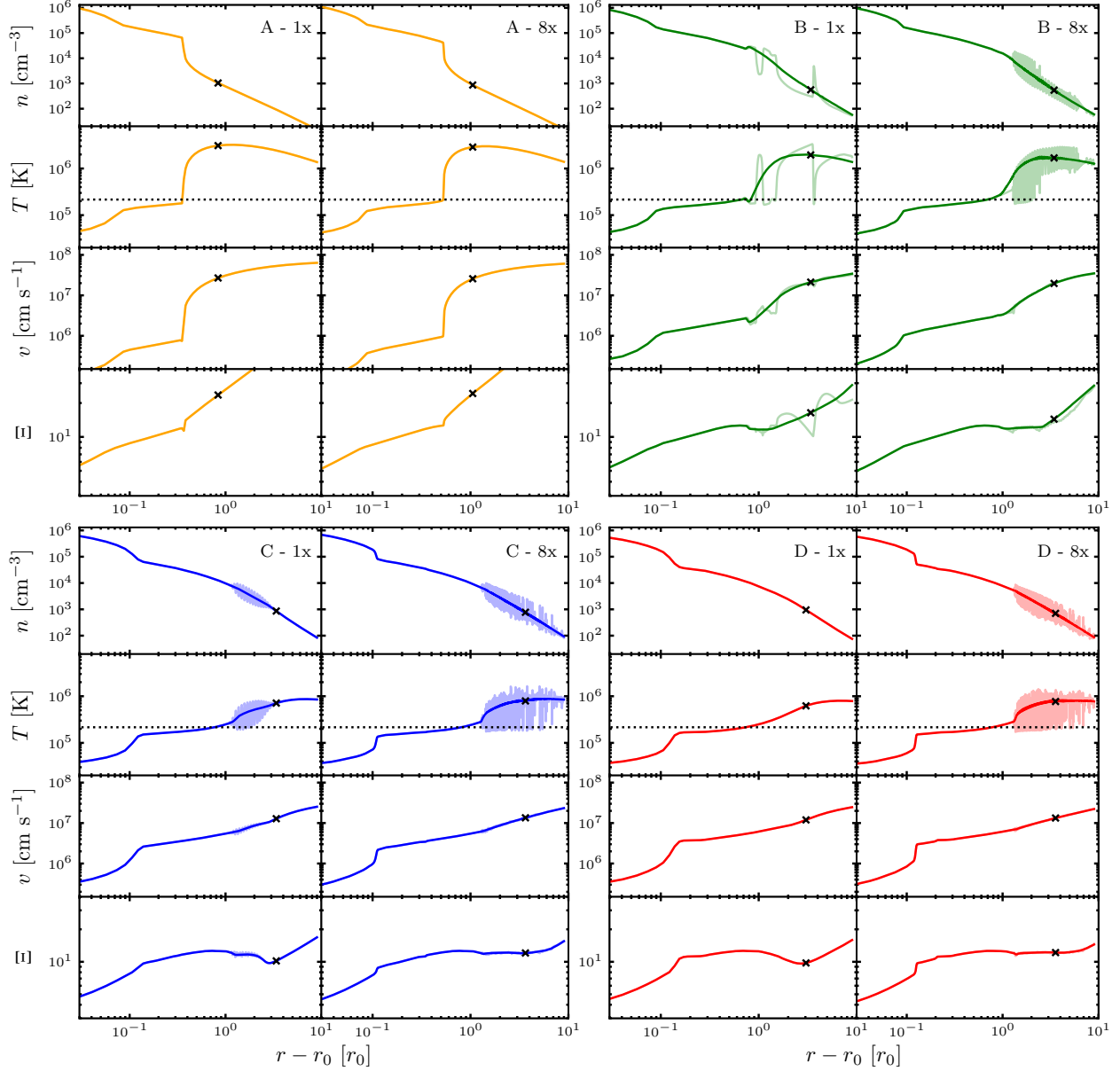


Figure 3.3. Spatial low profiles of our four 1-D models run at both medium (‘-1x’ runs, the first and third columns of panels) and high (‘-8x’ runs, the second and fourth column of panels) resolution. As in Fig. 2, fully opaque curves show time-averaged profiles, while less opaque ones are snapshots from the end of the simulation. The X’s mark sonic points of the time-averaged solutions. In the temperature panels, the dotted black line shows where $T = T(\Xi_{c,\max})$. Animations of these runs are downloadable at <https://doi.org/10.5281/zenodo.3739603> or watchable at <http://www.physics.unlv.edu/astro/clumpywindsims.html>.

cold region and below an unstable and condensing cool region, but there is very little ‘room’ in the $(T-\Xi)$ -plane for gas to condense, while there is a lot of room for it to heat. With time, the hot layer expands and pushes the colder, dense material outward. The ram pressure increases somewhat the

density of the cold gas but it is not the cause of the over-densities. It would be more appropriate to view this process as the separation of layers of the atmosphere rather than the condensation of cool clumps.

We note that TI operates here under nearly isobaric conditions (the cold and hot phases in Fig. 3.2 are connected by nearly vertical lines at a given radius). In particular, the size of the perturbation that grows, as well as the resulting clumps, are both smaller than the pressure scale height, and therefore they have nearly constant pressure. Despite having $t_{\text{cool}} < t_{\text{sc}}$ globally (i.e. on the scale of λ_p) as mentioned above, the requirement for isobaricity ($t_{\text{sc}} < t_{\text{cool}}$) is satisfied locally.

Finally, while it is not obvious from Figs. 3.2 and 3.3, we found that generally as the flow accelerates, ξ increases, even for the cold phase gas. This leads to heating and expansion of the colder clumps, eventually causing them to enter the hot phase. In model C-1x, this expansion process operates over a relatively small radial range and is well displayed in the figures as a decrease in the density and temperature variations with distance.

3.3.2 Smooth Wind Solutions Passing Through a TI Zone

Models with HEP higher than that for model B evolve toward a steady, transonic and stable solution of a Compton heated wind, while all other models are *unstable* (and hence unsteady) transonic solutions of a thermally driven wind heated mainly by photo-absorption (the temperature at the sonic point and even of the hottest gas is less than 10^6 K). Model A resembles the cases that we saw in the past (e.g., D17). At small radii, the gas is subsonic with a density profile close to that of a hydrostatic equilibrium solution for a temperature profile tracing the cold branch of the S-curve. At $r \approx 1.4 r_0$, where $\log \Xi \simeq 1.1$, the flow undergoes runaway heating (see the temperature panels in Fig. 3.3 for Model B). The heat input is relatively large and it results in a rapid flow acceleration, the wind becoming supersonic at $r \approx 2 r_0$. Similarly to the cases described in D17, the increase in v is so significant that the adiabatic cooling becomes faster than the radiative heating

and the flow does not evolve along the S-curve at large radii.

Two dynamical effects suppress TI in solutions with relatively high HEP: 1) stretching (i.e. radial flow acceleration that causes rapid expansion of fluid elements) operating on the time scale $\tau_s = 1/|\partial v/\partial r|$ and 2) high velocity. The latter causes a gas parcel to ‘fly through’ the TI zone on the dynamical time scale $\tau_d = |r/v|$, which is shorter than the maximum growth rate of TI, τ_{TI} . These two effects are the main reason for an accelerating flow to be thermally stable despite satisfying Balbus’ generalized instability criterion (see discussions of this point in MP13 and Higginbottom and Proga (2015) in the context of accretion flows and of thermal disk winds, respectively).

Model D-x1 seems similar to model A-x1, insomuch as it appears to reach a steady state, but model D-x1 hosts fluctuations at the level of $\lesssim 10\%$. This model is also a clear example of a solution that follows the S-curve backwards in the $(T-\Xi)$ -plane (see the upper right panel of Fig. 3.2); it occupies the same region of the phase diagram as models B and C without becoming noticeably unsteady. Our analysis of the time scales shows that although τ_{TI} is small compared to τ_s , the perturbations that are triggered by grid scale noise do not stay in the TI zone long enough to grow beyond the 10% level in model D-x1. However, model D type solutions are unstable at both higher resolution and to linear perturbations inserted by hand, in contrast to model A type solutions. Indeed, we checked that adding random perturbations with $10^{-3} \lesssim \delta\rho/\rho_0 \lesssim 10^{-1}$ at r_0 cause model D-x1 to behave similarly to model C-x1.

3.3.3 Clumpy Winds in 2-D

We conclude the presentation of our results with one example of a 2-D simulation, the counterpart to model B. The bottom panels in Fig. 3.4 shows the temperature and density in cgs units, whereas the top panels show the relative difference between these quantities and their time-averaged values ($\langle T \rangle$ and $\langle \rho \rangle$) at a given location for a snapshot near the end of the simulation. Notice that the flow is very clumpy at $r \simeq 2 r_0$ but appears quite smooth at larger radii where the density is

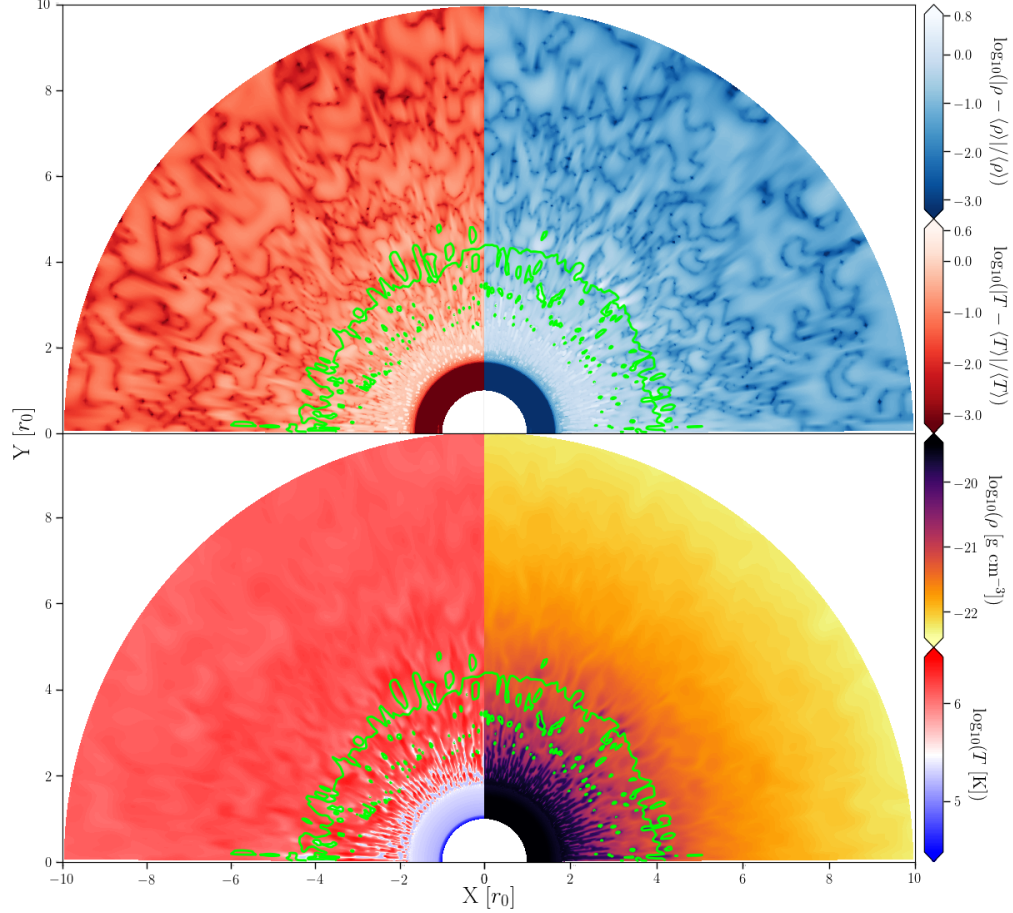


Figure 3.4. 2-D version of model B. *Bottom Panels:* Log-scale maps of T (left) and ρ (right) in cgs units. *Top Panels:* The relative difference of T (left) and ρ (right) computed using time averaged values. Bright green contours display sonic surfaces.

overall smaller and clumps have begun to expand. This is apparent from the density profiles in our 1-D simulations, although not altogether obvious. The maximum density/temperature contrast is never more than 10.

Compared to model B in 1-D, we found a significant scatter of the 2-D wind profiles at a given radius, which reflects the loss of spherical symmetry. The amplitude of the scatter (i.e., the variability in the θ direction) is of the same order as the variation in the radial direction. This in turn shows that the perturbations grow to a similar level in both directions.

3.4 Discussion of Thermally Driven Winds and Their Clumpiness

In this study, we identified a finite parameter space for which a thermally driven wind is clumpy. The origin of the clumps in our X-ray irradiated outflows is very similar to that of clumpy accretion flows studied by Barai et al. (2012) and MP13: quite simply, small perturbations are allowed to grow due to TI. However, we found that because the flow enters the TI zone near the cold phase, TI mainly serves to raise the temperature of perturbations. Therefore, the clumpiness is a result of the separation of heated layers of gas from the cold, dense layers near the base of the flow rather than the formation of dense clumps within a more tenuous background plasma. Importantly, this formation of heated layers from TI requires that a perturbation can stay in the TI zone long enough for it to become nonlinear and that stretching due to radial flow acceleration does not stabilize the growth of such layers.

These two requirements represent necessary conditions for TI to operate in dynamical flows and are due to velocity gradients in the wind that are not accounted for in the classical theory of TI. We similarly identified another necessary condition that distinguishes dynamical TI from local TI, this one arising from pressure gradients: Ξ must decrease once gas enters a TI zone (see §3.3.1). Because Ξ is the ratio of two pressures, both of which are decreasing functions of radius, Ξ could be a non-monotonic function of radius. Specifically, the models here have $\Xi \propto 1/(r^2 p)$, and even though p decreases with radius, this decrease could be slower than $1/r^2$ and Ξ can decrease downstream.

To build intuition for when to expect a clumpy versus smooth outflow, we could just consider the geometric effects involved in the problem. For example, let us assume that the radiation flux scales as r^{-q} , where q is a constant. We then find the following trend: the more q is less than 2, the more solutions resemble those from D17, where the wind is steady and monotonic and Ξ shows no ‘back tracking’. For $2.0 \lesssim q \lesssim 2.5$, the wind is unsteady and the range of Ξ and T is reduced

compared to the cases presented here. For $q \gtrsim 2.5$, the flux drops so fast that the heating is very weak. Consequently, Ξ and T are never large enough for the solution to even approach the TI region and as a result the flow is smooth.

CHAPTER 4: THERMALLY AND LINE DRIVEN WINDS

In many astrophysical systems both the momentum and energy of photons could be dynamically important in launching and accelerating mass outflows. A proper inclusion of the radiation heating/cooling and radiation forces in outflow models is challenging as it requires accurate treatment of a non-trivial coupling between electromagnetic radiation and matter (i.e., the gas opacity and emissivity) from the underlying spectral energy distribution (SED) of the radiation. In a series of papers, we described our framework for self-consistent modeling of outflows from a variety of objects (e.g., stars, accretion disks around stars as well as black holes). We build our framework upon several previous studies of gas outflows in cataclysmic variables (CVs) and AGN where radiation source terms are included in a progressively more self-consistent manner (e.g., Proga et al., 1998, 2000; Proga, 2007; Proga and Waters, 2015).

In Dyda et al. (2017; hereafter D17), we presented our general method for modeling of the outflows that results from the irradiation of optically thin gas by a radiation field with an *arbitrary* strength and SED. We used the photoionization code XSTAR (Kallman and Bautista, 2001) to calculate the radiative heating and cooling rates (\mathcal{H} and \mathcal{C} , respectively) as functions of gas temperature, T , and gas ionization parameter, ξ (Eq. 2.1). We explored several SEDs: those due to unobscured and obscured AGN (AGN1 and AGN2, hereafter Mehdipour et al., 2015), as well as SEDs for hard and soft state X-ray binaries (XRB1 and XRB2, hereafter; Trigo et al. (2013), see fig. 1 in D17), bremsstrahlung, and blackbody (BB). This general method was applied to study the hydrodynamics of 1-D spherical winds heated by a uniform radiation field using the magnetohydrodynamic (MHD) code ATHENA++ (Stone et al., 2020).

In our following-up work Dannen et al. (2019; hereafter D19), we made the next step in our development of a self-consistent comprehensive model of astrophysical winds. As in D17, we employed the photoionization code XSTAR, this time to compute not only $\mathcal{H}(\xi, T)$ and $\mathcal{C}(\xi, T)$ but

also the radiation force due to spectral lines using the most complete and up-to-date line list. For a radial flow, the line force $\mathbf{F}_{\text{rad},l}$, equals to $\mathbf{F}_{\text{rad},e}M$, where $\mathbf{F}_{\text{rad},e}$ is the radiation force due to electron scattering and M is the famous force multiplier (Castor et al., 1975, CAK hereafter). For a given SED, the force multiplier is a function of ξ and T and, in addition, of an optical depth parameter, $t = \sigma_e \rho l_{\text{Sob}}$, where σ_e is the mass-scattering coefficient for free electrons, ρ is the density and λ_{Sob} the Sobolev length. This length equals to $v_{th}/(dv_l/dl)$, where v_{th} is the thermal velocity while dv_l/dl is the sight-line velocity gradient. However, to reduce the number of parameters, we assumed the temperature dependence can be captured by using the thermal equilibrium value of T for a given ξ so that $M = M(t, \xi, T_{\text{eq}}(\xi), t) = M(t, \xi$ where $T_{\text{eq}}(\xi)$ satisfies the equilibrium equation: $\mathcal{C}(\xi, T_{\text{eq}}) - \mathcal{H}(\xi, T_{\text{eq}}) = 0$.

In Appendix 5, we present a sample of results from our photoionization calculations of T_{eq} and $M(t, \xi)$ for various SEDs (see also Fig. 4.1, for a subset of these results). Following the convention from CAK, Owocki et al. (1988), and Abbott (1982), we characterize the force multiplier dependence on t and ξ using the following parameters, α , k , M_{max} , η_{max} , and δ (see Appendix for the formal definitions).

In Dannen et al. (2020; hereafter D20), we mainly explored how the force multiplier dependence on ξ and t for AGN1 and AGN2 SEDs, in part because we aimed at investigating the so-called overionization problem in line driven winds in AGN. A key constraint on any model for the origin of AGN outflows is the ionization balance. The issue is that on the one hand, we observe very high luminosities in X-rays and the UV, and on the other hand we observe spectral lines from moderately and highly ionized species. The problem is how the gas avoids full photoionization and permits formation of any spectral lines at all (e.g., Arav and Li, 1994; Murray et al., 1995; Krolik, 1999; de Kool and Begelman, 1995; Proga et al., 2000).

Stevens and Kallman (1990) presented one of the earliest quantification of the overionization

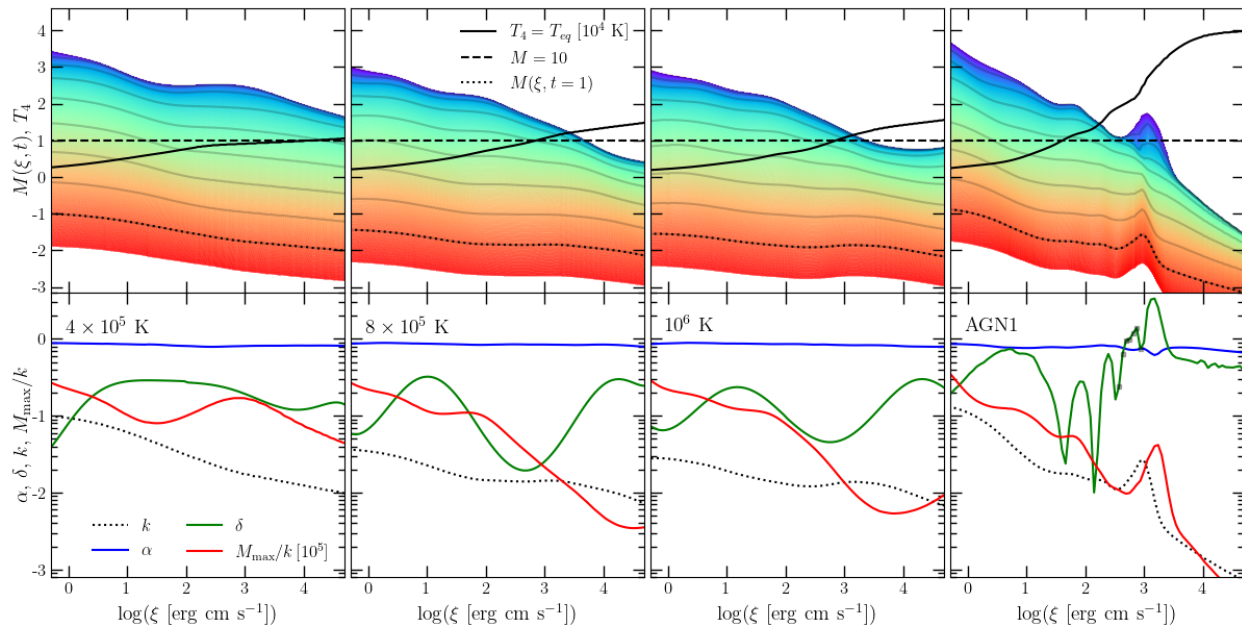


Figure 4.1. Example of results from our photoionization calculations for four SEDs: from left to right, blackbody SEDs with temperatures 4×10^5 K, 8×10^5 K, 10^6 K, and an unobscured AGN SED (AGN1; Mehdipour et al., 2015). *Top panels:* colormap of the force multiplier for t going from $\log t = 1$ (red) to $\log t = -8$ (blue). Black dotted lines mark $M(t, \xi)$, while gray lines indicate $M(t, \xi)$ at $\log t = -1, -2, \dots, -8$. The horizontal dashed line marks the value $M(t, \xi) = 10$, to indicate the level above which line driving can be the dominant outflow driving mechanism. The solid black line is the equilibrium temperature (or S-curve), T_{eq} , in units of 10^4 K. *Bottom panels:* profiles of $\alpha(\xi)$, $k(\xi)$, $|\delta(\xi)|$, and $M_{\text{max}}(\xi)/k(\xi)$ (blue, black dashed, green, and red curves, respectively), the four parameters characterizing the behavior of the force multiplier. To mark negative values of δ we added green squares to the green line in the right panel. The first three parameters are computed along the $t = 1$ curves above to relate our numerical results of the force multiplier to the modified CAK formula. The fourth parameter, $M_{\text{max}}(\xi)/k(\xi)$, is estimated, using $M(t = 10^{-8}, \xi)$ (the upper envelope of the curves above) as a proxy of the maximum force multiplier, $M_{\text{max}}(\xi)$. See Appendix A for more details.

problem using detailed photoionization XSTAR calculations. Assuming a 10 keV bremsstrahlung SED, Stevens and Kallman (1990) found that the force multiplier is a strong function of the photoionization parameter for high values of the parameter. In particular, for a given t , $M(t, \xi)$ quickly approaches zero for $\xi > 100$. This ξ dependence is an illustration of the overionization problem in line driven winds. The results from (Stevens and Kallman, 1990) have been applied to model outflows in AGN for over two decades (e.g., Proga et al., 2000; Proga and Kallman, 2004; Kurosawa and Proga, 2009b; Nomura et al., 2013; Waters and Proga, 2016; Nomura et al., 2020; Quera-Bofarull

et al., 2021; Wang et al., 2022, and references therein). However, the AGN SEDs differ from a bremsstrahlung SED. Therefore, for given ξ and T , the gas exposed to an AGN radiation field can have different spectral lines than that exposed to bremsstrahlung radiation.

In D19, we have confirmed that overall the line force is a strong function of the photoionization parameter for high values of the parameter using AGN SEDs. We also found that for a fixed value of t , the force multiplier is not a monotonic function of the ionization (see the left and second left pairs of panels at the bottom row in Figs. 4.1 and the right panels in B.2). While $M(t, \xi)$ first decreases with ξ for $\xi > 1$ as shown by (Stevens and Kallman, 1990), this decrease is not as strong for both AGN1 and AGN2. In addition, we found that for a fixed t , $M(t, \xi)$ can increase again at $\xi \approx 30$ and $\xi \approx 900$ for AGN1 and $\xi \approx 50$ and $\xi \approx 300$ for AGN2. The main consequence of this behavior is that the multiplier can stay larger than 1 for ξ approaching 10^3 . Moreover, we noted that the range $10^2 \lesssim \xi \lesssim 10^3$ is also where gas is thermally unstable by the isobaric criterion. The regime of thermal instability (TI; Field, 1965) corresponds to the regime where the slope of the slope of the $\log T$ - $\log \xi$ curve is larger than 1, (see the black solid curve in the top panels in Figs.B.2 and 4.1). Thus, a full understanding of this highly ionized regime likely requires coupling photoionization physics with hydrodynamical calculations.

Therefore, we subsequently improved the computational capabilities of including results from D17 and D19 in hydrodynamical simulations. We applied them to study winds in AGN (Dannen et al., 2020; Waters et al., 2021, 2022). One of the intriguing results found by D20 is that in an AGN wind originating at large radii, thermal driving always dominates over line driving. Our initial analysis showed that at the wind base, despite low ξ and an abundance of spectral lines (i.e., large k and M_{max}), the line force is weak. This weakness is caused by large values of the t parameter which indicates large optical depth in lines. On the other hand, at larger radii, ξ is high and there are few lines - the gas is almost fully ionized (i.e., small k and M_{max}). The latter is a manifestation

of the overionization mentioned above. Another manifestation of a very high ionization and the overall decrease in the number of lines, including coolants, is significant Compton heating which leads to runaway heating and TI. The runaway heating makes thermal driven even stronger and line-driven weaker.

The problem of the overionization is a well recognized issue in AGN outflows. However, the problem with too large an optical depth in lines appears to be new and it is related to a self-consistent treatment of the radiation heating and cooling and line driving that takes into account the physical coupling of these processes.

4.1 Scaling Relations

A useful measure of the strength of the thermally driven wind is the ratio of the effective gravitational potential to the thermal energy at the radius of the wind base, r_0 , usually termed the hydrodynamic escape parameter (HEP), that is,

$$\text{HEP}_0 = \frac{GM(1 - \Gamma)}{r_0 c_s^2}, \quad (4.1)$$

where M is the central mass, c_s the sound speed, and Γ is the luminosity in units of the Eddington luminosity L_{Edd} . For $\text{HEP}_0 \lesssim 10$, a thermally driven hydrodynamic (Parker) wind will be produced (e.g., Stone and Proga, 2009, and reference therein). This parameter is related to the density scale height of an isothermal static atmosphere, $\lambda_\rho \equiv |\rho/(d\rho/dr)| = r_0/\text{HEP}_0$. At the base of an outflowing atmosphere, the gas velocity is very sensitive to HEP_0 for $\text{HEP}_0 > \text{a few}$, [i.e., $v_{0,\text{th}} \simeq c_s(\text{HEP}_0/2)^2 \exp(-\text{HEP}_0 + 3/2)$, see e.g., Lamers and Cassinelli (1999)]. Thus the mass-loss rate of the thermally driven wind also exponentially decreases with increasing HEP_0 (i.e., $\dot{M}_{w,\text{th}} \simeq 4\pi r_0^2 \rho_0 v_0$, where ρ_0 is the gas density at the wind base.) This dimensionless parameter is also useful in measuring the strength of the thermal wind from an irradiated disk (see, e.g., Waters et al., 2021).

For line driving, such a measure of the wind strength should also exist but determining it is somewhat more involved. The basic requirement for line driving to dominate gravity is $M_{\max}\Gamma > 1$, where M_{\max} is the maximum value of the force multiplier for a given ξ when even most opaques lines are optically thin. The value of M_{\max} could be as high as a few $\times 10^3$ for low ξ , but it depends on ξ and can be viewed as the upper limit of $M(t, \xi)$ when t approaches zero. However, the above requirement is just a necessary and not a sufficient condition for producing an appreciable line-driven wind, because the actual value of M can be smaller than M_{\max} as the optical parameter is not always very much smaller than unity. Using the Sobolev approximation, CAK showed that $t \propto \rho/(dv_l/dl)$. Thus more information is needed to compute the actual value of M than to compute M_{\max} .

To estimate t , we will use the analytic expression for the mass-lose of the line-driven wind found by CAK:

$$\dot{M}_{w,\text{CAK}} = \frac{4\pi GM(1-\Gamma)}{\sigma_e v_{\text{th}}} \left[\frac{\alpha}{1-\alpha} \left(k\Gamma \frac{1-\alpha}{1-\Gamma} \right)^{1/\alpha} \right], \quad (4.2)$$

where k and α are the parameters of the force multiplier as obtained by CAK, i.e., $M(t) = M_{\text{CAK}} = kt^{-\alpha}$. Note that in the original formulation presented by CAK, k and α do not depend on ξ and thus they are constant. However, in general it is not the case (see below).

Next, we estimate the gas properties near the wind base where gas is gravitationally bound and subsonic so that the density radial profile as very close to the profile of an atmosphere in hydrostatic equilibrium ($1/\lambda_\rho = -\text{HEP}_0/r_0$). On the other hand, using the mass continuity equation for a steady state, isothermal, spherical wind we have $1/\lambda_\rho + 1/\lambda_v + 2/r = 0$ where $\lambda_v = v/(dv/dr)$ is the velocity scale length which at the wind base can be approximated as $\lambda_{v,0} \simeq r_0/(\text{HEP}_0 - 2)$. Finally, using the last expression and the expressions for $\dot{M}_{w,\text{CAK}}$ and t , we estimate the optical depth parameter at the wind base as

$$t_0 \simeq \tau_0^2 \frac{v_{\text{th}}^2}{c_s^2} \frac{1}{\text{HEP}_0(\text{HEP}_0 - 2)} \frac{1-\alpha}{\alpha} \left[\frac{\Gamma}{1-\Gamma} k(1-\alpha) \right]^{-1/\alpha}, \quad (4.3)$$

where $\tau_0 = \sigma_e \rho_0 r_0$. The HEP_0 dependence in Eq. 4.3 can be eliminated when we consider cases where $\text{HEP}_0 > 2$ and that τ_0 is not a free parameter because the radiation heating/cooling and line driving are physically coupled processes. Namely, using Eq. 2.1, we can write

$$\tau_0 = \frac{4\pi c k_B T_{\text{eq}}(\xi_0)}{\xi_0} \frac{\Gamma}{1-\Gamma} \text{HEP}_0 \quad (4.4)$$

or introducing the so-called pressure ionization parameter,

$$\Xi = \xi / (4\pi c k_B T), \quad (4.5)$$

we can rewrite it as

$$\tau_0 = \frac{\Gamma}{1-\Gamma} \frac{\text{HEP}_0}{\Xi_0}, \quad (4.6)$$

to find that

$$t_0 \simeq \left(\frac{\Gamma}{1-\Gamma} \right)^2 \frac{1-\alpha}{\alpha} \left[\frac{\Gamma}{1-\Gamma} k(1-\alpha) \right]^{-1/\alpha} \left(\frac{v_{th}}{c_s} \right)^2 \Xi_0^{-2}. \quad (4.7)$$

Note that the sound speed is a function of ξ_0 via the gas temperature, where as v_{th} is kept constant in calculations of k and α (e.g., Stevens and Kallman, 1990).

In Dannen et al. (2020), we found that for given black hole mass M_{bh} and SED, three parameters govern the solutions: Γ , Ξ_0 , and HEP_0 . These parameters set the strength of thermal driving, for example the mass-loss of the thermal wind can be estimated as

$$\dot{M}_{w,th} = \frac{GM\Gamma}{4c_s\sigma_e} \frac{\text{HEP}_0^2}{\exp(\text{HEP}_0 - 3/2)} \Xi_0^{-1}. \quad (4.8)$$

We could also estimate the optical depth parameter, t , at the base of a thermal wind, $t_{0,th}$. Using the same approach that we used to estimate t_0 and expression for $\dot{M}_{w,th}$, we find

$$t_{0,th} = 4 \frac{1-\Gamma}{\Gamma} \frac{\exp(\text{HEP}_0 - 3/2)}{\text{HEP}_0(\text{HEP}_0 - 2)} \frac{v_{th}}{c_s} \Xi_0^{-1}. \quad (4.9)$$

Here, we show that two of these three dimensionless parameters, i.e., Γ and Ξ_0 , set also the strength of line driving, for given k and α . Eq. 4.7 can be used to explain why line driving

was negligible in the AGN cases we explored earlier. For the wind base to have a relatively low temperature so that the AGN irradiated gas could be on a cold stable branch of the thermal equilibrium and to have many spectral lines, Ξ_0 needs to be less than 10 (e.g., see fig. 1 in D20). However, there is no parameter space with a large the force multiplier because t at the base, t_0 , is not a free parameter: it decreases with increasing Ξ_0 and therefore, it is large for small Ξ_0 .

The line optical depth dependence on Ξ_0 determines the parameter space for line driving in our self-consistent model: if Ξ_0 is low enough for many lines to exist (i.e., large k and M_{max}), the line optical depth could be too large for the line force to operate. To reduce the line optical depth, Ξ_0 would need to be increased but this could reduce the number of driving lines (i.e., small k and M_{max}). Equation 4.9 shows that t at the base at a thermally driven wind exponentially increases with HEP_0 for large HEP_0 which implies that as the thermal wind weakens with increasing HEP_0 , the line driving may not necessary kick in and strengthen a wind because the gas could be too optically thick unless Ξ or c_s or both increase.

In the two AGN cases explored in D20, we found that there is not parameter space for which $M(t, \xi) \Gamma > 1$ even though for a large range of ξ , the line driving has a 'potential' to be important because $M_{max} > 10$ so for $\Gamma > 0.1$, $M_{max}\Gamma > 1$.

In § 4.3, we will elaborate on this point and show specific cases when the potential of the line driving is realized for BB SEDs with temperature, T_{BB} , as high as 10^6 K.

4.2 Simulation Setup

Our time-dependent hydrodynamical simulations are performed in spherical coordinates assuming spherical symmetry, i.e., $(r, \theta = 0, \phi = 0)$ using the magnetohydrodynamic code ATHENA++ (Stone et al., 2020) to solve the equations of hydrodynamics mentioned in § 3.1 We used pre-calculated tables with \mathcal{L} and adopted our interpolation and backwards Euler schemes for determin-

T_{BB} [K]	4×10^5	8×10^5	10^6
T_0 [10^4 K]	5.51	4.76	4.26
ρ_0 [10^{-11} g cm $^{-3}$]	11.1	8.28	0.66
r_0 [10^{13} cm]	1.70	1.95	1.76
Ξ_0	28	32	26

Table 4.1. Example of input parameters for three SED cases with $\text{HEP}_0 = 5$: 4×10^5 , 8×10^5 , and 10^6 BB SED, second, third, fourth column, respectively. For all models, we assumed $M = 10 M_\odot$, $\Gamma = 0.2$, and $\xi_0 = 80$. In addition, we set T_0 to T_{eq} corresponding to ξ_0 for a given SED. Therefore, the inner radius and the density at the base depend only on HEP_0 and we compute them using the following expressions $r_0 = (1 - \Gamma) GM \text{HEP}_0^{-1} c_{s,0}^{-2}$ (see Eq. 3.5) and $\rho_0 = \mu m_p L_{\text{Edd}} \Gamma \xi_0^{-1} r_0^{-2}$ facilitating the definition of ξ . For a reference, we also list Ξ_0 (see Eq. 4.5). We explored models with HEP_0 ranging from 5 to 500 (see Table 4.2).

ing \mathcal{L} as those described in Dyda et al. (2017). We use a similar interpolation method for force multiplier grids computed using the method described in D19 and shown in Fig. 4.1. We initialize the density assuming a hydrostatic atmosphere such that $\rho(r) = \rho_0 \exp(-\text{HEP}_0(r/r_0 - 1))$ with constant temperature set to be $T(r) = T_0 (= T_{\text{eq}}(\xi_0))$. The initial velocity for the models that include heating and cooling is set to 0. However for the isothermal models, we apply the velocity field $v(r) = v_{\text{esc}} \sqrt{1 - r_0/r} \hat{\mathbf{r}}$. At the beginning of our simulations, we use outflow boundary conditions at the inner and outer radii, however after allowing the model to evolve for sometime, we switch to constant gradient boundary conditions at the inner radius, r_0 . We also fix density in the first active zone to the appropriate value as shown in the Table 4.2. Our standard computational domain is defined to occupy the radial range $r_0 \leq r \leq 100r_0$, where r_0 is computed based on our assumed value of ξ_0 . In Table 4.1, we list the main input parameters of our calculations as well as a short summary of how we compute r_0 and ρ_0 . Finally, we adopt logarithmic grid spacing with $\text{x1rat} = 1.0099$ and $\text{nx1} = 1020$. For models that assume CAK or modified CAK (mCAK hereafter) formula, we assume that $k = 0.0076$ and $\alpha = 0.742$.

Model	HEP	$\dot{M} [M_{\odot} \text{ yr}^{-1}]$	η_{wind}	comment
4×10^5 K	5	2.99×10^{-7}	3.55×10^{-2}	steady state
	10	9.78×10^{-8}	1.47×10^{-2}	steady state
	20	5.21×10^{-8}	9.69×10^{-3}	steady state
	50	2.67×10^{-8}	6.41×10^{-3}	steady state
	100	1.71×10^{-8}	5.15×10^{-3}	steady state
	200	1.12×10^{-8}	4.18×10^{-3}	steady state
	500	5.28×10^{-9}	2.55×10^{-3}	steady state
8×10^5 K	5	2.83×10^{-7}	3.82×10^{-2}	steady state
	10	1.16×10^{-7}	1.69×10^{-2}	steady state
	20	2.34×10^{-8}	3.13×10^{-3}	steady state
	50	2.73×10^{-10}	3.05×10^{-5}	variable
	100	1.20×10^{-11}	5.33×10^{-7}	variable
	200	2.46×10^{-13}	3.16×10^{-9}	variable
	500	1.01×10^{-11}	2.18×10^{-6}	variable
10^6 K	5	2.22×10^{-7}	3.10×10^{-2}	steady state
	10	1.03×10^{-7}	1.54×10^{-2}	steady state
	20	3.05×10^{-8}	4.52×10^{-3}	steady state
	50	4.62×10^{-9}	9.84×10^{-4}	steady state
	100	3.31×10^{-9}	1.38×10^{-3}	steady state
	200	3.20×10^{-9}	2.43×10^{-3}	steady state
	500	2.96×10^{-9}	4.54×10^{-3}	steady state
CAK	5	4.91×10^{-7}	5.26×10^{-2}	steady state
	10	4.70×10^{-8}	6.58×10^{-3}	steady state
	20	2.36×10^{-8}	6.23×10^{-3}	steady state
	50	2.09×10^{-8}	9.60×10^{-3}	steady state
	100	2.05×10^{-8}	1.34×10^{-2}	steady state
	200	2.03×10^{-8}	1.88×10^{-2}	steady state
	500	2.01×10^{-8}	2.94×10^{-2}	steady state
$\delta = 0.1$	5	4.84×10^{-7}	5.13×10^{-2}	steady state
	10	3.31×10^{-8}	4.09×10^{-3}	steady state
	20	9.90×10^{-9}	2.21×10^{-3}	steady state
	50	7.38×10^{-9}	2.75×10^{-3}	steady state
	100	6.63×10^{-9}	3.44×10^{-3}	steady state
	200	6.11×10^{-9}	4.38×10^{-3}	steady state
	500	5.59×10^{-9}	6.13×10^{-3}	steady state
$\delta = 0.3$	5	4.73×10^{-7}	4.93×10^{-2}	steady state
	10	1.91×10^{-8}	1.97×10^{-3}	steady state
	20	7.33×10^{-10}	1.20×10^{-4}	steady state
	50	2.60×10^{-10}	7.33×10^{-5}	variable
	100	1.79×10^{-10}	7.07×10^{-5}	variable
	200	1.20×10^{-10}	6.59×10^{-5}	variable
	500	9.14×10^{-11}	7.67×10^{-5}	variable

Table 4.2. List of the simulations considered in this work and summary of some gross properties of the wind solutions. The first column list the model case, from the top to the bottom: self-consistent model with radiative heating and cooling and line driving based on the results from photoionization calculations for 4×10^5 , 8×10^5 , and 10^6 BB SEDs, isothermal model using the CAK, and two modified CAK expression for line driving with $\delta = 0.1$ and 0.3 . The second column list HEP₀ value. The third and fourth column lists the wind mass loss rate and momentum efficiency, \dot{M}_w and $\eta_{\text{wind}} \equiv \dot{M}_w v_{\text{out}} c / (L_{\text{Edd}} \Gamma)$, respectively. We plot these two and other wind properties as functions of HEP₀ in Fig. 4.3. Finally, the last column provides the information whether the wind solution reached a steady state or remained variable.

4.3 Results

The original application of the CAK theory was to explain mass outflows from OB stars. As we mentioned in § 4, the theory has been applied to outflows in CVs and AGNs. In such accretion disk systems, the range of atmospheric temperatures is much wider than among OB stars; in CVs and AGNs, temperatures can be about 10^3 K or less and as high as a few 10^5 K typically. AGNs have the additional complication that the X-ray source compared to the thermal BB-like source can be significantly stronger than in CVs.

To keep our exploration of the various radiative environments general and manageable, we will focus here on BB SED cases with the temperature significantly higher than that applicable to OB stars.

As we described in the Appendix, M_{max} typically decreases with increasing ξ (see Figs. B.2 and B.3). This downward trend is especially strong for AGN and XRB SEDs and for BB SEDs with $T_{BB} \gtrsim 4 \times 10^5$ K. However, for $T_{BB} \lesssim 4 \times 10^5$ K, M_{max} is relatively high and stays about the level of 10 even for $\log \xi$ as high as 5. Thus, $T_{BB} \approx 4 - 6 \times 10^5$ K marks the transition to the regime for which the line driving will not be significant because even the necessary condition for driving is not satisfied for high ξ .

To investigate the wind solutions in more detail for various BB SEDs, we choose the 4×10^5 BB SED case to be representative of the regime where the necessary condition is satisfied for a wide range of ξ whereas the 8×10^5 BB SED and 10^6 BB SED as representative regimes where the necessary condition is satisfied only for small and intermediate ξ . We also consider the former as one that belongs to the class of cases defined by OB stars (with no or weak effects due to ionization) whereas the latter as those that belong to the class of high energy SEDs where the effects due to ionization are strong and can lead to significant ionization (see, Fig. B.3 for a comparison of the key force multiplier characteristics for all SEDs). We note that the ionization effects in these high

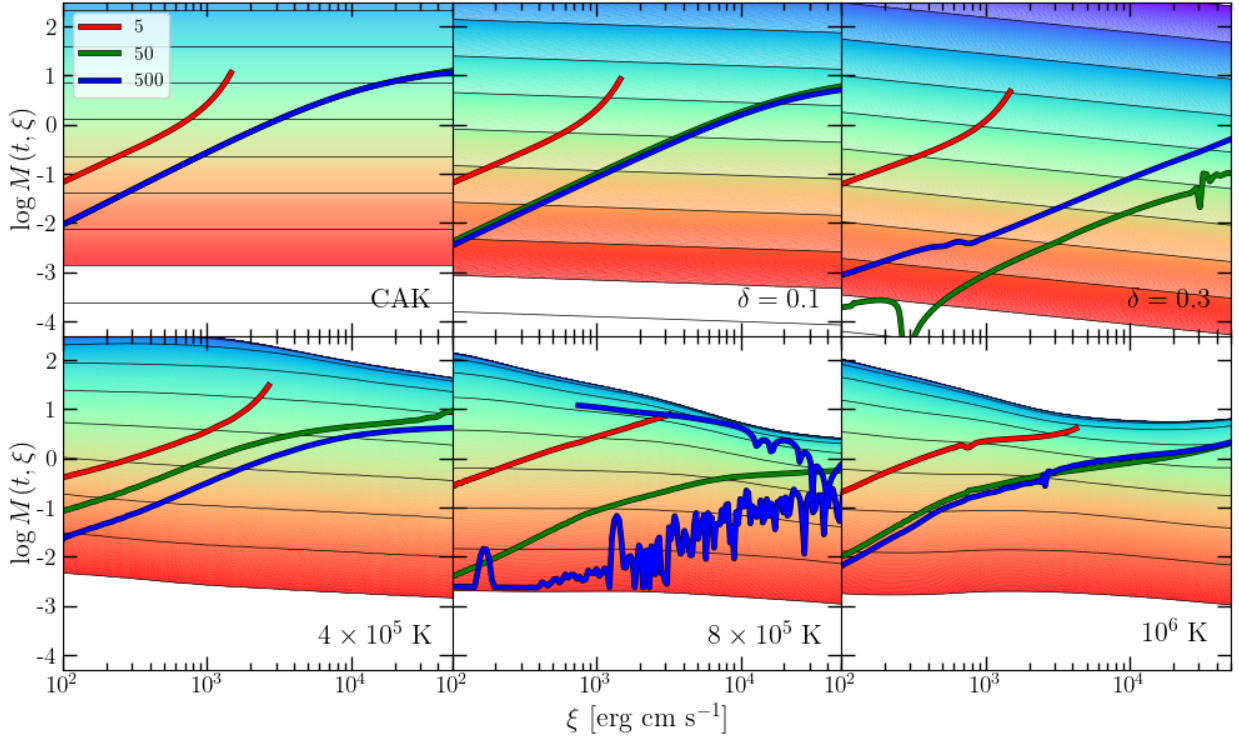


Figure 4.2. The force multiplier as a function of ξ for a subset of our wind solutions. Each panel shows results for $\text{HEP}_0=5, 50, \text{ and } 500$ (red, green, blue curves) our six cases presented in this work: 1) CAK (i.e., $\delta = 0$ top left panel); 2) mCAK with $\delta = 0.1$ (top middle panel); 3) mCAK with $\delta = 0.3$ (top right panel); and 4-6) $4, 8, 10 \times 10^5$ BB SED cases (the bottom panels, from left to right). For a reference, in each panel we also plot the force multiplier as a function of ξ for fixed values of optical depth parameter, t : $\log t = -8, -7, \dots, 0, 1$). In the top panels, the solid lines are by design straight lines, equally spaced and with the slope equal to $-\delta$ (see the appendix including Eq. B.2). In the bottom panels, the force multiplier is computed based on the photoionization calculations and its t and ξ is more complex, for example the solid lines converge for small t which reflects the saturation of $M(t, \xi)$ as t approaches zero. This saturation is most apparent for the 8×10^5 BB SED case and has a significant effect on the wind solution especially for high HEP_0 simulations where the solution is highly time dependent.

temperature BB SED case are not as strong as AGNs (see, e.g., Fig. 4.1 for a comparison of the force multiplier for the three BB SED cases and the AGN1 case but also Figs. B.2 and B.3). In AGN and XRBs case, the radiation is so hard that it can not just strongly ionize the gas but it can fully ionize the gas and lead to TI, note for example, a drop in M_{max}, k, η_{max} with ξ . On the other hand, in all our BB cases, the gas is thermally stable as indicated by the slope of the $\log T - \log \xi$ which is less than 1 for all ξ (see the solid black curves in the top panels in Fig. 4.1 and the top panels of the pair of panels shown in Fig. B.2). Thus, one can expect that even for our

highest T_{BB} cases, the wind solution will be qualitatively different from thermally unstable AGN and XRB cases.

In Table 4.2, we summarize the main parameters for all simulations that we present in this paper. The table also lists the wind mass loss rate, \dot{M}_w , momentum efficiency $\eta_{\text{wind}} \equiv \dot{M}_w v_{\text{out}} c / (L_{\text{Edd}} \Gamma)$ and whether the wind solution reached a steady state or remained variable even after running the simulations for 2 or even 8 sound crossing times (i.e., a few $100 r_0 / c_{s,0}$).

Our illustrative wind simulations are 1D radial flows. Therefore, it may come as a surprise that not all simulations resulted in steady state solutions akin to time independent CAK solutions (see right column of Table 4.2). We have investigated possible causes of this variable behavior and concluded it is not a numerical effect. So as to not limit the results of our parameter survey to steady solutions, these variable solutions have been included in our analysis, with wind properties quoted after time-averaging the solutions. We plan on investigating in more detail the dynamics leading to variability in a future study. In § 5, we offer a brief discussion of these variable solutions and cite a couple of previous works that reported on oscillations in the outflows.

In Fig. 4.2, we show how the force multiplier varies as a function of ξ for in 18 different wind solutions. We present results for $\text{HEP}_0 = 5, 50, \text{ and } 500$ (red, green, blue curves) in six cases: 1) CAK (i.e., $\delta = 0$ top left panel); 2) mCAK with $\delta = 0.1$ (top middle panel); 3) mCAK with $\delta = 0.3$ (top right panel); and 4-6) $4, 8, 10 \times 10^5$ BB cases (the bottom panels, from left to right).

The CAK case corresponds to the case we discussed in § 4.1. The wind solutions for this case show that indeed in a cold regime, where ($\text{HEP}_0 \gtrsim 5$) the wind solution does not depend on HEP_0 (see also Table 4.1 and Fig. 4.3 where we show some gross wind properties as functions of HEP_0). For example, in the top left panel of Fig. 4.2, the curves for $\text{HEP}_0 = 50$ and 500 overlap and are different than the red curve corresponding to $\text{HEP}_0 = 5$ which is the hot solution where the wind is driven by the pressure force not the line force.

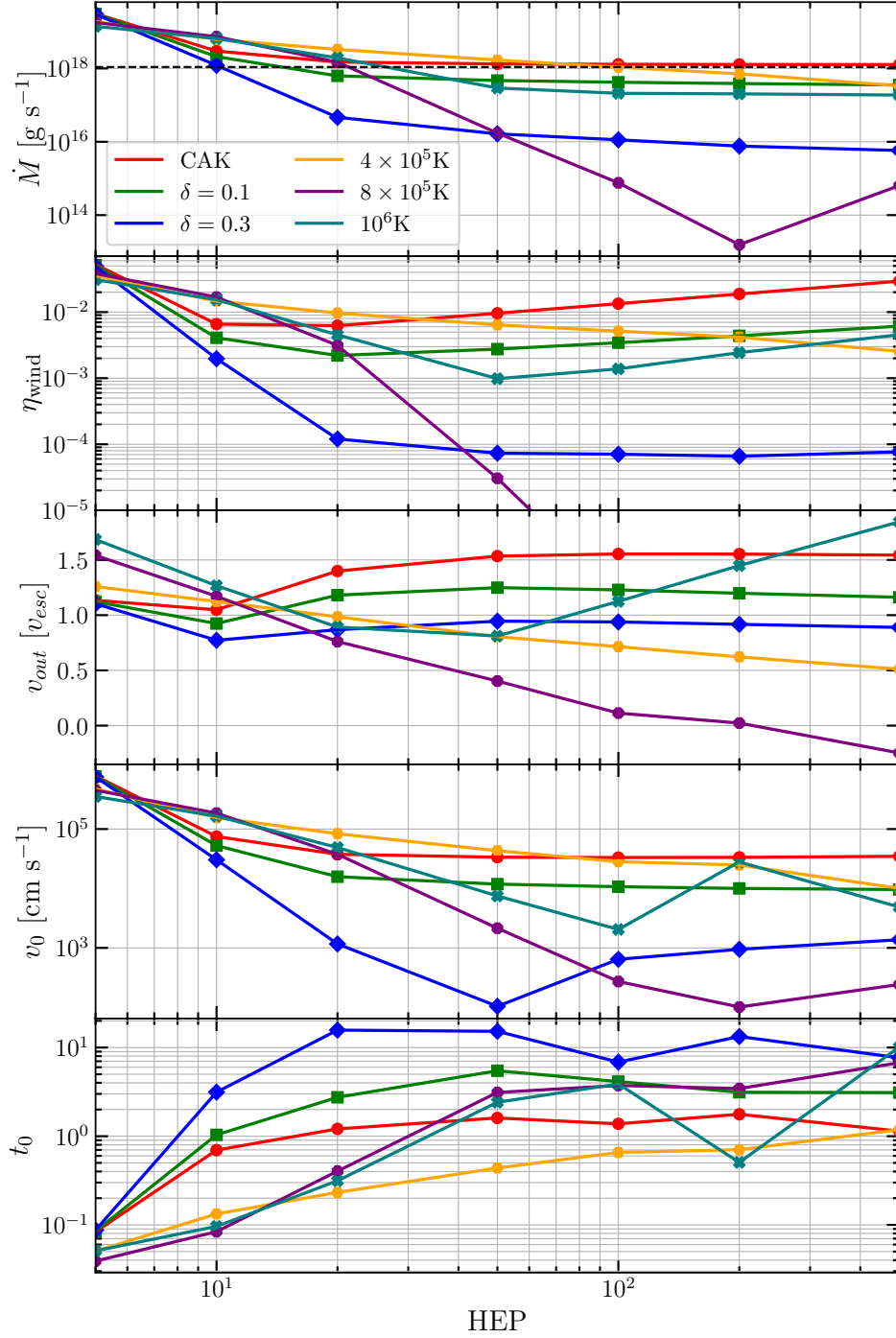


Figure 4.3. Comparison of the gross properties of our wind solutions as a function of HEP_0 . From top to bottom, those quantities shown are the mass flux, wind momentum efficiency $\eta_{\text{wind}} = v\dot{M} (c / (\Gamma L_{\text{Edd}}))$, velocity as the gas exits the outer grid cell in units of escape velocity defined at the inner radius ($v_{\text{esc}} = \sqrt{2GM/r_0}$), v_{out} velocity at the inner radius, v_0 , and optical depth parameter at the inner radius, t_0 . The horizontal black dashed line in the top panel represents $\dot{M}_{w,\text{CAK}}$ (see Eq. 4.2).

In the $\delta = 0.1$ mCAK case, we also see that the wind solutions for $\text{HEP}_0=50$ and 500 very similar. Fig. 4.3 indicates that the transition between the 'hot' to 'cold' solutions (i.e., to those that become insensitive to HEP_0) occurs at $\text{HEP}_0 \approx 20$.

In the other four cases: $\delta = 0.3$ mCAK, 4×10^5 BB, 8×10^5 BB, and 10^6 BB SED, the wind solutions depend on HEP_0 for all HEP_0 . These are the cases where the force multiplier quite strongly decreases with increasing with ξ for a given t (see for instance, the slopes of the solid lines plotted in fig. 4.2 and the decrease of k in increasing ξ in the lower panels of Fig. 4.1). This decrease of the force multiplier with increasing ξ results in the weakening of the wind as measured, for example by the wind mass loss rate and velocity in units of the escape velocity that both decrease with increasing HEP_0 for large HEP_0 (see the top and third from the top panel in Fig. 4.3).

In § 4.1, we cited the expression for $\dot{M}_{w,\text{CAK}}$ (see Eq. 4.2) and derived an expression for t_0 (i.e., Eq. 4.7). These two quantities are HEP_0 independent for large HEP_0 , in the cold wind regime and under the assumption that k is a constant. Our numerical solutions for the CAK case are consistent with this prediction as shown by the red lines in Fig. 4.3. In the other cases that we presented here, k varies with ξ either explicitly via a power-law scaling with ξ or v (i.e., non zero δ in mCAK cases) or implicitly when we use our photoionization calculations.

The main physical reason for this HEP_0 sensitivity can be described in the following way: \dot{M}_w and other key wind properties, including t_0 are determined at the wind critical radius (r_c , see Lamers and Cassinelli, 1999, for an overview). If the k parameter decreases with increasing ξ then one can still consider to eqs. 4.2 and 4.7 to gain some insight but for k , the value at r_c should be used.

As we increase HEP_0 , the gravity relative to both the gas pressure and line forces also increases. As a result, the flow velocity at the base decreases while the escape velocity increases with increasing HEP_0 (e.g., note that by keeping M , Γ and ξ_0 $r_0 = (1 - \Gamma) GM \text{HEP}_0^{-1} c_{s,0}^{-2}$, see also Table 4.1) and see second from left panel in Fig. 4.4 for specific examples). This in turn means that

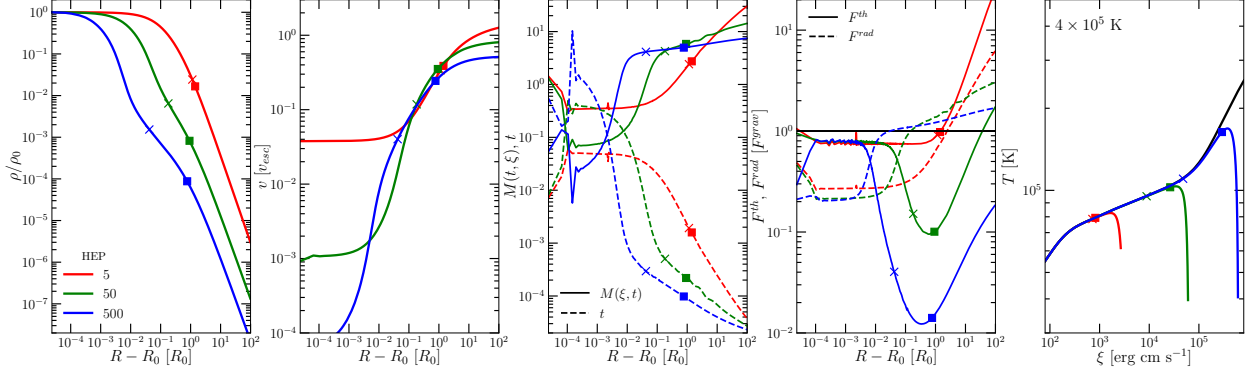


Figure 4.4. Properties of winds for the 4×10^5 BB SED case. We show three solutions that correspond to $\text{HEP}_0 = 5, 50, 500$ (red, green, and blue lines respectively). Proceeding left to right, the first panel shows the density in units of the density at r_0 , ρ/ρ_0 . The second panels shows the radial velocity. The third panel shows both force multiplier, $M(t, \xi)$ (solid), and the line optical depth parameter, t (dashed), as functions of radius. Fourth panel displays the radiation force, F^{rad} , and gas pressure, F^{th} , normalized to the force of gravity, F^{grav} , as a function of radius. The final right most panel shows the phase diagram (i.e., $\log T$ vs. $\log \xi$) for all three wind solutions. The solid black curve corresponds to the thermal equilibrium (“S-curve”, i.e. where $T = T_{eq}(\xi)$). The x’s and squares in matching color on each curve mark the sonic and critical radii, respectively).

for the wind to reach at least the escape velocity, its velocity must increase by a large factor so does ξ . Therefore as the flow accelerates its ξ increases which leads to a decreases of the force multiplier for a given t . To maintain, the net outwards force the wind density must decrease while the velocity gradient must increase so that the force multiplier can sufficiently high due to decreasing t . To explicitly illustrates these dependencies, in Fig. 4.4, we plot several wind properties and forces acting on the wind as functions of radius for the 10^6 BB SED case and three values of HEP_0 . The right panel shows explicitly that ξ at the critical radius increases with increasing HEP_0 (compare the position of the points marked by the black squares). The right hand sides of eqs. 4.2 and 4.7 depend therefore indirectly on HEP_0 through k . Formally, there is also indirect dependence through α . But α is a very weak function of ξ even in our self-consistent cases (see the blue solid lines in Figs. 4.1 and B.2).

Eqs. 4.2 and 4.7 are of less help to gauge the effects of changes in M_{\max} or η on the wind properties. But generally one can expect that too large a decrease in M_{\max} with ξ will lead

to the line force inability to remain stronger than gravity downstream (see Proga, 1999, for an earlier exploration of the effects of the force multiplier saturation on disk and wind solution using a modified CAK method). This limited growth of the force multiplier can prevent the wind from developing, or from being strong like found by Proga (1999) and us here. But moreover the force multiplier saturation can lead to a highly variable wind solution as we found here in high HEP_0 simulations for the 8×10^5 BB SED cases (see, for instance, the blue line in the bottom middle panel of Fig. 4.2).

CHAPTER 5: DISCUSSION OF RESULTS & FUTURE WORK

The luminosity of AGNs is very high and very likely a significant fraction of their Eddington luminosity (Giustini and Proga, 2019, and references therein). Therefore, the line force must play a role in at least launching but even accelerating winds from accretion disks in these systems. These winds could account for the so-called broad absorption lines (see Giustini and Proga, 2019, for a review of both observational and theoretical arguments). In this radiation driven disk wind scenario, the overionization problem is solved by self-shielding, i.e., attenuation of the X-rays from the central object by the disk atmosphere so the X-ray cannot prevent the local disk radiation from pushing matter away from the disk (e.g., Proga et al., 2000; Proga and Kallman, 2004; Nomura et al., 2013, 2020; see also Murray et al., 1995, for the idea of a 'hitch-hiking' gas shielding the disk wind). The wind acceleration and its terminal velocity are sensitive to the X-ray opacity and radiation transfer effects such as photon scattering (Proga and Kallman, 2004; Sim et al., 2010; Higginbottom et al., 2014). Therefore, the line force alone may not suffice to accelerate winds to velocities that are on the order of 10% the speed of light. However, the launching seems very robust because overionization is not an issue near the disk surface where the ionization parameter is relatively low due to a high gas density.

The robustness of the launching was explored by Proga and Kallman (2004) who considered the 'worst case' scenario for line driving of disk winds in AGN. Specifically, they showed that no self-shielding is needed to launch a wind from luminous AGN where M_{BH} is very high (i.e., $> 10^8 M_{\odot}$) so that the disk radiation is relatively soft and is dominated for the UV radiation. However, their assumption that the force multiplier parameters do not depend on the disk local BB SED. This assumption was motivated by the results from modeling of line driving from OB stars, where it was shown that the energy distribution of the line opacity follows the SED as the star temperature changes and consequently k and α do not significantly change with the SED (e.g.,

Abbott, 1982; Lamers and Cassinelli, 1999). However, the temperature range in luminous stars is relatively narrow, it ranges from 10^4 K to 5×10^4 K. This range is certainly narrower than the range expected in AGN disks where the disk inner temperature can be 10^5 K if not enough much more. Thus, it is possible that outside the OB temperature range the line force can significantly depend on the BB SED. In particulate, above some disk temperature, k can decrease with increasing T_{BB} .

It is in this context that we discuss our results here. We surveyed the parameter space of line forces resulting from various temperature BB SEDs, while also self-consistently computing the heating and cooling balance to compute the temperature. Our main finding is a quantification of how the line force and the wind properties depend on the assumed SED and the key parameters characterizing the wind base such HEP_0 . Specifically, we found that the line force is relatively insensitive to the BB SEDs with the temperature as high as 2×10^5 K, so well above the temperature of OB stars. This means that the line force has a similar capability for launching wind over a wide range of disk radii including the radii close to the inner disk radius in very high M_{BH} where much of the accretion luminosity is liberated. This result also indicates that models of mass lose from the central objects of young planetary objects as well as accreting white dwarfs with the surface temperature of order of 2×10^5 K could be viewed as an high temperature extension of the models for OB stars.

Accretion disks in AGN, and also CVs, are geometrically thin as their thermal energy is small compared to the huge gravitational energy of the central compact object (the corresponding $\text{HEP}_0 >$ a few thousand even). Here, we found that for some BB SEDs as HEP_0 increases the wind weakens but can reach a steady state. However, for some BB SEDs (e.g., 8×10^5 BB case) while the wind also weakens with increasing HEP_0 , in addition, it becomes variable for $\text{HEP}_0 \gtrsim 50$. Axisymmetric time-dependent simulations by Proga et al. (1998); Proga (1999) showed that line-driven disk winds are intrinsically variable even when the force multiplier parameters are constant and for $\delta = 0$ (see

also Dyda et al., 2020, for a confirmation of this result in the upgraded and 3-D counterparts of these simulations). It is possible then the variability that we found, can make disk winds even more variable.

We noted that in the 8×10^5 BB case, the δ parameter is relatively high, (i.e., 0.3, higher than for typical OB cases, (see, e.g, Lamers and Cassinelli, 1999). To elucidate the cause of this variability, we have explored a few isothermal cases using a modified CAK method. We found that even for these relatively simple cases the wind is variable, even periodic, for $\delta = 0.3$. Therefore, we attribute this variability to weakening of the line force with increases wind velocity. (recall that δ is a measure how quickly k decreases with increase ξ or the wind velocity, see eq. B.2). We plan on further investigating this variable solution. However, two points are worth noting: 1) Curé et al. (2011) studied line driven winds for various δ and stated that they were not able to find any steady state wind solution in the interval $0.22 < \delta < 0.30$. We did find solutions in this interval but they are unsteady; 2) in a stratified atmosphere, the velocity amplitude of the propagating sound waves increases with altitude (e.g., see Clarke and Carswell, 2014, for a textbook elaboration on this plot). Therefore, we expect that the wind variability in high δ cases is related to the propagation of sound waves in the wind base and then farther in a weak wind which is also slower compared to a stronger wind for a small δ . The lower wind velocity which is related to the smaller acceleration appears to be the key: when the acceleration is large the waves are stretched downstream and they do not affect the wind, while when the acceleration is small the wave survey over large distances and the related pressure force can affect a wind that is driven by a weak line force. Our unsteady wind solutions could also be related to some previously reported cases. For example, Owocki et al. (1994) found that the density at the wind base affects the wind solution including its temporal behavior. Specifically, a steady state transonic outflow exists for a narrow range of ρ_0 . For too small ρ_0 , the outflow is supersonic already at the base whereas for too large ρ_0 . Owocki et al. (1994) wrote

that they “encountered a kind of boundary ‘stiffness’ that induces a persistent base oscillations in density and velocity.” Similar issues were noticed by Proga et al. (1998) and Proga et al. (1999). In addition, Proga et al. (1999) checked how line-driven disk wind solutions depend on the sound speed at the base, which is equivalent to the dependence on HEP_0 . He found that although the mass loss rate and velocity do not depend on c_s , the time behaviour of the isothermal winds does depend on it. For example, the fiducial state-state solution model from Proga et al. (1998) recalculated with c_s reduced by a factor of 3 (corresponding to an increase of HEP_0 by a factor of 3) is somewhat time-dependent: density fluctuations originating in the wind base spread in the form of streams sweeping outward. Generally, he found that wind time dependence weakens with increasing c_s because the gas pressure effects get stronger with increasing c_s . Subsequently higher gas pressure smooths the flow more effectively and in a larger region above the disk mid-plane as the size of the subcritical part of the flow increases with c_s . Thus, in retrospect, our systematic parameter survey appears to include some cases that have been explored before by others concerned with setting up the lower boundary conditions appropriate to simulate an outflow that is subsonic near the base, goes through a critical point, and becomes supersonic at some finite distance from the base.

The main conclusion of this work is that the line force can operate over a very wide range of SEDs and of the ratio between the gravitational and thermal energies. In other words, this force seems to be able to operate in both warm and cold regimes and in situations the mean photon energy is relatively high. This is well beyond the conditions for which the original CAK solutions were obtained, i.e., the cold regime of winds from OB stars. Future modeling of the astrophysical outflows including self-consistent radiative heating and cooling rates and the line-force will likely lead to new insights into the properties of line driven winds, in particular such basic ones like the wind efficiency, velocity and temporal behavior. This work shows the results from our method of self-consistently including those processes and hopefully the potential for future insights.

APPENDIX A: LTE VS. NON-LTE CALCULATIONS

One of the main challenges in estimating the force multiplier is the ability to properly compute the level populations, and although it is common to assume a Boltzmann distribution for the level populations (see §2.5), this assumption may not be appropriate for AGN, unjustifiably adding the contribution of thousands of additional lines. One needs to have complete atomic data in order to solve the statistical equilibrium equations instead of assuming a Boltzmann distribution. To explore non-LTE effects, we used only the lines available in `XSTAR` because not all necessary atomic data is available for many lines included in Kurucz’s list. `XSTAR` contains information about the vast majority of UV and X-ray lines included in our combined line list, and those are the lines present when the gas is highly ionized.

The non-LTE calculation shown in Fig. A.1 (blue dash-dotted line) is a demonstration of how a more complete treatment of the level populations reduces the force multiplier. Our result that $M(\xi, t)$ can exceed unity for $\log(\xi)$ as large as 3 followed from the common practice of assuming a Boltzmann distribution for the level populations (see §2.5). When we loosen this assumption by using the level populations determined by `XSTAR` to compute $M(\xi, t)$ in a manner fully self-consistent with the heating and cooling rates, the population of the excited states is decreased. The reason is simply that it is common for the temperature of photoionized plasmas to be an order of magnitude or more smaller than the ionization potential of H and He-like ions, so many excited state transitions that are collisionally populated in the LTE case can only exist if they become radiatively populated in the non-LTE case and radiative excitations can be highly sensitive to the incident SED. Consequently, the general expectation is a significant reduction of $M(\xi, t)$.

Omitting lines that are exclusively present in Kurucz’s list can also have a significant effect on the force multiplier, but only for low to moderate ξ . We verified that for AGN1 with $\xi \gtrsim 100$ and AGN2 with $\xi \gtrsim 200$, there is no significant change in $M(\xi, t)$ when comparing Boltzmann

distribution calculations done with and without the combined line list. This means that non-LTE effects are most important for $\log(\xi) \gtrsim 2$, while for $\log(\xi) \lesssim 2$ we have found that non-LTE effects and the reduced line list contribute about equally to the ~ 1 order of magnitude reduction in $M(\xi, t)$. It is therefore likely that if we were able to perform a full non-LTE calculation using the combined line list, we would find that $M(\xi, t)$ is nearly as large as the black line in Fig. A.1, but only for $\log(\xi) \lesssim 2$.

For $\log(\xi) \gtrsim 2$, the reduction in the line force is almost entirely due to non-LTE effects, and Fig. A.1 shows $M(\xi, t)$ is smaller by more than two orders of magnitude, a finding at odds with our result that $M(\xi, t)$ can remain larger than unity out to $\log(\xi) \approx 3$. This in itself is an important result, as the LTE approximation is a standard one when computing force multipliers (e.g., CAK; Abbott 1982; SK90; Gayley 1995; Puls et al. 2000). Note that it is dependent on the value of density we have assumed. If densities are much greater than those considered in this work, the resulting $M(\xi, t)$ will be larger due to the greater populations of the excited levels due to electron collisions.

In consideration of our earlier discussion highlighting the fact that the gas is thermally unstable in the range $2 \lesssim \log(\xi) \lesssim 3$, the non-adiabatic hydrodynamics may dictate that force multipliers in this range of ξ are seldom even sampled. Understanding this highly ionized regime is likely impossible from the standpoint of photoionization physics alone; the gas dynamics must also be taken into account.

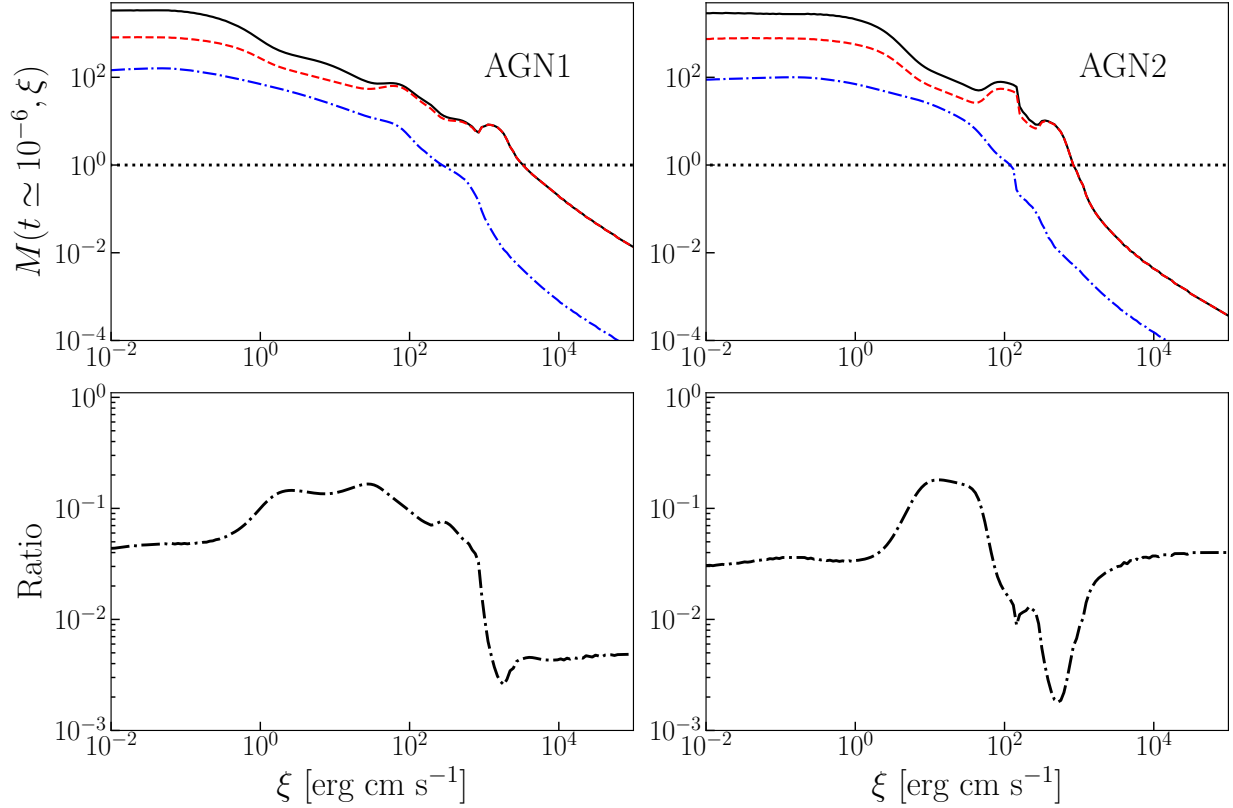


Figure A.1. Comparison of LTE and non-LTE force multiplier calculations for AGN1 (left) and AGN2 (right), assuming $t = 10^{-6}$. *Top Panels:* The solid black line is $M(\xi, t)$ from Fig. 2.3 that assumes a Boltzmann distribution for the level populations. The blue dash-dotted line is $M(\xi, t)$ found without making the Boltzmann distribution assumption but with the level populations determined by `xstar` and including only lines contained in `xstar`. *Bottom Panels:* The black dash-dotted line is the ratio of the blue dash-dotted and black solid lines, illustrating how the combination of a smaller line list and a non-LTE treatment of the level populations reduces $M(\xi, t)$.

APPENDIX B: THE EQUILIBRIUM TEMPERATURE AND FORCE

MULTIPLIER

Here, we summarize some results from our photoionization calculations of the equilibrium temperature and force multiplier from D17 and D19. In Fig. B.2 consists of fourteen pairs of panels for fourteen SEDs (the SED's label is shown in the bottom left corner of the bottom panel of each pair). In the top panel for each pair/SED, we show how the gas equilibrium temperature (in units of 10^4 K) and the force multiplier depend on ξ . We use the solid black curve for T_{eq} and the dotted curves with the space between them filled with color bands for M (the thick dotted line is for M with $\log t = 0$ while the thin dotted curves are, from the bottom to the top, with $\log t = 1, -1, -2, \dots, -8$). In addition, the horizontal thick dashed line in each of the top panels corresponds to the $M = 10$ level.

Our results show that regardless of a SED, for a fixed ξ , $M(t, \xi)$ asymptotically approaches 0 as t becomes large and a constant as t approaches zero. We will refer to this constant, $M_{\text{max}}(\xi)$. For intermediate values of t , the force multiplier monotonically increases with decreasing t . On the other hand, the dependence on ξ for a fixed t can be non-monotonic and specific to a given SED and a specific value of t . For example, $M_{\text{max}}(\xi)$ is of an order of a few $\times 10^3$ for small ξ in all SED cases, except for the two XRB cases where it is an order of magnitude smaller. Then as ξ increases, $M_{\text{max}}(\xi)$ decreases gradually for the BB SEDs with $T_{\text{BB}} \lesssim 10^5$ K and decreases strongly for the hotter BB SED cases and even more strongly for the AGN and XRBs cases.

I reckon that for a given SED, it might be possible to capture the force multiplier dependence on t and ξ using some analytic formulae as for example Stevens and Kallman (1990) did for a 10 keV bremsstrahlung. But we opt to use the actual results from our photoionization calculations in a tabulated form. Nevertheless, we find that it is instructive and useful to relate our results to some well-known and often-used scaling relations.

The t dependence of the force multiplier, including its asymptotic behavior that we found are, of course, consistent with the results first found by CAK. They showed that for the large and intermediate values of t , the force multiplier can be well approximated by the following power-law: $M_{\text{CAK}}(t) = k_{\text{CAK}}t^{-\alpha}$, where k_{CAK} and α are constants that can be estimated by fitting the above formula to the results from ionization calculations or using a theoretical approach that considers a statistical distribution of the line opacity as a function of the line opacity and of the line frequency. The saturation of the force multiplier for very small t corresponds to a optically thin limit for all the lines, including the strongest lines. They estimated that M_{max} is of order of a few $\times 10^3$ for OB stars and that it is determined by chemical composition, atomic data, including an upper limit to the opacity distribution in a given assembly of lines. Motivating by this scale, we can express $M(t, \xi)$ in the following way

$$M(t, \xi) = M(t = 1, \xi)t^{-\alpha}\epsilon_{fm}(t, \xi), \quad (\text{B.1})$$

where $M(t = 1, \xi)$ is a normalization factor which is just a ξ dependent version of the k_{CAK} parameter ($k(\xi)$ hereafter), and $\epsilon_{fm}(t, \xi)$ is a factor correcting the CAK like scaling for additional dependence of $M(t, \xi)$ on t and ξ , for example to account for $M(t, \xi)$ saturation as t approaches zero. As a proxy for $M_{\text{max}}(\xi)$, we use $M(t = 10^{-8}, \xi)$.

To parameterize the force multiplier dependence on ionization at moderate t , we compute the slope of the force multiplier- ξ relation at $t = 1$: $\delta(\xi) \equiv -\partial \log M(t, \xi) / \partial \log \xi|_{t=1} = d \log k(\xi) / d \log \xi$. Here, we follow the approach adopted by Abbott (1982) who introduced this parameter to estimate the effect of ionization on the force multiplier through the following factor $(n_{11}/W)^\delta$, where n_{11} is the number density in units of $10^{11} \text{ cm}^3 \text{ s}^{-1}$ and $W = W(r)$ is the geometrical dilution factor. In our photoionization calculations of δ corresponds to that introduced by Abbott (1982) because $J \propto W$ and using the definition of ξ (i.e., Eq. 2.1) one finds that $\xi \propto W/n$. We use δ to approximate

the k dependence of ξ :

$$k(\xi) \simeq k_0(\xi/\xi_0)^{-\delta}, \quad (\text{B.2})$$

where k_0 is the value of $k(\xi)$ for a fiducial value of the ionization parameter, ξ_0 .

In bottom panel of each pair/SED, we plot four parameters characterizing the force multiplier using the convention from CAK and Abbott (1982). Specifically, we show $\alpha(\xi) \equiv \partial \log M(t, \xi) / \partial \log t|_{t=1}$ (solid blue curve); $k(\xi) \equiv M(t = 1, \xi)$ (black dashed curve; note, it is the same quantity shown as the thick black dotted line in the corresponding top panel), δ (green curves or green curves with squares if δ is negative, i.e., where k increases with ξ) and finally $M_{max}(\xi)/k(\xi)$ ($= M(t = 10^{-8}, \xi)/M(t = 1, \xi)$ in units of 10^5 , solid red curve).

These four parameters can be used to assess how the force multiplier shown in the top panel departure from the scaling introduced by CAK for which α , k , and δ do not depend on ξ , and M_{max} is huge (formally infinite) while $\delta = 0$. Just for the reference, note that for CAK's scaling the dashed lines would be purely horizontal and equally spaced from each other (i.e., lines representing $M(t, \xi)$ as a function of ξ for a given t , see the top left panel in Fig. 4.2).

Our results show that $\alpha \approx 0.8 - 0.9$ for all BB SEDs. So it is a relatively very weak function of ξ . It is a somewhat stronger function for AGN1/2 and XRB1/2 SEDs and has a tendency to slightly decrease with increasing ξ (it decreases from $\approx 0.8 - 0.9$ for $\log \xi \lesssim 2$ to $\approx -0.5 - 0.6$ for $\log \xi = 5$).

The other quantities are more sensitive to ξ especially for high temperature BBs and AGN and XRB cases. This was also found by Stevens and Kallman (1990) for the 10 keV bremsstrahlung. The dependence of the force multiplier on ξ is reflected in a non-zero value of δ which could be as high 1 in the cases with a relatively hard SEDs. This value of δ is much higher than in OB stars where $\delta < 0.2$ (see for example table 8.2 in Lamers and Cassinelli, 1999, and references therein) and in our results for BBs where δ does not exceed 0.4. We note that δ is negative for some ξ which

is an indication that the force multiplier can be a non-monotonic function of ξ as found by D19. CAK showed k is related to the total number of spectral lines. Therefore, the dependence of k on ξ is related to a variation in total line number so it is not too surprising that δ could be negative for some ξ (note that a possibility of δ being negative in OB star cases has been mentioned by Puls et al., 2000).

The dependence of k on ξ is dynamically important because for example the wind mass loss rate depends in k (see Eq. 4.2). A by-eye inspection of our results indicates that of the k - and δ - ξ dependencies can be well captured by a single power-law for BBs with the temperature $\lesssim 10^5$ K while a broken-power-law would be required for the higher temperature BBs. The AGN and XRBs cases are more complicated as both k and δ are non-monotonic functions of ξ . Piecewise functions (e.g., a combination of several power-laws or of power-laws and exponential functions) would be required as also found by (Stevens and Kallman, 1990).

In our hydrodynamical simulations, we have used tabulated values of $M(t, \xi)$ rather than fits to these values. Nevertheless, the δ parameterization of the $k - \xi$ dependence (see Eq.B.2) has proven to be very useful in interpreting our hydrodynamical results and make a more direct connection with previous work by Abbott (1982) and others.

Our last parameter is related another way of characterizing the force multiplier saturation. We herecite work by Owocki et al. (1988) who explicitly accounted for the saturation, by modifying the CAK statistical model cutting off the maximum line strength and thereby limiting the effect of very strong lines:

$$M(t, \eta_{max}) = k_{CAK} t^{-\alpha} \left[\frac{(1 + t\eta_{max})^{1-\alpha} - 1}{(t\eta_{max})^{1-\alpha}} \right] = k_{CAK} t^{-\alpha} \left[\frac{(1 + \tau_{max})^{1-\alpha} - 1}{(\tau_{max})^{1-\alpha}} \right], \quad (\text{B.3})$$

where η_{max} is the opacity of the most opaque line and $\tau_{max} = t\eta_{max}$ (η_{max} is in units of electron scattering opacity). Note that the expression in the square brackets is an example of the $\epsilon_{fm}(t, \xi)$ correction factor that we introduced in eq B.1. For very large τ_{max} , one recovers the original CAK

equation, whereas for small τ_{max} , the force multiplier equals to $M_{max} = k_{CAK}(1 - \alpha)\eta_{max}^\alpha$, therefore the cut-off opacity could be estimate based on our results as

$$\eta_{max}(\xi) \simeq [M_{max}(\xi)/k(\xi)/(1 - \alpha(\xi))]^{1/\alpha}. \quad (\text{B.4})$$

To facility a comparison of the properties of the force multiplier for different SEDs and their trends with ξ , in Fig. B.3 we show six parameters: M_{max} , k , the ratio of M_{max} and k , maximum line opacity η_{max} , α , and δ . One the main results shown in this figure is that up to $T_{BB} \lesssim 2 \times 10^5$ K, the properties of $M(t, \xi)$ are very sensitive to SEDs. For higher temperature SEDs, the force multiplier parameters are sensitive to SEDs and strongly dependent on ξ , expect for the α parameter that even for the hottest SED changes by no more than a factor of 2 over a span of seven orders of magnitudes of ξ .

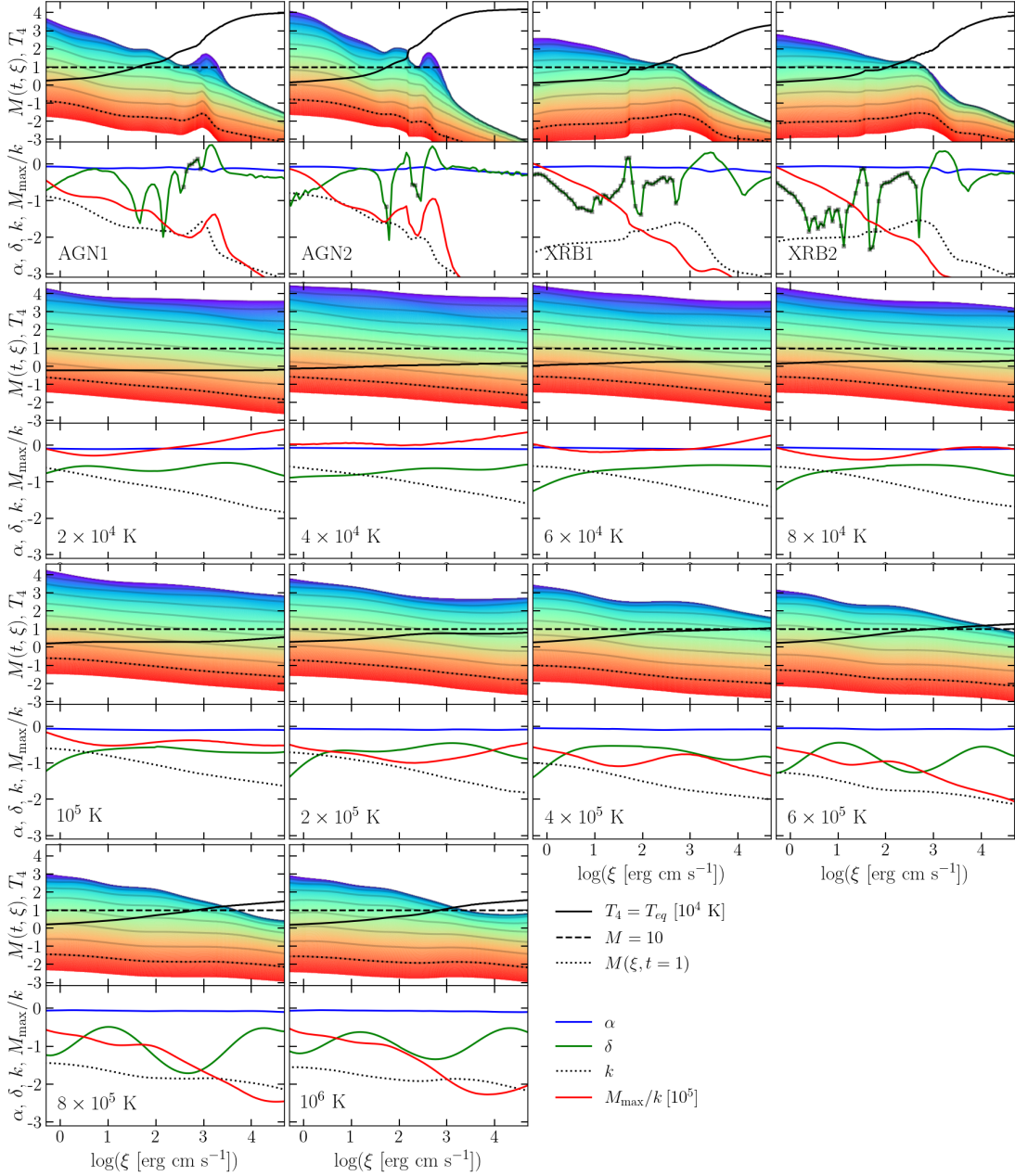


Figure B.2. Parameter survey of photoionization results for the two AGNs and two XRBs SEDs (top row of pair of panels), and ten blackbody SEDs of different temperatures. From left to right, from second top row of panels to bottom, the SEDs correspond to BBs with $T = 2 \times 10^4$ K, 4×10^4 K, 6×10^4 K, 8×10^4 K, 10^5 K, 2×10^5 K, 4×10^5 K, 6×10^5 K, 8×10^5 K, 10^6 K. The first four SEDs correspond to an unobscured and obscured AGN (AGN1 and AGN2; Mehdipour et al., 2015) and hard and soft state XRBs (XRB1 and XRB2; Trigo et al., 2013). *Top panels:* colormap of the force multiplier for t going from $\log t = 1$ (red) to $\log t = -8$ (blue). Black dotted lines mark $M(t, \xi)$, while gray lines indicate $M(t, \xi)$ at $\log t = -1, -2, \dots, -8$. The horizontal dashed line marks the value $M(t, \xi) = 10$, to indicate the level above which line driving can be the dominant outflow driving mechanism. The solid black line is the equilibrium temperature (or S-curve), T_{eq} , in units of 10^4 K. *Bottom panels:* profiles of $\alpha(\xi)$, $k(\xi)$, $|\delta(\xi)|$, and $M_{\text{max}}(\xi)/k(\xi)$ (blue, black dashed, green, and red curves, respectively), the four parameters characterizing the behavior of the force multiplier. To mark negative values of δ we added grey squares atop the green line.

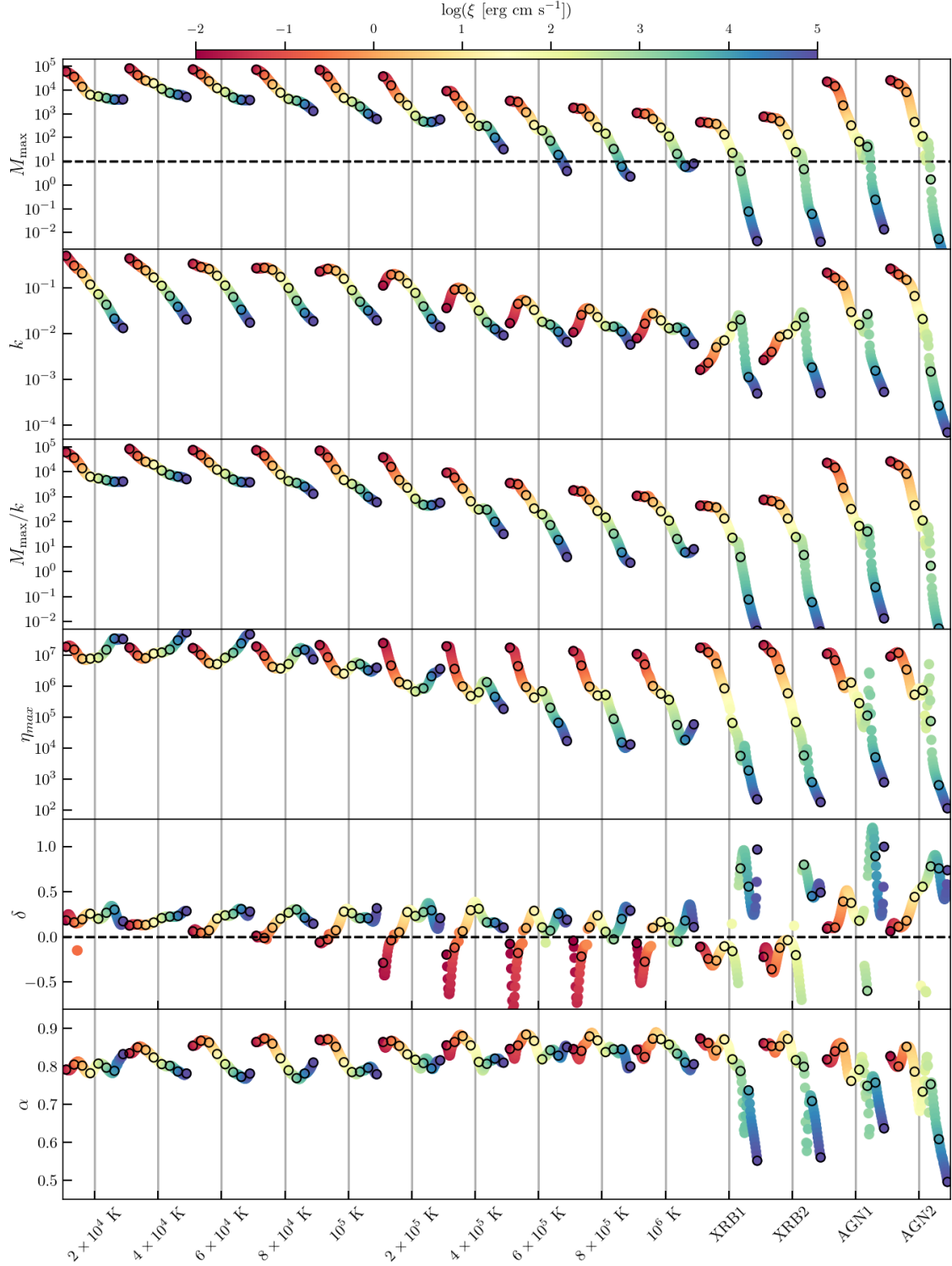


Figure B.3. Parameter survey of our line force result for the ten BB SEDs of different temperatures, XRB, and AGN SEDs with increasing mean photon energy from left to right. The parameters of interest from top to bottom are M_{max} , k , the ratio of M_{max} and k , maximum line opacity η_{max} , α , and δ . The color of the of each point corresponds to $\log \xi$ shown in the color bar along the top (red corresponding to low ionization and blue with high ionization). The circled points correspond to where $\log \xi = -2, -1, 0, 1, 2, 3, 4, 5$, and the vertical lines are for reference but also indicate where $\xi \approx 30$ for each SED.

BIBLIOGRAPHY

- Abbott, D. C. (1982). The theory of radiatively driven stellar winds. II. The line acceleration. *ApJ*, 259:282–301.
- Arav, N. and Li, Z.-Y. (1994). The Role of Radiative Acceleration in Outflows from Broad Absorption Line QSOs. I. Comparison with O Star Winds. *ApJ*, 427:700.
- Arav, N., Liu, G., Xu, X., Stidham, J., Benn, C., and Chamberlain, C. (2018). Evidence that 50% of BALQSO Outflows Are Situated at Least 100 pc from the Central Source. *ApJ*, 857(1):60.
- Balbus, S. A. (1986). Local Dynamic Thermal Instability. *ApJL*, 303:L79.
- Balbus, S. A. (1995). Thermal Instability. In Ferrara, A., McKee, C. F., Heiles, C., and Shapiro, P. R., editors, *The Physics of the Interstellar Medium and Intergalactic Medium*, volume 80 of *Astronomical Society of the Pacific Conference Series*, page 328.
- Barai, P., Proga, D., and Nagamine, K. (2012). Multiphase, non-spherical gas accretion on to a black hole. *MNRAS*, 424(1):728–746.
- Bennert, N., Falcke, H., Schulz, H., Wilson, A. S., and Wills, B. J. (2002). Size and structure of the narrow-line region of quasars. *The Astrophysical Journal*, 574(2):L105–L109.
- Bowler, R. A. A., Hewett, P. C., Allen, J. T., and Ferland, G. J. (2014). Line-driven radiative outflows in luminous quasars. *MNRAS*, 445(1):359–377.
- Capellupo, D. M., Hamann, F., Shields, J. C., Rodríguez Hidalgo, P., and Barlow, T. A. (2011). Variability in quasar broad absorption line outflows - I. Trends in the short-term versus long-term data. *MNRAS*, 413(2):908–920.
- Capellupo, D. M., Hamann, F., Shields, J. C., Rodríguez Hidalgo, P., and Barlow, T. A. (2012). Variability in quasar broad absorption line outflows - II. Multi-epoch monitoring of Si IV and C IV broad absorption line variability. *MNRAS*, 422(4):3249–3267.
- Castor, J. I., Abbott, D. C., and Klein, R. I. (1975). Radiation-driven winds in Of stars. *ApJ*, 195:157–174.
- Castor, J. L. (1974). On the force associated with absorption of spectral line radiation. *MNRAS*, 169:279–306.
- Chartas, G., Brandt, W. N., Gallagher, S. C., and Garmire, G. P. (2002). CHANDRA Detects Relativistic Broad Absorption Lines from APM 08279+5255. *ApJ*, 579(1):169–175.
- Chartas, G., Saez, C., Brandt, W. N., Giustini, M., and Garmire, G. P. (2009). Confirmation of and Variable Energy Injection by a Near-Relativistic Outflow in APM 08279+5255. *ApJ*, 706(1):644–656.
- Chelouche, D. and Netzer, H. (2003). Continuum shielding and flow dynamics in active galactic nuclei. *MNRAS*, 344(1):233–241.
- Chen, Z.-F. and Pan, D.-S. (2017). Collective Properties of Quasar Narrow Associated Absorption Lines. *ApJ*, 848(2):79.

- Choi, E., Naab, T., Ostriker, J. P., Johansson, P. H., and Moster, B. P. (2014). Consequences of mechanical and radiative feedback from black holes in disc galaxy mergers. *MNRAS*, 442(1):440–453.
- Ciotti, L., Ostriker, J. P., and Proga, D. (2010). Feedback from Central Black Holes in Elliptical Galaxies. III. Models with Both Radiative and Mechanical Feedback. *ApJ*, 717(2):708–723.
- Clarke, C. and Carswell, B. (2014). *Principles of Astrophysical Fluid Dynamics*.
- Crenshaw, D. M., Kraemer, S. B., and George, I. M. (2003). Mass Loss from the Nuclei of Active Galaxies. *ARA&A*, 41:117–167.
- Curé, M., Cidale, L., and Granada, A. (2011). Slow Radiation-driven Wind Solutions of A-type Supergiants. *ApJ*, 737(1):18.
- Dannen, R. C., Proga, D., Kallman, T. R., and Waters, T. (2019). Photoionization Calculations of the Radiation Force Due To Spectral Lines in AGNs. *ApJ*, 882(2):99.
- Dannen, R. C., Proga, D., Waters, T., and Dyda, S. (2020). Clumpy AGN Outflows due to Thermal Instability. *ApJL*, 893(2):L34.
- Davidson, K. and Netzer, H. (1979). The emission lines of quasars and similar objects. *Reviews of Modern Physics*, 51(4):715–766.
- de Kool, M. and Begelman, M. C. (1995). Radiation Pressure-driven Magnetic Disk Winds in Broad Absorption Line Quasi-stellar Objects. *ApJ*, 455:448.
- Dyda, S., Dannen, R., Waters, T., and Proga, D. (2017). Irradiation of astrophysical objects - SED and flux effects on thermally driven winds. *MNRAS*, 467(4):4161–4173.
- Dyda, S. and Proga, D. (2018). Non-axisymmetric line-driven disc winds II - full velocity gradient. *MNRAS*, 478(4):5006–5016.
- Dyda, S., Proga, D., and Reynolds, C. S. (2020). Effects of opacity temperature dependence on radiatively accelerated clouds. *MNRAS*, 493(1):437–445.
- Elvis, M. (2017). Quasar Rain: The Broad Emission Line Region as Condensations in the Warm Accretion Disk Wind. *ApJ*, 847(1):56.
- Everett, J. E. (2005). Radiative Transfer and Acceleration in Magnetocentrifugal Winds. *ApJ*, 631(2):689–706.
- Fabian, A. C. (2012). Observational Evidence of Active Galactic Nuclei Feedback. *ARA&A*, 50:455–489.
- Fath, E. A. (1909). The spectra of some spiral nebulae and globular star clusters. *Lick Observatory Bulletin*, 149:71–77.
- Faucher-Giguère, C.-A., Quataert, E., and Murray, N. (2012). A physical model of FeLoBALs: implications for quasar feedback. *MNRAS*, 420(2):1347–1354.
- Ferland, G. J., Chatzikos, M., Guzmán, F., Lykins, M. L., van Hoof, P. A. M., Williams, R. J. R., Abel, N. P., Badnell, N. R., Keenan, F. P., Porter, R. L., and Stancil, P. C. (2017). The 2017 Release Cloudy. *RMxAA*, 53:385–438.

- Ferrarese, L. and Merritt, D. (2000). A Fundamental Relation between Supermassive Black Holes and Their Host Galaxies. *ApJL*, 539(1):L9–L12.
- Field, G. B. (1965). Thermal Instability. *ApJ*, 142:531.
- Foltz, C. B., Weymann, R. J., Morris, S. L., and Turnshek, D. A. (1987). The Complex Absorption Spectrum of the Broad Absorption Line QSO 1303+308. *ApJ*, 317:450.
- Fu, X.-D., Zhang, S.-N., Sun, W., Niu, S., and Ji, L. (2017). Joint fit of Warm Absorbers in COS and HETG spectra of NGC 3783. *Research in Astronomy and Astrophysics*, 17(9):095.
- Furlanetto, S. R. and Loeb, A. (2003). Metal Absorption Lines as Probes of the Intergalactic Medium Prior to the Reionization Epoch. *ApJ*, 588(1):18–34.
- Gabel, J. R., Crenshaw, D. M., Kraemer, S. B., Brandt, W. N., George, I. M., Hamann, F. W., Kaiser, M. E., Kaspi, S., Kriss, G. A., Mathur, S., Mushotzky, R. F., Nandra, K., Netzer, H., Peterson, B. M., Shields, J. C., Turner, T. J., and Zheng, W. (2003). The Ionized Gas and Nuclear Environment in NGC 3783. II. Averaged Hubble Space Telescope/STIS and Far Ultraviolet Spectroscopic Explorer Spectra. *ApJ*, 583(1):178–191.
- Ganguly, R., Masiero, J., Charlton, J. C., and Sembach, K. R. (2003). An Intrinsic Absorption Complex toward RX J1230.8+0115: Geometry and Photoionization Conditions. *ApJ*, 598(2):922–934.
- Gaspari, M., Ruszkowski, M., and Oh, S. P. (2013). Chaotic cold accretion on to black holes. *MNRAS*, 432(4):3401–3422.
- Gayley, K. G. (1995). An Improved Line-Strength Parameterization in Hot-Star Winds. *ApJ*, 454:410.
- Gebhardt, K., Bender, R., Bower, G., Dressler, A., Faber, S. M., Filippenko, A. V., Green, R., Grillmair, C., Ho, L. C., Kormendy, J., Lauer, T. R., Magorrian, J., Pinkney, J., Richstone, D., and Tremaine, S. (2000). A Relationship between Nuclear Black Hole Mass and Galaxy Velocity Dispersion. *ApJL*, 539(1):L13–L16.
- Giustini, M., Cappi, M., Chartas, G., Dadina, M., Eracleous, M., Ponti, G., Proga, D., Tombesi, F., Vignali, C., and Palumbo, G. G. C. (2011). Variable X-ray absorption in the mini-BAL QSO PG 1126-041. *A&A*, 536:A49.
- Giustini, M. and Proga, D. (2019). A global view of the inner accretion and ejection flow around super massive black holes. Radiation-driven accretion disk winds in a physical context. *A&A*, 630:A94.
- Gofford, J., Reeves, J. N., Tombesi, F., Braitto, V., Turner, T. J., Miller, L., and Cappi, M. (2013). The Suzaku view of highly ionized outflows in AGN - I. Statistical detection and global absorber properties. *MNRAS*, 430(1):60–80.
- Gupta, N., Srianand, R., Petitjean, P., and Ledoux, C. (2003). Outflowing material in the $z_{em} = 4.92$ BAL QSO SDSS J160501.21-011220.0. *A&A*, 406:65–73.
- Haiman, Z. and Bryan, G. L. (2006). Was Star Formation Suppressed in High-Redshift Minihalos? *ApJ*, 650(1):7–11.

- Halpern, J. P. (1984). Variable X-ray absorption in the QSO MR 2251-178. *ApJ*, 281:90–94.
- Hamann, F., Chartas, G., McGraw, S., Rodriguez Hidalgo, P., Shields, J., Capellupo, D., Charlton, J., and Eracleous, M. (2013). Extreme-velocity quasar outflows and the role of X-ray shielding. *MNRAS*, 435(1):133–148.
- Hamann, F., Chartas, G., Reeves, J., and Nardini, E. (2018). Does the X-ray outflow quasar PDS 456 have a UV outflow at 0.3c? *MNRAS*, 476(1):943–953.
- Hamann, F., Kanekar, N., Prochaska, J. X., Murphy, M. T., Ellison, S., Malec, A. L., Milutinovic, N., and Ubachs, W. (2011). A high-velocity narrow absorption line outflow in the quasar J212329.46 - 005052.9. *MNRAS*, 410(3):1957–1974.
- Hickox, R. C. and Alexander, D. M. (2018). Obscured Active Galactic Nuclei. *ARA&A*, 56:625–671.
- Higginbottom, N. and Proga, D. (2015). Coronae and Winds from Irradiated Disks in X-Ray Binaries. *ApJ*, 807(1):107.
- Higginbottom, N., Proga, D., Knigge, C., and Long, K. S. (2017). Thermal Disk Winds in X-Ray Binaries: Realistic Heating and Cooling Rates Give Rise to Slow, but Massive, Outflows. *ApJ*, 836(1):42.
- Higginbottom, N., Proga, D., Knigge, C., Long, K. S., Matthews, J. H., and Sim, S. A. (2014). Line-driven Disk Winds in Active Galactic Nuclei: The Critical Importance of Ionization and Radiative Transfer. *ApJ*, 789(1):19.
- Hopkins, P. F., Hernquist, L., Cox, T. J., Di Matteo, T., Robertson, B., and Springel, V. (2006). A Unified, Merger-driven Model of the Origin of Starbursts, Quasars, the Cosmic X-Ray Background, Supermassive Black Holes, and Galaxy Spheroids. *ApJS*, 163(1):1–49.
- Kaastra, J. S., Kriss, G. A., Cappi, M., Mehdipour, M., Petrucci, P. O., Steenbrugge, K. C., Arav, N., Behar, E., Bianchi, S., Boissay, R., Branduardi-Raymont, G., Chamberlain, C., Costantini, E., Ely, J. C., Ebrero, J., Di Gesu, L., Harrison, F. A., Kaspi, S., Malzac, J., De Marco, B., Matt, G., Nandra, K., Paltani, S., Person, R., Peterson, B. M., Pinto, C., Ponti, G., Nuñez, F. P., De Rosa, A., Seta, H., Ursini, F., de Vries, C. P., Walton, D. J., and Whewell, M. (2014). A fast and long-lived outflow from the supermassive black hole in NGC 5548. *Science*, 345(6192):64–68.
- Kallman, T. and Bautista, M. (2001). Photoionization and High-Density Gas. *ApJS*, 133(1):221–253.
- Kallman, T. R. and McCray, R. (1982). X-ray nebular models. *ApJS*, 50:263–317.
- Kaspi, S., Brandt, W. N., George, I. M., Netzer, H., Crenshaw, D. M., Gabel, J. R., Hamann, F. W., Kaiser, M. E., Koratkar, A., Kraemer, S. B., Kriss, G. A., Mathur, S., Mushotzky, R. F., Nandra, K., Peterson, B. M., Shields, J. C., Turner, T. J., and Zheng, W. (2002). The Ionized Gas and Nuclear Environment in NGC 3783. I. Time-averaged 900 Kilosecond Chandra Grating Spectroscopy. *ApJ*, 574(2):643–662.
- Kinch, B. E., Schnittman, J. D., Kallman, T. R., and Krolik, J. H. (2016). Fe $K\alpha$ Profiles from Simulations of Accreting Black Holes. *ApJ*, 826(1):52.
- Knigge, C., Scaringi, S., Goad, M. R., and Cottis, C. E. (2008). The intrinsic fraction of broad-absorption line quasars. *MNRAS*, 386(3):1426–1435.

- Krolik, J. H. (1999). *Active galactic nuclei : from the central black hole to the galactic environment*.
- Krolik, J. H. and Vrtilik, J. M. (1984). The dynamics of the narrow line regions of Seyfert galaxies. *ApJ*, 279:521–528.
- Kurosawa, R. and Proga, D. (2008). Three-dimensional Simulations of Inflows Irradiated by a Precessing Accretion Disk in Active Galactic Nuclei: Formation of Outflows. *ApJ*, 674(1):97–110.
- Kurosawa, R. and Proga, D. (2009a). On the large-scale outflows in active galactic nuclei: consequences of coupling the mass supply rate and accretion luminosity. *MNRAS*, 397(4):1791–1803.
- Kurosawa, R. and Proga, D. (2009b). Three-Dimensional Simulations of Dynamics of Accretion Flows Irradiated by a Quasar. *ApJ*, 693(2):1929–1945.
- Laha, S., Reynolds, C. S., Reeves, J., Kriss, G., Guainazzi, M., Smith, R., Veilleux, S., and Proga, D. (2020). Ionized outflows from active galactic nuclei as the essential elements of feedback. *Nature Astronomy*.
- Lamers, H. J. G. L. M. and Cassinelli, J. P. (1999). *Introduction to Stellar Winds*.
- Longinotti, A. L., Krongold, Y., Kriss, G. A., Ely, J., Gallo, L., Grupe, D., Komossa, S., Mathur, S., and Pradhan, A. (2013). The Rise of an Ionized Wind in the Narrow-line Seyfert 1 Galaxy Mrk 335 Observed by XMM-Newton and HST. *ApJ*, 766(2):104.
- Lu, W.-J. and Lin, Y.-R. (2018). Narrow Absorption Lines Complex. II. Probing the Line-locking Signatures within the Trough-like Broad Absorption Line. *ApJ*, 863(2):186.
- Luketic, S., Proga, D., Kallman, T. R., Raymond, J. C., and Miller, J. M. (2010). On the Properties of Thermal Disk Winds in X-ray Transient Sources: A Case Study of GRO J1655-40. *ApJ*, 719(1):515–522.
- Lynden-Bell, D. (1969). Galactic Nuclei as Collapsed Old Quasars. *Nature*, 223(5207):690–694.
- Magorrian, J., Tremaine, S., Richstone, D., Bender, R., Bower, G., Dressler, A., Faber, S. M., Gebhardt, K., Green, R., Grillmair, C., Kormendy, J., and Lauer, T. (1998). The Demography of Massive Dark Objects in Galaxy Centers. *AJ*, 115(6):2285–2305.
- Mas-Ribas, L. and Mauland, R. (2019). The Ubiquitous Imprint of Radiative Acceleration in the Mean Absorption Spectrum of Quasar Outflows. *ApJ*, 886(2):151.
- McCarthy, I. G., Schaye, J., Ponman, T. J., Bower, R. G., Booth, C. M., Dalla Vecchia, C., Crain, R. A., Springel, V., Theuns, T., and Wiersma, R. P. C. (2010). The case for AGN feedback in galaxy groups. *MNRAS*, 406(2):822–839.
- McCourt, M., Sharma, P., Quataert, E., and Parrish, I. J. (2012). Thermal instability in gravitationally stratified plasmas: implications for multiphase structure in clusters and galaxy haloes. *MNRAS*, 419(4):3319–3337.
- McGraw, S. M., Brandt, W. N., Grier, C. J., Filiz Ak, N., Hall, P. B., Schneider, D. P., Anderson, S. F., Green, P. J., Hutchinson, T. A., Macleod, C. L., and Vivek, M. (2017). Broad absorption line disappearance and emergence using multiple-epoch spectroscopy from the Sloan Digital Sky Survey. *MNRAS*, 469(3):3163–3184.

- Mehdipour, M., Kaastra, J. S., Kriss, G. A., Arav, N., Behar, E., Bianchi, S., Branduardi-Raymont, G., Cappi, M., Costantini, E., Ebrero, J., Di Gesu, L., Kaspi, S., Mao, J., De Marco, B., Matt, G., Paltani, S., Peretz, U., Peterson, B. M., Petrucci, P. O., Pinto, C., Ponti, G., Ursini, F., de Vries, C. P., and Walton, D. J. (2017). Chasing obscuration in type-I AGN: discovery of an eclipsing clumpy wind at the outer broad-line region of NGC 3783. *A&A*, 607:A28.
- Mehdipour, M., Kaastra, J. S., Kriss, G. A., Cappi, M., Petrucci, P. O., De Marco, B., Ponti, G., Steenbrugge, K. C., Behar, E., Bianchi, S., Branduardi-Raymont, G., Costantini, E., Ebrero, J., Di Gesu, L., Matt, G., Paltani, S., Peterson, B. M., Ursini, F., and Whewell, M. (2016). Anatomy of the AGN in NGC 5548. VII. Swift study of obscuration and broadband continuum variability. *A&A*, 588:A139.
- Mehdipour, M., Kaastra, J. S., Kriss, G. A., Cappi, M., Petrucci, P. O., Steenbrugge, K. C., Arav, N., Behar, E., Bianchi, S., Boissay, R., Branduardi-Raymont, G., Costantini, E., Ebrero, J., Di Gesu, L., Harrison, F. A., Kaspi, S., De Marco, B., Matt, G., Paltani, S., Peterson, B. M., Ponti, G., Pozo Nuñez, F., De Rosa, A., Ursini, F., de Vries, C. P., Walton, D. J., and Whewell, M. (2015). Anatomy of the AGN in NGC 5548. I. A global model for the broadband spectral energy distribution. *A&A*, 575:A22.
- Mościbrodzka, M. and Proga, D. (2013). Thermal and Dynamical Properties of Gas Accreting onto a Supermassive Black Hole in an Active Galactic Nucleus. *ApJ*, 767(2):156.
- Murray, N., Chiang, J., Grossman, S. A., and Voit, G. M. (1995). Accretion Disk Winds from Active Galactic Nuclei. *ApJ*, 451:498.
- Mushotzky, R. F., Solomon, P. M., and Strittmatter, P. A. (1972). Radiation-Pressure Mass Loss from Quasi-Stellar Objects. *ApJ*, 174:7.
- Nardini, E., Reeves, J. N., Gofford, J., Harrison, F. A., Risaliti, G., Braitto, V., Costa, M. T., Matzeu, G. A., Walton, D. J., Behar, E., Boggs, S. E., Christensen, F. E., Craig, W. W., Hailey, C. J., Matt, G., Miller, J. M., O’Brien, P. T., Stern, D., Turner, T. J., and Ward, M. J. (2015). Black hole feedback in the luminous quasar PDS 456. *Science*, 347(6224):860–863.
- Nayakshin, S. (2014). Two-phase model for black hole feeding and feedback. *MNRAS*, 437(3):2404–2411.
- Netzer, H. (2013). *The Physics and Evolution of Active Galactic Nuclei*.
- Nomura, M., Ohsuga, K., and Done, C. (2020). Line-driven disc wind in near-Eddington active galactic nuclei: decrease of mass accretion rate due to powerful outflow. *MNRAS*, 494(3):3616–3626.
- Nomura, M., Ohsuga, K., Wada, K., Susa, H., and Misawa, T. (2013). Modeling Line-Driven Disk Wind for Broad Absorption Lines of Quasars. *PASJ*, 65:40.
- North, M., Knigge, C., and Goad, M. (2006). A new sample of broad absorption-line quasars exhibiting the ghost of Lyman α . *MNRAS*, 365(4):1057–1066.
- Ostriker, J. P., Choi, E., Ciotti, L., Novak, G. S., and Proga, D. (2010). Momentum Driving: Which Physical Processes Dominate Active Galactic Nucleus Feedback? *ApJ*, 722(1):642–652.
- Owocki, S. P., Castor, J. I., and Rybicki, G. B. (1988). Time-dependent Models of Radiatively Driven Stellar Winds. I. Nonlinear Evolution of Instabilities for a Pure Absorption Model. *ApJ*, 335:914.

- Owocki, S. P., Cranmer, S. R., and Blondin, J. M. (1994). Two-dimensional Hydrodynamical Simulations of Wind-compressed Disks around Rapidly Rotating B Stars. *ApJ*, 424:887.
- Proga, D. (1999). Comparison of theoretical radiation-driven winds from stars and discs. *MNRAS*, 304(4):938–946.
- Proga, D. (2007). Dynamics of Accretion Flows Irradiated by a Quasar. *ApJ*, 661(2):693–702.
- Proga, D. and Kallman, T. R. (2002). On the Role of the Ultraviolet and X-Ray Radiation in Driving a Disk Wind in X-Ray Binaries. *ApJ*, 565(1):455–470.
- Proga, D. and Kallman, T. R. (2004). Dynamics of Line-driven Disk Winds in Active Galactic Nuclei. II. Effects of Disk Radiation. *ApJ*, 616(2):688–695.
- Proga, D., Stone, J. M., and Drew, J. E. (1998). Radiation-driven winds from luminous accretion discs. *MNRAS*, 295(3):595–617.
- Proga, D., Stone, J. M., and Drew, J. E. (1999). Line-driven disc wind models with an improved line force. *MNRAS*, 310(2):476–482.
- Proga, D., Stone, J. M., and Kallman, T. R. (2000). Dynamics of Line-driven Disk Winds in Active Galactic Nuclei. *ApJ*, 543(2):686–696.
- Proga, D. and Waters, T. (2015). Cloud Formation and Acceleration in a Radiative Environment. *ApJ*, 804(2):137.
- Puls, J., Springmann, U., and Lennon, M. (2000). Radiation driven winds of hot luminous stars. XIV. Line statistics and radiative driving. *A&AS*, 141:23–64.
- Quera-Bofarull, A., Done, C., Lacey, C. G., Nomura, M., and Ohsuga, K. (2021). Qwind3: UV line-driven accretion disc wind models for AGN feedback. *arXiv e-prints*, page arXiv:2111.02742.
- Ramírez-Velasquez, J. M., Klapp, J., Gabbasov, R., Cruz, F., and Sigalotti, L. D. G. (2016). Impetus: New Cloudy’s Radiative Tables for Accretion onto a Galaxy Black Hole. *ApJS*, 226(2):22.
- Rees, M. J. (1984). Black Hole Models for Active Galactic Nuclei. *ARA&A*, 22:471–506.
- Reeves, J. N., Lobban, A., and Pounds, K. A. (2018). The Variable Fast Soft X-Ray Wind in PG 1211+143. *ApJ*, 854(1):28.
- Reynolds, C. S. and Fabian, A. C. (1995a). Warm absorbers in active galactic nuclei. *MNRAS*, 273(4):1167–1176.
- Reynolds, C. S. and Fabian, A. C. (1995b). Warm absorbers in active galactic nuclei. *MNRAS*, 273(4):1167–1176.
- Saez, C. and Chartas, G. (2011). A Study of the X-rayed Outflow of APM 08279+5255 through Photoionization Codes. *ApJ*, 737(2):91.
- Salpeter, E. E. (1964). Accretion of Interstellar Matter by Massive Objects. *ApJ*, 140:796–800.
- Salz, M., Banerjee, R., Mignone, A., Schneider, P. C., Czesla, S., and Schmitt, J. H. M. M. (2015). TPCI: the PLUTO-CLOUDY Interface . A versatile coupled photoionization hydrodynamics code. *A&A*, 576:A21.

- Seyfert, C. K. (1943). Nuclear Emission in Spiral Nebulae. *ApJ*, 97:28.
- Shakura, N. I. and Sunyaev, R. A. (1973). Reprint of 1973A&A....24..337S. Black holes in binary systems. Observational appearance. *A&A*, 500:33–51.
- Sharma, P., McCourt, M., Quataert, E., and Parrish, I. J. (2012). Thermal instability and the feedback regulation of hot haloes in clusters, groups and galaxies. *MNRAS*, 420(4):3174–3194.
- Shields, J. C. and Hamann, F. (1997). On the Nature of Ultraviolet and X-Ray Absorption in NGC 3783. *ApJ*, 481(2):752–757.
- Shlosman, I., Vitello, P. A., and Shaviv, G. (1985). Active galactic nuclei - Internal dynamics and formation of emission clouds. *ApJ*, 294:96–105.
- Shu, F. H. (1992). *The physics of astrophysics. Volume II: Gas dynamics*.
- Silk, J. and Rees, M. J. (1998). Quasars and galaxy formation. *A&A*, 331:L1–L4.
- Sim, S. A., Proga, D., Miller, L., Long, K. S., and Turner, T. J. (2010). Multidimensional modelling of X-ray spectra for AGN accretion disc outflows - III. Application to a hydrodynamical simulation. *MNRAS*, 408(3):1396–1408.
- Srianand, R., Petitjean, P., Ledoux, C., and Hazard, C. (2002). A collimated flow driven by radiative pressure from the nucleus of quasar Q1511 + 091. *MNRAS*, 336(3):753–758.
- Stevens, I. R. (1991). X-Ray-illuminated Stellar Winds: Optically Thick Wind Models for Massive X-Ray Binaries. *ApJ*, 379:310.
- Stevens, I. R. and Kallman, T. R. (1990). X-Ray Illuminated Stellar Winds: Ionization Effects in the Radiative Driving of Stellar Winds in Massive X-Ray Binary Systems. *ApJ*, 365:321.
- Stone, J. M. and Proga, D. (2009). Anisotropic Winds from Close-In Extrasolar Planets. *ApJ*, 694(1):205–213.
- Stone, J. M., Tomida, K., White, C. J., and Felker, K. G. (2020). The Athena++ Adaptive Mesh Refinement Framework: Design and Magnetohydrodynamic Solvers. *ApJS*, 249(1):4.
- Strateva, I. V., Strauss, M. A., Hao, L., Schlegel, D. J., Hall, P. B., Gunn, J. E., Li, L.-X., Ivezić, Z., Richards, G. T., Zakamska, N. L., Voges, W., Anderson, S. F., Lupton, R. H., Schneider, D. P., Brinkmann, J., and Nichol, R. C. (2003). Double-peaked Low-Ionization Emission Lines in Active Galactic Nuclei. *AJ*, 126(4):1720–1749.
- Takeuchi, S., Ohsuga, K., and Mineshige, S. (2013). Clumpy Outflows from Supercritical Accretion Flow. *PASJ*, 65:88.
- Tombesi, F., Cappi, M., Reeves, J. N., Nemmen, R. S., Braitto, V., Gaspari, M., and Reynolds, C. S. (2013). Unification of X-ray winds in Seyfert galaxies: from ultra-fast outflows to warm absorbers. *Monthly Notices of the Royal Astronomical Society*, 430(2):1102–1117.
- Tombesi, F., Cappi, M., Reeves, J. N., Palumbo, G. G. C., Yaqoob, T., Braitto, V., and Dadina, M. (2010a). Evidence for ultra-fast outflows in radio-quiet AGNs. I. Detection and statistical incidence of Fe K-shell absorption lines. *A&A*, 521:A57.

- Tombesi, F., Cappi, M., Reeves, J. N., Palumbo, G. G. C., Yaqoob, T., Braito, V., and Dadina, M. (2010b). Evidence for ultra-fast outflows in radio-quiet AGNs. I. Detection and statistical incidence of Fe K-shell absorption lines. *A&A*, 521:A57.
- Trigo, M. D., Boirin, L., Migliari, S., Miller-Jones, J., Parmar, A., and Sidoli, L. (2013). Variability of winds in X-ray binaries. In Zhang, C. M., Belloni, T., Méndez, M., and Zhang, S. N., editors, *Feeding Compact Objects: Accretion on All Scales*, volume 290, pages 25–28.
- Urry, C. (2004). AGN Unification: An Update. In Richards, G. T. and Hall, P. B., editors, *AGN Physics with the Sloan Digital Sky Survey*, volume 311 of *Astronomical Society of the Pacific Conference Series*, page 49.
- Wang, B.-C., Yang, X.-H., Bu, D.-F., and Huang, S.-S. (2022). Effect of radiation drag on the line-force-driven winds. *MNRAS*, 515(4):5594–5603.
- Waters, T. and Proga, D. (2016). On the efficient acceleration of clouds in active galactic nuclei. *MNRAS*, 460(1):L79–L83.
- Waters, T. and Proga, D. (2018). Magnetothermal disc winds in X-ray binaries: poloidal magnetic fields suppress thermal winds. *MNRAS*, 481(2):2628–2645.
- Waters, T. and Proga, D. (2019). Non-isobaric Thermal Instability. *ApJ*, 875(2):158.
- Waters, T., Proga, D., and Dannen, R. (2021). Multiphase AGN Winds from X-Ray-irradiated Disk Atmospheres. *ApJ*, 914(1):62.
- Waters, T., Proga, D., Dannen, R., and Dyda, S. (2022). Dynamical Thermal Instability in Highly Supersonic Outflows. *ApJ*, 931(2):134.
- Weymann, R. J., Carswell, R. F., and Smith, M. G. (1981). Absorption lines in the spectra of Quasi-Stellar Objects. *ARA&A*, 19:41–76.
- Weymann, R. J., Morris, S. L., Foltz, C. B., and Hewett, P. C. (1991). Comparisons of the Emission-Line and Continuum Properties of Broad Absorption Line and Normal Quasi-stellar Objects. *ApJ*, 373:23.
- Woods, D. T., Klein, R. I., Castor, J. I., McKee, C. F., and Bell, J. B. (1996). X-Ray-heated Coronae and Winds from Accretion Disks: Time-dependent Two-dimensional Hydrodynamics with Adaptive Mesh Refinement. *ApJ*, 461:767.

CURRICULUM VITAE

Graduate College
University of Nevada, Las Vegas

Randall Cody Dannen
randall.dannen@gmail.com

Degrees:

Bachelor of Science - Physics, 2016
University of Nevada, Las Vegas
Bachelor of Science - Mathematics, 2016
University of Nevada, Las Vegas

Master of Science - Astronomy, 2018
University of Nevada, Las Vegas

Thesis Title:

ON OUTFLOWS DUE TO RADIATION

Thesis Examination Committee:

Chairperson, Daniel Proga, Ph.D.
Committee Member, Zhaohuan Zhu, Ph.D.
Committee Member, Stephen Lepp, Ph.D.
Graduate Faculty Representative, Monika Neda, Ph.D.

Talks & Conference Proceedings:

AAS 241 (2023) — iPoster
University of Cambridge (2020) — Invited Virtual Talk
AAS 235 (2020) — Poster
Athena++ Workshop (2019) — Invited Talk
AGN winds on the Georgia Coast (2017) — Poster

Outreach:

Astronomy on Tap — Organizer & Presenter 2018–2023
UNLV Society of Physics Students — President 2015–2016

Teaching:

PHSY 151L — Fall 2016, 2018, 2019 & Spring 2019
PHSY 180L — Spring 2017, 2020
PHSY 181L — Fall 2016, Spring 2017, 2018, 2020

Publications (ORCID: 0000-0002-5160-8716):

Dynamical Thermal Instability in Highly Supersonic Outflows

Dannen, R., Proga, D., Waters, T.

2023, in prep.

On the transition from efficient to inefficient line-driving in irradiated flows

Waters, T., Proga, D., **Dannen, R.**, Dyda, S.

2022, ApJ, 931, 134. doi:10.3847/1538-4357/ac6612

On Synthetic Absorption Line Profiles of Thermally Driven Winds from Active Galactic Nuclei

Ganguly, S., Proga, D., Waters, T., **Dannen R. C.**, Dyda, S., Giustini, M., Kallman, T., et al.

2021, ApJ, 914, 114. doi:10.3847/1538-4357/abf939

Multiphase AGN winds from X-ray irradiated disk atmospheres

Waters, T., Proga, D., **Dannen, R.**

2020 ApJ, 914, 62. doi:10.3847/1538-4357/abf6e6

Clumpy AGN outflows due to thermal instability

Dannen, R., Proga, D., Waters, T., Dyda, S.

2020, ApJL, 893, L34. doi:10.3847/2041-8213/ab87a5

Photoionization Calculations of the Radiation Force Due To Spectral Lines in AGNs

Dannen, R., Proga, D., Waters, T., Kallman, T.R.

2019, ApJ, 882, 99. doi:10.3847/1538-4357/ab340b

Irradiation of astrophysical objects – SED and flux effects on thermally driven wind

Sergei, D., **Dannen, R.**, Waters, T., Proga, D.

2017, MNRAS, 467, 4161

Synthetic absorption lines for a clumpy medium: a spectral signature for cloud acceleration in AGN?

Waters, T., Proga, D., **Dannen, R.**, Kallman, T.R.

2017, MNRAS, 467, 3160

Technical Skills:

Programming Languages

C/C++, FORTRAN, Python

Software/OS

Athena++, XSTAR, Visit, Git, L^AT_EX

Windows/Linux